THE MODIFICATION, DEVELOPMENT, AND CHARACTERIZATION OF AN AEROSOL DISPERSION WIND TUNNEL FOR THE USE OF CANDIDATE AIR SAMPLER TESTING

by

MATTHEW S. WELCH

A Thesis Submitted in Partial Fulfillment

of the Requirements for the Degree

MASTER OF SCIENCE

Major Subject: Environmental Science

West Texas A&M University

Canyon, Texas

December 2014

ABSTRACT

Before a candidate ambient air monitoring sensor can be used confidently in the field, it first must undergo characterization in a tightly controlled environment. To create those predictable testing conditions, the Aerosol Dispersion Wind Tunnel at the West Texas A&M University Environmental Quality Research and Technology Laboratory was physically modified to ensure sufficient mixing and fully developed flow at the testing section, then verified for acceptable velocity and aerosol concentration profile standards as specified by 40 CFR 53 Subpart D (USEPA, 1987).

Using a particle image velocimetry system, the applicable cross section inside the test chamber was non-intrusively interrogated with planar sheets created by the Class IV Nd:YAG laser. By imaging the displacement of seed aerosols illuminated by the laser light sheet, nearly instantaneous velocity flow fields were calculated and time-averaged at 5 levels across the Y-axis of the test section, resulting in a high resolution velocity profile. These tests showed that the percent coefficient of variation ($C_{v\%}$) for the target velocities of 2 kilometers per hour and 8 kilometers per hour were 3.8 percent and 3.4 percent, respectively.

To characterize the concentration profile within the applicable cross section, a vibrating orifice aerosol generator was used to introduce highly mono-disperse aerosols tagged with a fluorescent tracer into the wind tunnel at the same target speeds mentioned above. An adjustable isokinetic rake fitted with four isokinetic sampling cones was used

to collect the aerosols of varying sizes upon glass fiber filters once isokinetic conditions had been established. The filters were then soaked in an aliquot, and a fluorometer was used to calculate the concentration of the fluorescent tag in each sample. From this the concentration profile within the tunnel was established. To be considered acceptably uniform, the $C_{v\%}$ of the concentration values for each run could not exceed 10 percent. The aerosol concentration distributions within the test section proved more uniform when tested with middle range droplet sizes (7, 10, and 13 micrometers), while concentration values at the high and low ends of the droplet size range (3 and 17 micrometers) did not meet the 10% $C_{v\%}$ standard.

DEDICATION

For my wife Amy and for my daughters Mo and Shay.

Well, it's done…

…now I can be a Dad again.

ACKNOWLEDGEMENTS

I would like to thank my committee chair, Dr. DeOtte, and my committee members, Dr. Auvermann and Dr. Rogers, for their guidance and support throughout the course of this research.

Thanks also go to my friends, colleagues, faculty, and staff of both the Department of Life, Earth, and Environmental Sciences and the School of Engineering and Computer Science for making my time at West Texas A&M University a fantastic experience.

Finally, thanks to my mother and father for their encouragement and support, and especially to my wife and daughters for their limitless patience and love.

Approved:

Robert E. DeOtte
Chairman, Thesis Committee Date

William J. Rogers
Member, Thesis Committee Date

Brent W. Auvermann
Member, Thesis Committee Date

David Sissom
Head, Life, Earth, and Environmental Sciences Date

Angela Spaulding
Dean, Graduate School Date

NOMENCLATURE

AERMOD	American Meteorological Society/Environmental Protection Agency Regulatory Model Improvement Committee Model
APS	Aerodynamic particle sizer
b	Numerator of confidence interval
C	Volumetric concentration non-volatile solute volatile solvent.
C_{iso}	Isokinetic concentration (milligrams / milliliter)
C_u	Mass concentration of uranine to oleic acid
C_v	Coefficient of variation
CAFO	Concentrated animal feeding operation
CCD	Charged coupled device
CFH	Cubic feet per hour
CFM	Cubic feet per minute
CFR	Code of Federal Regulations
D_a	Apparent diameter of impacted spheroid
D_d	Droplet diameter
D_p	Aerosol diameter
$D_{p,corr}$	Aerosol diameter corrected for non-volatile impurities
D_s	Aerosol diameter after application of flattening coefficient
CMM	Cubic meter per minute

EQRTL	Environmental Quality Research and Technology Laboratory
ERM	Equivalent reference method
f	Frequency
F	Flattening coefficient
FEM	Federal equivalent method
FRM	Federal reference method
GMD	Geometric mean diameter
HEPA	High efficiency particulate air
Hz	Hertz
I	Volumetric fraction of non-volatile impurities in the solution
km/hr	Kilometers per hour
LPM	Liters per minute
m	Meter
m^3/hr	Cubic meters per hour
mg	Milligram
mg/m^3	Milligram per cubic meter
ml	Milliliter
mm	Millimeter
m/m	Solution ratio by mass
MP	Mega pixel
m/s	Meters per second
n	Number of realizations
NAAQS	National Ambient Air Quality Standards

NaOH	Sodium hydroxide
Nd:YAG	Neodymium-doped Yttrium Aluminum Garnet
NIST	National Institute of Standards and Technology
PIV	Particle image velocimetry
PM_{10}	Particulate matter ≤ 10 μm in aerodynamic diameter
ppb	Parts per billion
Q	Volumetric flow rate
R	Nominal value of an arbitrary function
s_u	Standard deviation of a sample
TSP	Total suspended particulates
u	Vector velocity component in the X direction
ū	Mean of a sample
USEPA	United States Environmental Protection Agency
V	Velocity
v	Vector velocity component in the Z direction
v_n	Nominal value for a variable *n*
v/v	Solution ratio by volume
VOAG	Vibrating orifice aerosol generator
w_n	Uncertainty value for a measurement *n*
Δt	Time setting between PIV laser pulses
Δs	Displacement
ρ_u	Density of uranine
μ	Mean of a population

μ_g	Geometric mean of a population
μm	Micrometer
μs	Microsecond
σ	Standard deviation of a population
σ_g	Geometric standard deviation of a population
λ	Wavelength

TABLE OF CONTENTS

Page

LIST OF FIGURES

LIST OF TABLES

CHAPTER 1

INTRODUCTION

Before a candidate ambient air monitoring sensor can be used confidently in the field, it first must undergo characterization under tightly controlled conditions so that the researcher (or regulator) will understand the capabilities and limitations of the instrument being used. To create these predictable testing conditions, a facility, in this case the Aerosol Dispersion Wind Tunnel at the West Texas A&M University Environmental Quality Research and Technology Laboratory (EQRTL), must itself be characterized and vetted as able to create conditions that are acceptably controlled. To achieve this goal, the tunnel must first be physically modified to ensure sufficient mixing and fully developed flow at the testing section, then verified for acceptable velocity and aerosol concentration profile standards using the Title 40 Code of Federal Regulations (CFR) 53 Subpart D (USEPA, 1987) and 40 CFR 53 Subpart F (USEPA, 1997) as a guide (see Appendix G for CFR requirements).

According to table D-2 of 40 CFR 53 (USEPA, 1987), in order for the velocity profile within the test section to comply with the regulation, the mean velocity throughout the applicable cross section must be within 10 percent of the specified target wind speed for each test, and no single point within the test plane may deviate more than 10 percent of that measured mean velocity. For this a particle image velocimetry (PIV) system was used to measure horizontal velocity flow fields across five evenly-spaced levels (chords)

along the vertical axis of the applicable cross section and were analyzed for compliance to the rule.

The concentration distribution profile was established using an isokinetic rake fitted with four isokinetic (velocity entering the cone is the same as the ambient velocity) sampling cones. Each cone held a glass fiber filter to collect monodisperse liquid oleic acid droplets generated by a vibrating orifice aerosol generator (VOAG), which were tagged with a fluorescent tracer (uranine). The glass fiber filters were collected and soaked individually in a 50 / 50 (v/v) aliquot solution of isopropyl alcohol and distilled water. A calibrated fluorometer was used to quantify the mass concentration of uranine within each aliquot sample, the data from which were used to determine the mass concentration of aerosol at each sampler point within the cross section. According to the regulation, the coefficient of variation ($C_{v\%}$) of the mass concentrations determined at each of the four sampling cones for each individual testing run may not exceed 10 percent.

$$C_{v\%} = \left(\frac{standard\ deviation}{mean}\right) * 100$$

CHAPTER 2

REVIEW OF LITERATURE

In 1987, the USEPA promulgated size-specific National Ambient Air Quality Standards (NAAQS) for particulate matter less than or equal to 10 micrometers (μm) in aerodynamic diameter (PM_{10}) to replace the previous non-specific standards of total suspended particulates (TSP). New research had emerged showing that aerosols in the PM_{10} range posed a greater human health risk due to its ability to enter the respiratory system and was the impetus for this change. Since that time, aerosol wind tunnels have been used to evaluate and characterize candidate federal reference method (FRM) samplers prior to field deployment ensuring compliance to functional and performance standards specified by the USEPA (Ranade et al., 1990), as it is necessary to test a candidate sampler that is to be used for research and regulatory monitoring in the tightly controlled conditions made possible in a laboratory.

For a sampler evaluation to be compliant, the wind tunnel used for the testing must meet the standards specified in 40 CFR 53 Subpart D (USEPA, 1987) and Subpart F (USEPA, 1997). The particle delivery system must be a blower capable of wind speeds at 2 kilometers per hour (km/hr), 8 km/hr, and 24 km/hr (USEPA, 1987), and the test section needs to be large enough so that the candidate sampler blocks no more than 15 percent of the test section area (USEPA, 1997). Each individual measurement point within the defined cross section (no fewer than 12) must be within 10 percent of the mean

velocity of those points (USEPA, 1987). Once the wind velocity profile is verified, the particulate matter concentration profile of the tunnel must be established using monodisperse liquid aerosols tagged with a fluorescent tracer (USEPA, 1987). An array of isokinetic samplers (or "rake") consisting of at least five evenly-spaced samplers will collect the tagged aerosols generated by a VOAG onto glass-fiber filters. A fluorometer must then be used to quantify the mass of the aerosols deposited upon each filter (see 3.2.4 in Chapter 3), which will in turn be used to calculate the mass concentration at each sampler site. If a mass concentration value at any replicate differs by more than 10 percent from the mean mass concentration, adjustments to the tunnel must be made and the process is repeated (USEPA, 1987).

Perhaps the most important design consideration for an acceptable aerosol wind tunnel is sufficient mixing in the test chamber (Cheng et al., 2004). There are numerous methods to achieve this. The oldest and simplest method is to place the test section ten times the diameter of the tunnel section downwind of the inlet, which will allow the airflow to become fully developed (Cengal and Cimbala, 2014). However, size constraints of a laboratory may make this difficult to achieve, especially if the experimenter wishes the tunnel to be large enough to test actual field instruments instead of scale models. Mixing devices, such as a stationary air blender, can be used to increase turbulence and achieve fully developed flow with a shorter tunnel section, thus generating more mixing and improving both mean velocity and aerosol concentration uniformities in the test section. One such device, described by McFarland et al. (1999), consisted of two concentric wind vanes that generated swirl in opposing directions. The device was shown to reduce the $C_{v\%}$ of wind velocity at the test plane to 3 percent in as

little as 4 cross sectional diameters downstream in emission stacks. Turbulence intensities and $C_{v\%}$ values should not be confused. High turbulence is desirable and will cause rapid fluctuations in point velocity measurements as eddies of multiple scales propagate down the tunnel (Holton, 1979), which is, in effect, the engine for achieving the desired amount of mixing in the test section. It is therefore necessary to average the velocity measurements at a given point over a long enough time interval to account for these fluctuations (Holton, 1979). From these time-averaged data, the $C_{v\%}$ among multiple points is calculated, which should be low if sufficient mixing is present.

While mixing devices do a good job of creating uniform aerosol distribution, they also tend to induce undesirable swirl, which can lead to spatial non-uniformity of downstream velocity (Pankhurst and Holder, 1952) if a sufficient number of duct diameters do not lie between the blender and the test section. Turbulence reduction devices, such as screens, honeycombs and flow straighteners (Pankhurst and Holder, 1952; Hinds and Kuo,1995; Brixey et al., 2002) can be used to transfer the excess total kinetic energy from the high velocity regions to the regions of lower velocity (Pankhurst and Holder, 1952). This effectively breaks up the large-scale eddies created by the blender, which require a long downstream fetch to diminish, into much smaller ones that diminish rapidly. Wire mesh screens, when used alone, have been shown to reduce turbulence intensities from 10-14 percent to 7-10 percent, and when used in conjunction with honeycombs, the turbulence intensities have dropped as low as 3 percent (Hinds and Kuo 1995). Brixey et al. (2002) used a flow straightener device and was able to achieve turbulence intensities in the test section as low as 4 percent. Ranade et al. (1990) describe a wind tunnel used to test the effectiveness of PM_{10} samplers, one of the first

developed for this purpose, which successfully employed a honeycomb device to achieve uniform velocity and aerosol concentration capable of complying with the CFR. In aerosol wind tunnel applications, because it is important to achieve maximum mixing (high turbulence intensities) in the test section, it is unwise to use these devices too close to the testing chamber. A sufficient downwind travel distance must be allowed for the flow to re-develop, bringing the turbulence intensities back to desired levels without the artificial swirl caused by the mixer.

The major considerations when determining which method to use is based on the amount of aerosol loss the tunnel will experience due to these obstructions and amount of total achievable velocity sacrificed due to head loss (aerosol dispersion efficiency coefficient). On one hand, a screen with a porosity of 50 percent would do an extraordinary job of breaking up the turbulence induced by the blender, but would result in a large amount of test aerosols being collected upon the screen. The use of a screen may also result in an unacceptable drop in maximum achievable velocity due to head loss. On the other hand, a honeycomb or a flow straightener with a much larger porosity may result in low aerosol and head loss, but may not adequately reduce the spatial non-uniformities generated by the blender.

There are two main types of wind tunnels used in aerosol research. One is a closed-circuit tunnel, and the reasons for using this design are twofold. First, the closed circuit scheme allows for tight thermal control over the system. Placed in various parts of the tunnel are cooling and heating elements, and by manipulating these elements temperature inversions can be designed, created and studied (Cermak, 1995). This allows for the manipulation of stability coefficients to recreate natural atmospheric temperature

profiles specific to an area or time of day. Second, a closed-circuit tunnel allows great control over wind conditions inside the tunnel, as it is free from external influences such as irregular airflow within a laboratory (Cermak, 2003). For this increased degree of control, however, the experimenter must sacrifice a greater amount of lab space and money, as well as simplicity of design. Flow control devices, such as airfoils and wind vanes, must be placed at the turns in the tunnel in order to condition properly the downstream flow in the test sections. In addition, frictional forces and the generation of heat within the system can become a problem if heat sinks are not employed. Finally, it may prove difficult to ensure the air inside the tunnel is free of particulate matter left over from previous experiments, perhaps from re-entrainment from material deposited upon inner surfaces. Such contamination is likely to skew the results of the current experiment.

The other main type of wind tunnel is of an open-circuit design, where laboratory air is drawn directly into the tunnel and then vented to the atmosphere after flowing through the test section. The major advantages to this design are greater accessibility to a larger test section for physical modeling purposes, lower construction costs, and greater space economy (Cermak, 2003). By using an open circuit design, however, it is not easy to control the thermal profile inside the test section. This is important if an experimenter is planning to study the effects of various atmospheric thermal stability parameters on aerosol dispersion. Nevertheless, if the experimenter is simply trying to achieve uniform velocity and concentration profiles, it is possible to achieve the goal without manipulating thermal conditions. Cheng et al. (2004) accomplished this by incorporating a stationary air blender just downwind of the bell mouth inlet into a 6 foot diameter

circular duct to disperse the aerosols evenly. The air then continued for 30 feet (5 diameters) where it encounters a flow straightener to reduce turbulence. The point of air velocity measurement rested 4 feet beyond the flow straightener, just before the expansion section at the entrance of the test section. At the rear wall of the test section industrial high-efficiency particulate air (HEPA) filters are placed to filter the aerosol before the air enters the blower. Using the air blender and the flow straightener, the team was able to achieve a velocity and aerosol $C_{v\%}$ values compliant with the CFR despite a tunnel length of only 6 diameters.

Most recently, a similarly designed aerosol wind tunnel was developed at the Korea Research Institute of Standards and Science (Lee et al., 2013). It is also a large open-circuit tunnel and employs multiple flow conditioning devices, including a mixing baffle at the entrance of the duct. The main differences between this tunnel and the Cheng et al. (2004) tunnel are that a large, single HEPA filter is positioned at the duct opening to ensure only clean air is introduced into the system; the aerosol distribution system is positioned *after* the mixing baffle; and a small, counter-rotating fan is positioned just after the aerosol distribution system to distribute the aerosols. From this section, the aerosol-seeded air enters a constriction (which is another age-honored method of reducing initial turbulence; Pankhurst and Holder, 1952) where it moves unimpeded to the test section. At the back of the test section another large HEPA filter is fixed to ensure no fugitive particles enter the laboratory. Using this configuration, Lee et al. (2013) were able to achieve a wind velocity $C_{v\%}$ of no more than 5.7 percent and an aerosol concentration $C_{v\%}$ of no more than 8.7 percent.

Of equal importance to choosing flow conditioning techniques to establish sufficient mixing is choosing the measurement methods to analyze wind velocity and aerosol concentration profiles. 40 CFR 53.62 (USEPA, 1997) states that for wind velocity measurement, a method capable of 2 percent precision and 5 percent accuracy must be used, and mentions hot-wire anemometry specifically as a desirable method to achieve this. Indeed, multiple wind tunnel velocity profiles have been examined using some type of anemometer. Ranade et al. (1990) used a TSI System 1051-1 anemometer in conjunction with a TSI Model 1056 RMS mean-square, direct current voltmeter. The probe was calibrated using a TSI Model 1125 calibrator, which was used to create a calibration curve "linearized using the coefficients from a fourth-order least-squares polynomial fit of the original data" (Ranade et al., 1990). Multiple single-point measurements were then taken by inserting the probe into the test section at various points across the centerline (as well as above and below the centerline) over a number of days to ensure temporal as well as spatial velocity uniformity. Cheng et al. (2004) used a similar single-point anemometry technique (TSI velocity meter VelociCalc Model 8360-M). The cross section was divided into 16 equal areas, and velocity was measured with the probe at the centroid of each of these at least 7 separate times to gauge temporal as well as spatial uniformity. The 7 measurements were then averaged to establish the wind speed at each point, which were then compared to the overall mean wind velocity to determine the wind speed $C_{v\%}$. The 2013 Lee team adopted the 16-point anemometry method described by Cheng et al. (2004) for their velocity measurements as well.

An anemometric method not used in the above studies that is of particular interest is particle image velocimetry (PIV), a non-intrusive laser anemometry technique. PIV

interrogates an aerosol-laden flow field (usually artificially seeded by the experimenter) with “planar slices” of two dimensional laser light sheets (TSI, 1994). The aerosols in the planar slice are illuminated by the laser light, and their movement is then recorded by capturing and uploading to a computer a set of images from a charged coupled device (CCD) camera. Using software equipped with robust statistical analysis packages, the displacement of the illuminated aerosols is measured by first recognizing “tracer patterns” within the first raw image and tracking the pattern’s movement into the second image (Westerweel, 1997). Multiple patterns are identified within the flow field, allowing for the derivation of multiple velocity vectors from a single image (TSI, 1994). This allows for an instantaneous multi-point measurement by creating a velocity flow field from a single pair of images. If a modern CCD camera is used, multiple sets can be captured and processed over a set time (as many as the software or computer memory will allow), allowing for the creation of multiple velocity flow fields over that set time, each of which describes the instantaneous flow properties of the section at that instant. These velocity flow fields can then be averaged, creating an end product that describes both the spatial and temporal uniformity of the entire planar sheet. This offers decided advantages over single point measurement as it allows for extremely detailed, high-resolution analysis (both quantitative and qualitative) of flow fields (Normayati et al., 2012) without physically disrupting them.

The accuracy and uncertainty of PIV measurement has been the subject of continuing study involving sophisticated statistical analysis of various operating algorithms that is beyond the scope of this thesis. However, it is important to understand the origins of uncertainty when using the PIV system to minimize each elemental error

source. Wilson and Smith (2013b) set out to characterize the uncertainty of PIV measurements by comparing PIV algorithm output to velocities measured by hot-wire anemometry. The major sources of error identified were: density of the particles in the image; diameter of the seeded particles; particle displacement measurement (sub-pixel displacement); and velocity gradients (or shear) on the flow. The Wilson team then performed a surface-uncertainty analysis on two PIV algorithms using these four variables and found that their method performed reasonably well in estimating the difference between the hot-wire data and the PIV data. However, they found that the uncertainties for each algorithm were not related to one another, and that algorithm-specific uncertainty studies should be performed.

A 2012 study performed by Normayati et al. used the direct approach of comparing pitot-static tube data inside a wind tunnel to data gathered by a 3-D PIV. The flow was assumed to be fully developed at the test section as it was believed that sufficient hydrodynamic entry length was employed. The range of velocities obtained by the PIV system showed an average discrepancy of 0.8 percent from the pitot-static tube data, which was also in close agreement with calculated theoretical wind speed (1.2 percent discrepancy). The major sources of error identified in this study were found to be imperfect matching of coordinates between the laser sheet and the pitot probe; variation in particle image density; calibration precision; and variation in flow. These uncertainties can be separated into standard uncertainties (those affected by random error, such as flow variation) and systematic uncertainties (those that do not change with time and are considered constant as long as the experimental set up does not change; Normayati et al., 2012). Systematic errors may never be eliminated but can be anticipated and may be

minimized by using manufacturer's recommended best practices (TSI, 1994). As for standard uncertainties subject to non-linear, time and space varying uncertainties, it may be sufficient to assume that by increasing the time over which the area is being analyzed the influence of the random error would be diminished. Recent studies (Wilson and Smith, 2013a), however, show these errors can be and are propagated into the time averaged data and care must be taken not to dismiss them in certain applications.

The second major aspect of aerosol wind tunnel verification is the generation of monodisperse test aerosols at the aerodynamic diameters (how a particle behaves in a flow as related to a perfect sphere of pure water) specified in Table D-2 in 40 CFR 53.62 (USEPA, 1987) and Table 1 in this literature review. The CFR references the use of a VOAG to generate these test aerosols, and the VOAG is indeed a widely-used method in wind tunnel development (Ranade et al., 1990; Chen et al., 2004; Lee et al., 2013). The operational principles and application of a VOAG were described in detail by Berlund and Liu (1973). A VOAG works on the principle of the instability and break up of a cylindrical liquid jet when it is subjected to a mechanical disturbance generated at a constant frequency at sufficient amplitude. A solution is forced at a set flow rate through an orifice of a specified diameter (usually using a syringe pump), creating the jet. The mechanical disturbance is created by supplying an electrical current at a set frequency to a piezoelectric ceramic, which then interferes with the jet flow at that frequency, and breaks the jet into equal-sized droplets. The size of the droplets is highly dependent on: (1) the flow rate of the solution; (2) the frequency of the mechanical disturbance; (3) the diameter of the orifice hole, which determines the diameter of the liquid jet; and (4) the composition of the solution used. If the solution used is composed wholly of non-volatile

components, the diameter of the droplet can be calculated using the empirically developed equations from Berglund and Liu (1973) specific to a VOAG:

$$D_d = (\frac{6Q}{\pi f})^{1/3}$$

where D_d = droplet diameter; Q = liquid flow rate; and f = frequency of the mechanical disturbance. If the solution used is a ratio of non-volatile solute to a volatile solvent, the resulting aerosol diameter can be calculated as:

$$D_p = C^{1/3} D_d$$

where D_p = aerosol diameter and C = volumetric concentration of the non-volatile solute to the volatile solvent. The reasons for dissolving the non-volatile solute into a volatile solvent are two-fold: first, the technique of solvent evaporation makes it possible to create aerosols with a much smaller diameter than that of the orifice hole; and second, the orifice would quickly clog due to the viscosity of many non-volatile chemicals (Berglund and Liu, 1973). It is also necessary to account for any non-volatile impurities in the volatile solvent (the value of which is usually provided by the chemical manufacturer), using the equation:

$$D_{p,corr} = (1 + \frac{I}{C})^{1/3} D_p$$

where $D_{p,corr}$ = the aerosol diameter corrected for non-volatile impurities in the volatile solvent and I = volumetric fraction of non-volatile impurities in the solution. Finally, when applying a fluorescent tag to the solution for mass concentration measurement, the final equation (Faulkner and Haglund, 2012) is:

$$D_s = [\frac{6QC}{\pi f}\left(1 + \frac{C_u}{\rho_u} + \frac{I}{C}\right)]^{1/3}$$

where C_u= concentration (by mass, m/m) of the fluorescent tag in the non-volatile solute and ρ_u= density of the non-volatile solute.

Other considerations for creating monodisperse aerosols were discussed, including the importance of operational frequency ranges to generate the mechanical disturbance. Berglund and Liu (1973) found that at certain frequencies, non-uniform breakup of the jet occurred, resulting in satellite droplets. As such, it is necessary to perform a qualitative examination of the stream either by using strobe light to "freeze" the visual flow of the jet (Berglund and Liu, 1973) or by performing a deflection test (TSI, 2002). Additionally, because the droplets are highly charged when leaving the VOAG, some droplets quickly coagulate into multiplets, which are two or more droplets that have combined into a single droplet (doublets = twice the mass of a singlet, triplets = three times the mass of a singlet, etc.). By employing a Krypton-85 (Kr-85) radioactive neutralizer, the charge is reduced dramatically, resulting in far fewer multiplets. Even when employing the use of a radioactive neutralizer, the presence of multiplets is unavoidable, however they can be accounted for (Ranade, 1990). Using these methods, Berglund and Liu (1973) were able to achieve highly mono-disperse aerosols with a particle diameter accuracy of ±2 percent in routine operations.

Even though Berglund and Liu (1973) were able to achieve a ±2 percent accuracy, 40 CFR 53.62 (USEPA, 1997) requires that the aerosols generated by a VOAG be verified for both acceptable aerosol diameter and checked for an unacceptable percentage of multiplets (no more than 10 percent). To do this, it is necessary to collect liquid aerosols upon a slide coated with an oil-phobic substance using an aerosol impactor and physically verify the composition using a calibrated microscope. A major

consideration when performing this task is that after the spherical liquid droplet impacts the slide, the shape is changed to that of a flattened spheroid (Berglund and Liu, 1973) as a result of equilibrium between the droplet surface tension, interfacial forces, and gravity (Faulkner and Haglund 2012). It is therefore crucial to apply a flattening coefficient (F) when measuring these spheroids under the microscope to calculate the original diameter of the collected droplet by using the following equation from Faulkner and Haglund (2012):

$$D_s = \frac{D_a}{F}$$

where D_s= original spheroid diameter; D_a= apparent spheroid diameter; and F = flattening coefficient. Several studies have been conducted to determine the flattening coefficient with varying results. Olan-Figueroa et al. (1982) used a 2 percent solution of fluorocarbon oleophobic surfactant NyeBar Type CT to coat the slides, then calculated the average flattening coefficient of oleic acid droplets at F = 1.34. Liu et al. (1982) used the experimental surfactant L-1428 to coat the slides and calculated F = 1.429. The coefficients derived by Olan-Figueroa et al. (1982) have been primarily used in the past (Ranade et al., 1990; Chen et al., 2004), however as the commercial availability of these surfactants changes, it is necessary to calculate flattening coefficients for each new surfactant. Faulkner and Haglund (2012) conducted a study on the surfactant NyeBar Type L, which is still commercially available, and found that interfacial forces between the droplets and the coated slide can vary significantly with the chemical composition of the surfactant used. Using a confocal microscope, the three dimensional measurement of fluorescent-tagged oleic acid droplets was possible. The results of the study showed that the flattening coefficient varied not only with the surfactant used, but also with the

concentration of the fluorescent tag uranine in the oleic acid droplet. Table 2 summarizes Faulkner and Haglund's (2012) findings.

% Uranine	Flattening Coefficient
0	1.332 ± 0.007
5	1.297 ± 0.030
10	1.295 ± 0.009
20	1.205 ± 0.021

Table 1: Flattening Coefficients using Nyebar Type L Surfactant by percent Uranine (Faulkner and Haglund, 2012)

Once the quality of the aerosol is verified to comply with 40 CFR 53.62 (USEPA, 1997), the concentration profile of the aerosol wind tunnel can be tested and $C_{v\%}$ values for each replicate point can be calculated (Ranade et al. 1990). Chen et al. (2004) achieved this by installing a "rake" of 5 isokinetic samplers each holding glass fiber filters across the applicable cross section and exposing them to VOAG-generated oleic acid droplets of 10 µm diameter tagged with fluorescent tracer at wind velocities of 0.56, 2.2, and 6.6 meters per second (m/s). The flow rate through the isokinetic samplers was held constant and monitored to ensure isokinetic conditions at the sampler inlets. Once the test was complete, each isokinetic nozzle was rinsed with a 50 percent isopropyl alcohol and 50 percent distilled water solution (by volume, v/v) to recover the fluorescent-tagged oleic acid that had impacted upon the inner walls. The filters from each sampler were placed in more alcohol / water solution to extract the tracer from the glass fiber, and approximately 6 milliliters of 1N Sodium Hydroxide (NaOH) was added

to each liquid sample so the fluorescence of the tags would stabilize. A Sequoia-Turner Model 450 fluorometer was then used to quantify the concentrations in each sample. Lee et al. (2013) used a nearly identical method, the only difference being the model of fluorometer used (Thermo Scientific Quantech FM109515). Table 3 summarizes the findings from the two studies.

	Chen et al (2004)			Lee et al (2013)		
Wind Speed (m/s)	0.56	2.2	6.6	0.56	2.22	6.67
Cv(%)	7.5	9.1	7.5	8.7	6.5	7.9

Table 2: $C_{v\%}$ Aerosol Concentration Values by Wind Speed (Chen et. al, 2004 and Lee et. al., 2013)

Once the wind tunnel has been modified, tested, and verified as having acceptable C_v values for wind velocity and aerosol concentration, according to the USEPA (1997) it can now be used to characterize particulate matter Federal Reference Method (FRM) samplers. Indeed, Lee et al. (2013) went through this process in order to test the performance of ambient PM_{10} inlets and determine the 50 percent cutoff diameter for sampling efficiency (Lee et al, 2013), which was the original purpose of establishing these procedures (Ranade et al, 1990). While this is the aim of the USEPA, compliance with the rule provides for a vetted facility in which to test the performance of samplers not necessarily intended to become FRMs. As a case in point, the final goal of the 2004 Chen team was to test a massive flow air sampler designed for aerosol sampling of radioactive pollution associated with nuclear accidents, not to create an aerosol dispersion wind tunnel specifically for particulate matter FRM characterization. Nevertheless, the Chen team used the same methods and standards specified in Subparts D and F of 40

CFR 53 (USEPA, 1987 and 1997) to characterize the velocity and aerosol concentration profiles within the test section of their wind tunnel, as the uniformity of these elements was crucial to calibrate their sampler properly. Therefore it is appropriate to use such an aerosol wind tunnel in the characterization of multiple types of particulate matter monitoring / analysis mechanisms, such as nephelometers designed to measure the mass concentration of particulate matter in an emission cloud via indirect methods (i.e. Mie scattering of a laser beam caused by suspended aerosols) instead of the direct collection efficiency of a traditional FRM sampler.

The goal of this research is to use the principles described above to characterize the EQRTL Aerosol Dispersion Wind Tunnel for mean velocity and aerosol concentration distribution throughout the applicable cross section of the test chamber. Chapter 3 describes, in detail, how a TSI PIV Laser System was used to interrogate the test area to non-intrusively determine the cross sectional velocity profile by calculating the $C_{v\%}$ from nearly-instantaneous velocity flow fields. In addition, the following chapter will describe how an isokinetic rake equipped with isokinetic sampling cones was used to calculate the aerosol $C_{v\%}$ within the flow.

CHAPTER 3

MATERIALS AND METHODS

Using the research discussed in Chapter 2 as guidance, the wind velocity profile and aerosol concentration distribution of the EQRTL Aerosol Dispersion Wind Tunnel were both characterized using the methods described below. A major difference between previous methods and those used in this thesis is the employment of a TSI PIV laser system to calculate the velocity flow fields across the applicable cross section instead of taking point anemometry measurements. This provided exceptional velocity data resolution that surpassed the specified standard of no fewer than 12 discrete velocity measurements throughout the cross section (USEPA, 1987 and 1997). In addition to velocity distribution characterization, the aerosol concentration profile was determined by capturing generated test aerosols tagged with a fluorescent tracer using isokinetic sampling cones and glass fiber filters. The filters were soaked in an aliquot and a fluorometer measured the concentration of tracer present in the solution. The concentration of fluorescent material present in each sample was used to calculate the aerosol concentration within the test section over the sampling time at each cone position.

3.1 Velocity Profile Characterization of EQRTL Aerosol Dispersion Wind Tunnel Test Section Using a TSI PIV Laser System

As stated in 40 CFR 53 (USEPA, 1987 and 1997), an aerosol wind tunnel used to test the sampling efficiencies of Federal Reference Method (FRM) particulate matter

samplers must have a uniform wind velocity profile where no discrete measurement point differs by more than 10 percent of the overall mean velocity. In addition, the method used to make the velocity measurements must be capable of a precision and accuracy of 2 percent and 5 percent, respectively, or better. Previous researchers (Ranade et al, 1990; Cheng et al, 2004; Lee e. al, 2013) have used hot-wire anemometry methods to achieve this goal, as it is a proven technique capable of the prescribed criteria. However, for this research, a Solo PIV class four, neodymium-doped yttrium aluminum garnet (Nd:YAG) Laser System (TSI, Inc) was used to illuminate seed aerosols entrained in the airflow, measure the displacement of the illuminated aerosol patterns between image pairs, and calculate velocity vectors within the instantaneous horizontal velocity flow fields within the applicable cross section. The applicable cross section was defined as the inner 75 percent (457 mm) of the circular cross section (609 mm) of the to avoid boundary layer effects during characterization and testing. A total of 13 time-averaged flow fields were calculated across five horizontal chord lines (Chords A through E) evenly spaced at 114 mm along the vertical axis, providing extremely detailed analysis of the velocity profile at these levels. Each chord line was broken into subsections, the number of which was defined by the CCD camera's field of view when focused upon the interrogation region (subsections A1 through E2). Figure 1 details the interrogation regions within the cross section.

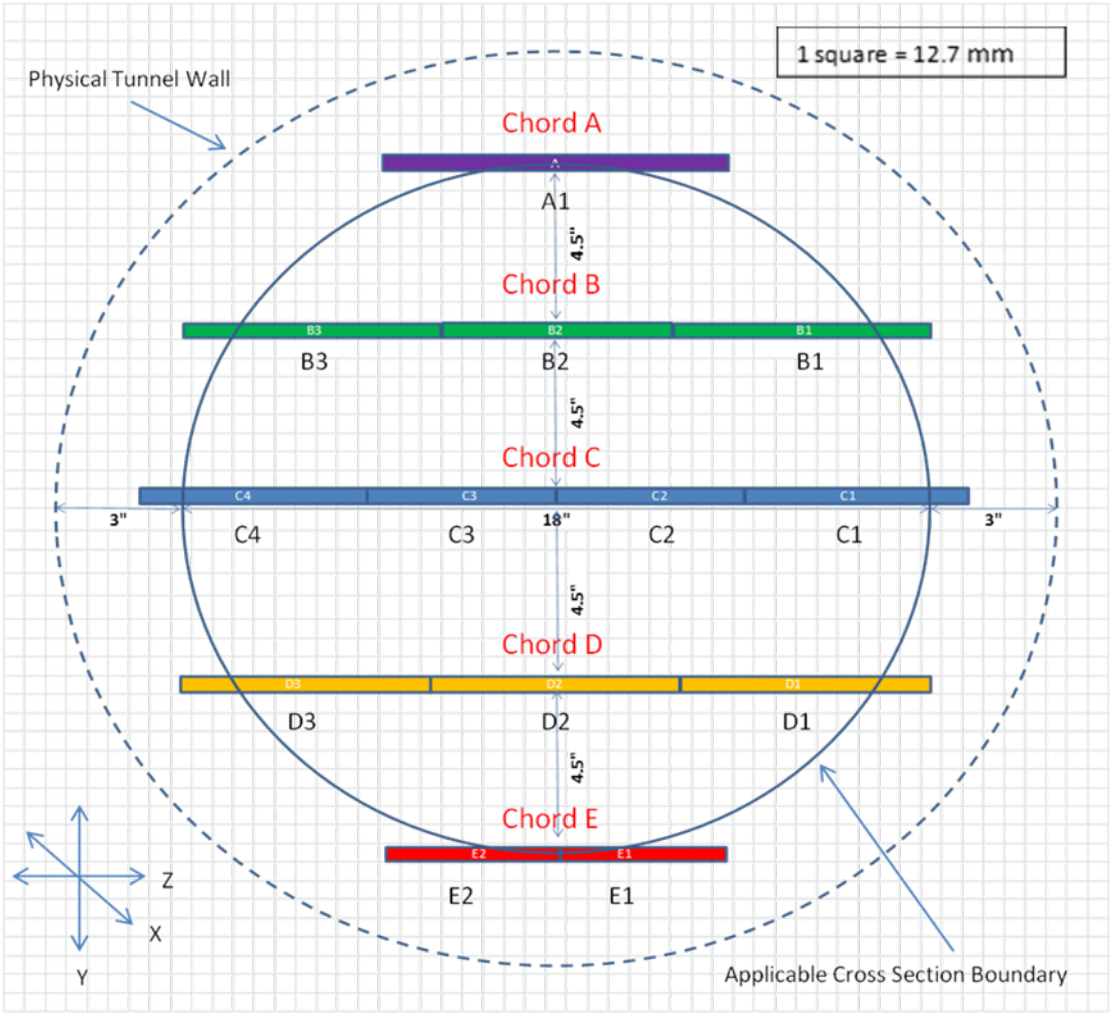

Figure 1: Detail of Chords and Subsections through the Applicable Cross Section

The dashed outer circle represents the physical wall of the wind tunnel. Only the inner seventy-five percent (457 millimeters) of the cross section was defined as the testing area to avoid boundary layer effects, as represented by the solid line. The five chords are designated as A, B, C, D, and E, with the top-most chord as A.

3.1.1 The EQRTL Aerosol Dispersion Wind Tunnel

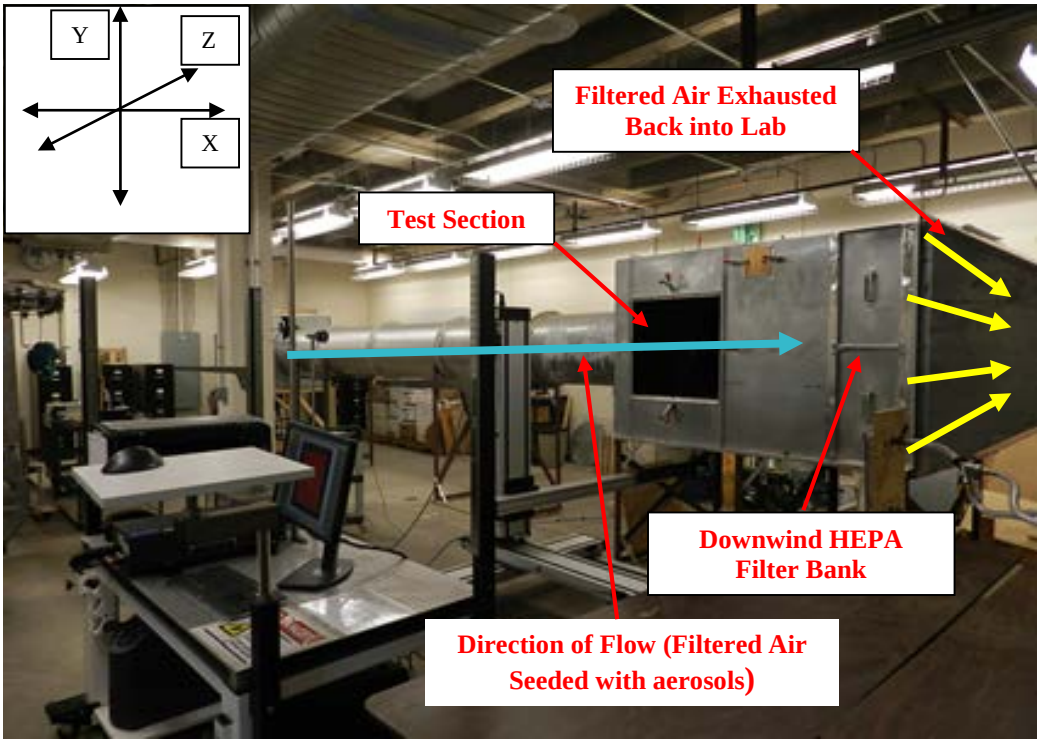

Figure 2: EQRTL Aerosol Dispersion Wind Tunnel (Downwind View)

The EQRTL Aerosol Dispersion Wind Tunnel draws unfiltered ambient air through the upwind HEPA filter bank and into the filter box (shown in Figure 3 below) where it is seeded with aerosols. The seeded filtered air is then drawn through the tunnel section and into the test section (shown by blue arrow). As the air exits the test section, it passes through the downwind HEPA filter bank, exhausting only filtered air (shown by yellow arrows) back into the lab. The X axis runs the length of the tunnel (direction of the wind flow, through the test section), the Y direction is the vertical axis across the test section and the Z is the horizontal axis across the test section.

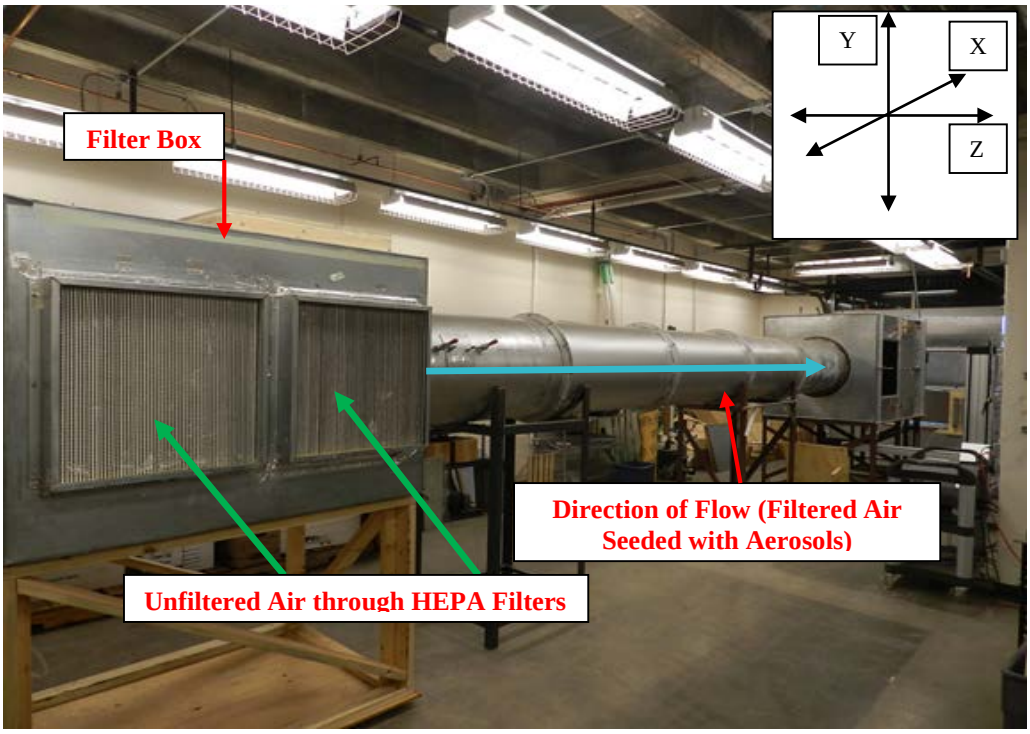

Figure 3: EQRTL Aerosol Dispersion Wind Tunnel (Upwind View)

Unfiltered ambient air is drawn in through the upwind HEPA filter bank (two of four HEPA filters pictured) as shown by the green arrows, into the filter box where it is seeded with aerosols. The seeded air (shown with the blue arrow) is then drawn down the tunnel section providing seeded filtered air to the test section. The X axis runs the length of the tunnel (direction of the wind flow, through the test section), the Y direction is the vertical axis across the test section and the Z is the horizontal axis across the test section.

The majority of the EQRTL wind tunnel is constructed of sheet metal. It has a circular tunnel section with a diameter of 0.61 m, which expands to a 1.83 m x 1.22 m x 1.22 m rectangular test chamber box. On each side of the box is a 0.686 m x 0.686 m access panel, which can be fitted with Plexiglas windows for observation. Housed within the back wall of the testing chamber are four 0.603 m x 0.60 m x 0.292 m HEPA filters, each capable of removing 99.97 percent of particles 0.1 μm and larger with a flow rate up to 1800 cubic meters per hour (m^3/hr), so that only filtered air is exhausted back into the laboratory. These filters also serve to eliminate any swirl that would otherwise be

propagated back into the chamber by a 0.6858 m square inline Fantech FSD 26 duct fan, which is bolted to the back of the testing chamber to pull the air through the tunnel. The fan is capable of an 11,800 m^3/hr flow rate at zero static pressure (Fantech 2012), and is controlled by a Dayton 3HX74 AC variable frequency drive (VFD). Housed within the tunnel section immediately downwind of the inlet filter box is a Turbulator mixing device (Air Blender, Inc.), which consists of two concentric rings of wind vanes, each generating swirl counter-directional to the other. In addition, to eliminate artificial swirl caused by the Turbulator, a wooden disk flow straightener with a porosity of 50 percent is positioned 1 diameter downwind of the mixing device. See Appendix D for additional information on wind tunnel modifications.

Figure 4: FSD26 Fan (Side view with VFD, left, and Front View, right)

3.1.2 The Particle Image Velocimetry (PIV) Laser System

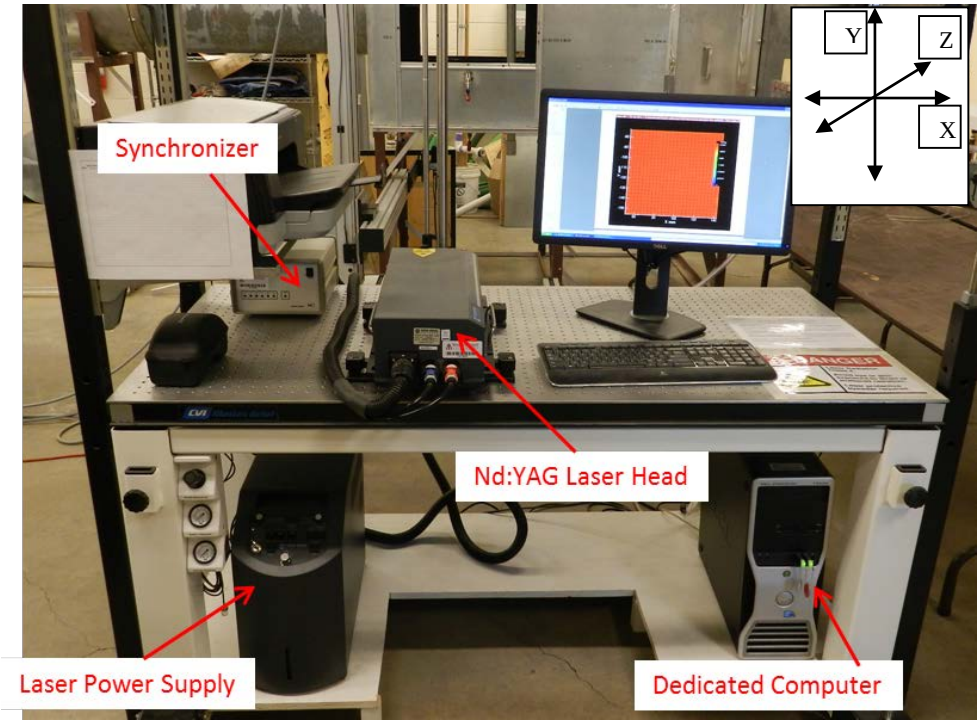

Figure 5: PIV Laser System

Figure 5 shows four of the five main components to the PIV Laser System used in this research: the laser power supply, which also houses the distilled water reservoir used for laser cooling; the Nd:YAG laser head, which emits the laser pulses; the synchronizer, which is the coordinating element between the laser fire and the CCD camera (not shown) set by the user; and the dedicated computer, which allows the user to set the timing conditions (Δt between laser pulses), collects imagery sent by the CCD camera, and to analyze collected data.

The PIV Laser System (TSI, Inc.) used in this research was a multiple-component system that illuminates aerosols seeded within a flow with a two-dimensional laser light sheet from a class four Nd:YAG laser. A CCD camera positioned below the test section captures the scattered light from the illuminated droplets entrained within the airflow which are digitally imaged using imagery software on a dedicated computer. By pulsing the laser at a known interval (Δt), image pairs are created and the displacement of the droplets between the two images can be measured. From the displacement values and the

known Δt, a nearly-instantaneous velocity flow field can be calculated. Multiple image pairs were taken for each test, and their corresponding velocity flow fields were averaged over a sufficient time period (approximately two minutes) to account for transient eddies to pass through the test section. This provided a single time-averaged velocity flow field representative of the flow within each chord subsection. The following paragraphs describe the processes and equipment in more detail.

Because the cross section of the tunnel was interrogated along the Y-axis, and because it is unwise and impractical to constantly move the laser itself, it was necessary to manipulate the height of the beam using an RS99 periscope assembly (Thorlabs, Inc.) consisting of two 45-degree mirror mounts that can be adjusted and locked at desired heights along a vertically mounted 25.4 mm diameter post (Thorlabs, Inc.). The bottom mount (part # RS99B) holds a 25.4 mm diameter, 3.2 mm thick and 45-degree angle-of-incidence Nd:YAG front surface mirror designed to divert the fundamental and second harmonic wavelength (λ) of the class 4 laser (λ=532 nm and 1064nm, respectively) 90 degrees up to an identical mirror in the second mount (part # NB1-K13, Thorlabs, Inc). The top mount (part # RS99T, Thorlabs, Inc) is equipped with adjustable knobs for pitch, yaw, rotation, as well as an up-to-4-degree tilt. The entire periscope assembly was mounted securely to a Melles Groit CVI optics table (Model # 590386-13). Directly in front of the top mirror, an elliptical lens was mounted on a second secured post, which focused the beam into a two-dimensional sheet of laser light.

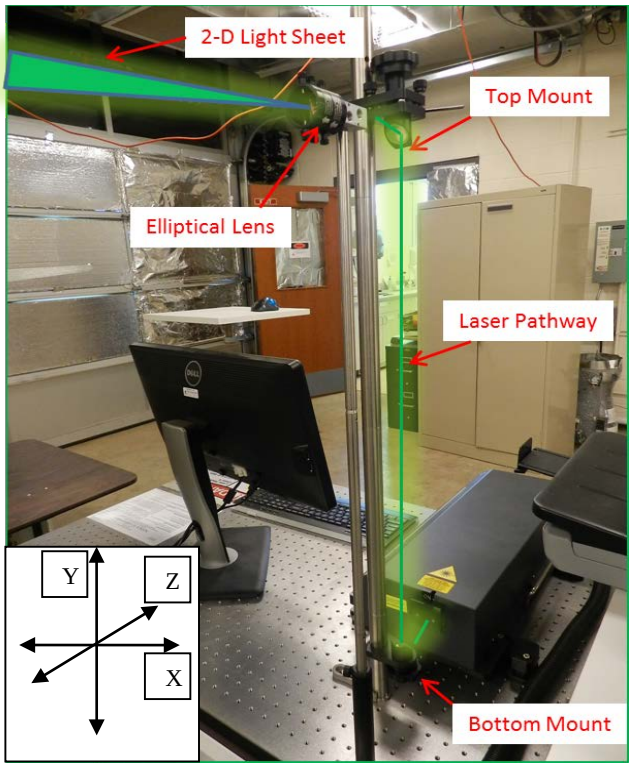

Figure 6: Periscope Assembly and Laser Pathway

The laser light beam (shown with green lines) is emitted from the laser head and encounters the bottom mount. The front surface mirror held in the mount diverts the light 90-degrees up to the top mount. The second front surface mirror again diverts the light 90-degrees out through the elliptical lens, which flattens the light beam into a two-dimensional light sheet. The top mount and elliptical lens can be adjusted vertically along their respective posts, allowing the experimenter to interrogate chord lines along the Y-axis across the applicable cross section in the tunnel test section.

The 4 megapixel (MP) camera (TSI Model 630059 PowerView Plus 4MP PIV Camera), which has a 2048 x 2048 pixel resolution (pixel size of 7.4µm by 7.4µm) and operates at 16 frames per second with 12-bit output (TSI, 2005), was mounted on the traverse system looking up through the acrylic window installed in the bottom of the test section, where it could image the aerosol field entrained within the flow using a Nikon AF Nikkor 50 mm f/1.8D lens. The EQRTL also has an 11MP camera that would yield a higher resolution for image processing, thus resulting in a lower uncertainty of velocity measurements (more pixels / mm, which would increase the precision of the point source

computation of the CCD array and hence the accuracy of aerosol displacement measurement). However, the 11MP camera naturally requires far more memory space than the 4 MP camera, and the uncertainty associated with the 4MP camera was considered acceptable for this application. See Appendixes A and B for more information on PIV uncertainty.

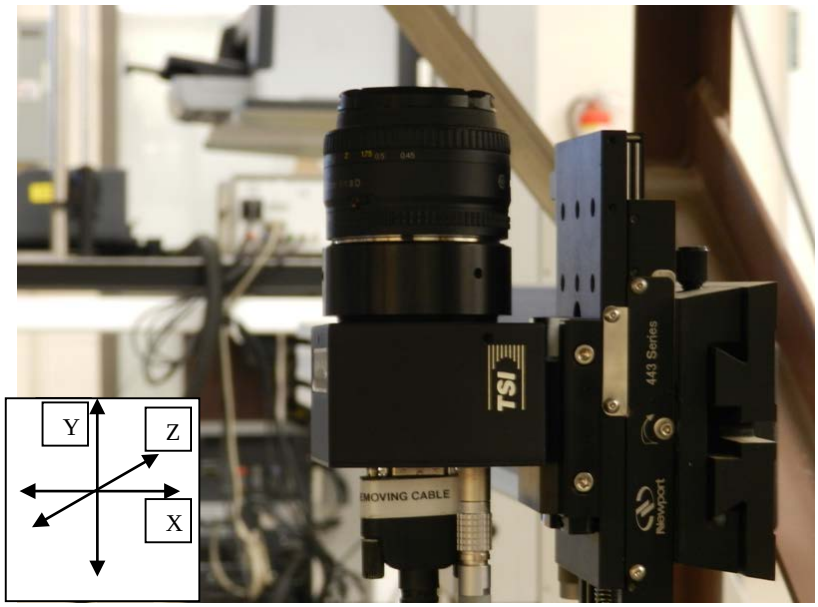

Figure 7: 4MP CCD Camera with 50mm Nikon Lens

The camera and lens was mounted on the traverse system which allowed for movement along the Z-axis beneath the test section.

The Δt setting is of great importance. The Insight 3G imaging software (Insight, Inc), using statistical analysis, tracks aerosol patterns rather than individual particles between image pairs. If too much time has passed between images, (too high of a Δt), then the droplet patterns have potentially deformed to the point that the software cannot recognize them between images. If too little time has passed between images, (Δt too low), then the software may not recognize that any movement has occurred. TSI, Inc.

(1994) therefore suggests that a Δt be selected that results in aerosol displacement of 5 to 15 pixels.

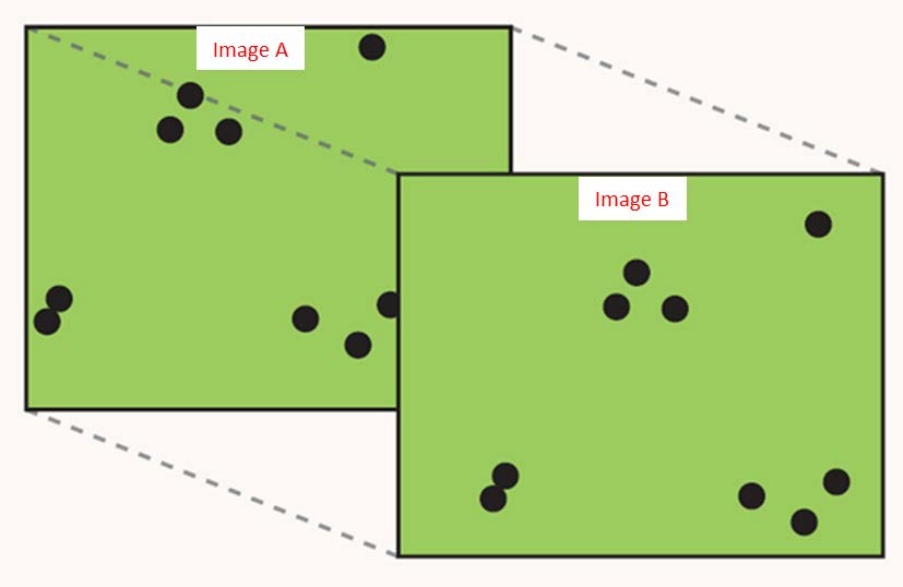

Figure 8: Example of Aerosol Groupings between Images (TSI, Inc., 2007)

The image pair shown depicts aerosol groupings and how they travel over a set time, Δt, between image A and image B. The displacement in pixels is measured by the Insight software using statistical analysis.

Once the Δt is set, the experimenter initiates an interrogation sequence using the Insight software that will create a single image pair. A synchronizer unit (Laser Pulse Synchronizer 610035, TSI Inc.) coordinates the first laser pulse with the CCD camera shutter, creating the first image of illuminated aerosols within the flow. After the selected Δt, the second pulse is fired, again coordinated with the camera.

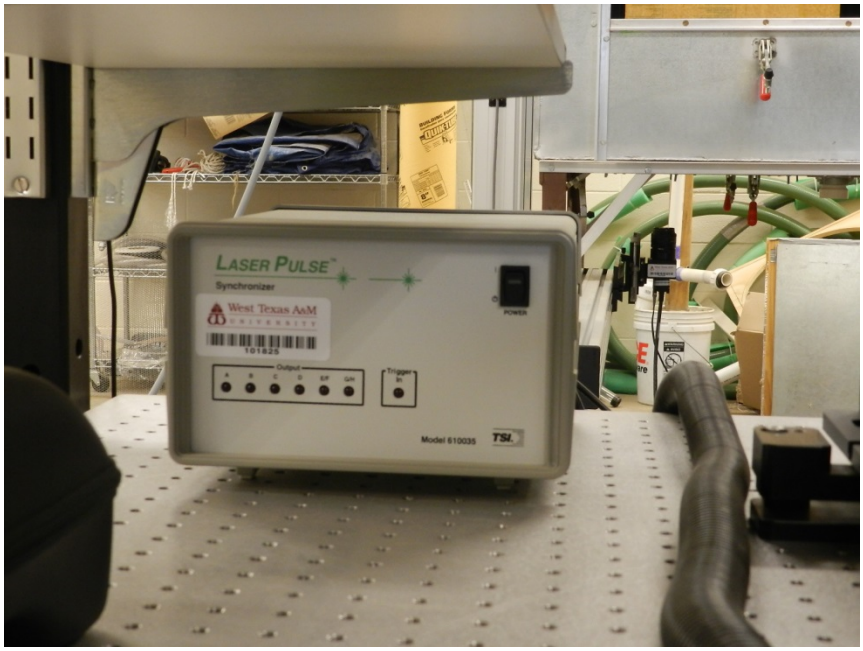

Figure 9: Laser Pulse Synchronizer

The laser pulse synchronizer coordinates the laser pulses over the set Δt with the CCD camera shutter, creating an image pair of illuminated aerosols within the flow.

These images are uploaded via a firewire cable and saved on the dedicated system computer (Dell Precision T5500), where the experimenter can then analyze the image pairs using the statistical analysis program included in the Insight software package as described above and calculate the velocities of the aerosol groups ($V = \frac{\Delta s}{\Delta t}$, where V = velocity and Δs = displacement). The information from these calculations is combined into a single analysis file (or vector file) for each image pair. Using these analysis files, nearly-instantaneous velocity vector flow fields are mapped and can be viewed and analyzed by the experimenter with either Tecplot (Tecplot, Inc) or MATLAB (MathWorks, Inc) post-processing programs, both of which are compatible and work in conjunction with the Insight 3G software package. If multiple image pairs are captured

and analyzed over a run time, a single time-averaged velocity flow field analysis file can be generated using Tecplot.

Before any of this can be accomplished, however, the experimenter must first perform a calibration to establish a pixel to length value. This is accomplished by placing a reference device (i.e. a National Institute of Standards and Technology, or NIST, traceable ruler) into the laser sheet.

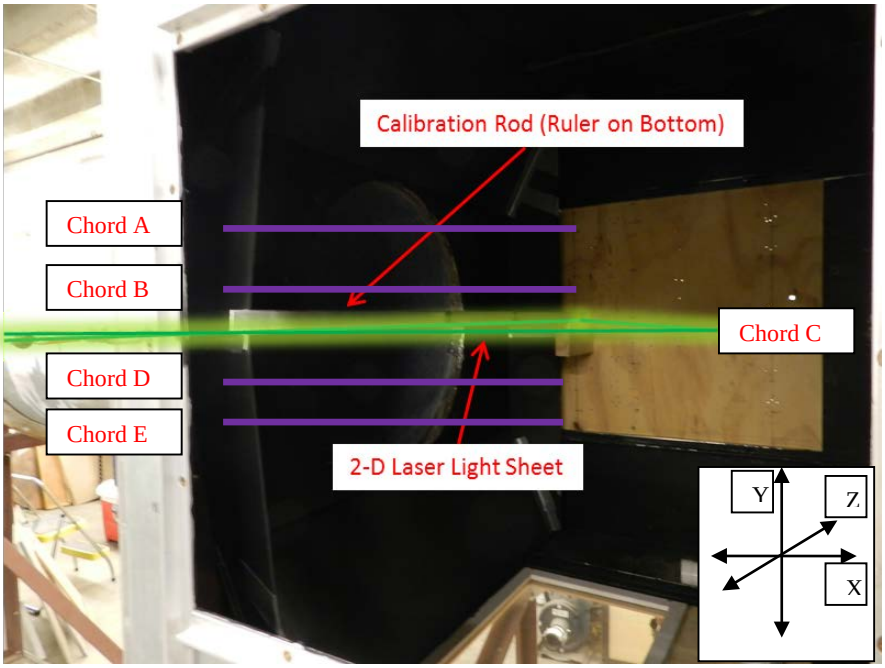

Figure 10: Calibration Setup with Light Sheet Illuminating the Ruler

The two-dimensional laser light sheet is aligned with the ruler, which is positioned across the desired chord line (chord C pictured) of the test section to ensure the intended region is being interrogated. Chord lines are depicted here with by the evenly-spaced purple lines. The camera lens is focused on the ruler, and a calibration image is captured.

The CCD camera is focused on the reference device by the experimenter, who initiates a calibration image sequence, which uploads the calibration image to the computer. The experimenter opens the image file and performs a calibration on the

image by clicking and dragging across a known distance, which the software equates to a number of pixels.

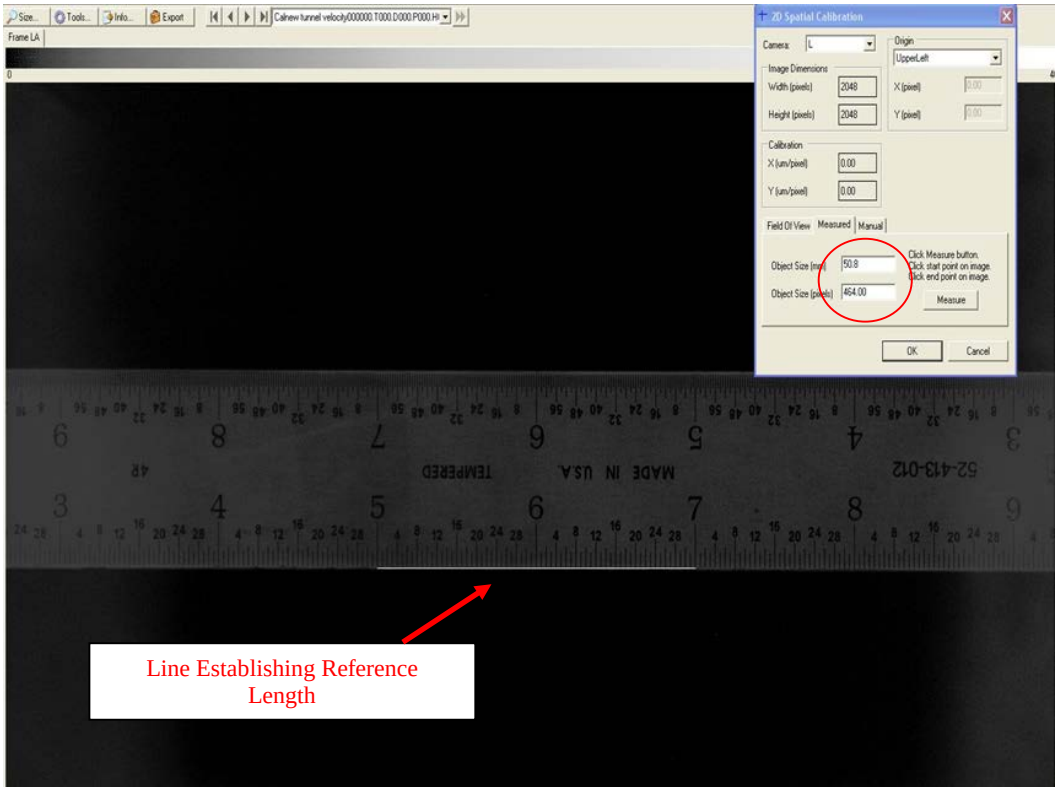

Figure 11: Calibration Image Example

The white line between the 5 and 7 inch markers at the bottom of the ruler shows the "click and drag" line over a 50.8 mm reference length; the fields inside the red circle in the upper right hand corner of the image shows how the pixel length is converted to pixels. Here it equates 464 pixels to 50.8 millimeters, as defined by the white line along the edge of the ruler.

It should be noted that this calibration is highly dependent on the experimenter's ability to click accurately on the desired reference points. In this research, it was found that the calibration should be performed multiple times and over a longer, rather than shorter, reference length. See Appendix A for more information on the PIV calibration and sources of uncertainty.

The above procedures were tested against pitot probe / analog manometer velocity measurements to ensure the PIV method satisfied the velocity measurement device accuracy and precision requirements stated in 40 CFR 53.62 (USEPA, 1997). The Solo PIV Laser System, when compared to the pitot probe data as an original principle reference, has an average estimated accuracy of 4.12 percent and an average precision of 1.87 percent across the two target testing velocities and all chord lines, both of which satisfy the requirements of 5 percent and 2 percent, respectively. While the accuracy remained fairly constant across all tests, the precision varied significantly with experimental setup. See Appendix A for more information on PIV uncertainty analysis and precision, and Appendix B for PIV accuracy tests.

Once the PIV method was verified as sufficiently accurate and precise, the system was set up to analyze the velocity profile of the applicable cross section inside the testing chamber (which was defined as a circular section with a 0.46 m diameter, approximately 0.3 m downwind of the tunnel section exit into the testing chamber, and centered over the bottom access door to allow for CCD imaging) as shown in Figure 1. A Cartesian coordinate system provided the cross sectional area positional reference, with the origin at the center of the section. The CCD camera was mounted on a traverse system (Isel Automation) which was used to maneuver the camera primarily in the X direction (Y and Z directions remained constant). The subsections of the individual chords were sized according to the CCD camera field of view when focused on a particular chord height. For instance, for Chord A, when the CCD camera was centered (X=0), the long focal distance (approximately 838mm from camera lens) yielded a field of view sufficiently large to cover the entire chord. By contrast, when focused on and imaging Chord D,

multiple subsections were needed to cover the entire area of interest as the shorter focal distance (approximately 495 mm from camera lens) yielded a smaller field of view. Each time a new chord was interrogated, a new calibration image had to be taken, as this changed the pixel/mm calibration value.

3.1.3 Velocity Characterization of the Cross Section

The EQRTL Aerosol Wind tunnel was first characterized across the C chord only to determine if any modifications to the wind tunnel were needed. This test showed that modifications were indeed necessary (see Appendix C for procedures and results of initial cross section velocity tests and Appendix D for a description and discussion of all tunnel modifications). After the necessary physical modifications to the tunnel were completed, the velocity profile was again characterized at two target wind speeds of 2 km/hr (approximately 0.556 m/s) and 8 km/hr (approximately 2.22 m/s). These wind speeds are described as "target" velocities because it is not necessary for the total mean velocity to equal 2 km/hr and 8 km/hr exactly; the overall mean need only be within 10 percent of the target for the test to be considered official when testing a candidate FRM sampler (EPA, 1997). This research strives to meet these goals as closely as possible; however failing to meet this requirement does not nullify the characterization of the tunnel itself. As mentioned in section 3.1.1 of this chapter, the FSD 26 Fan is controlled by a VFD. The frequency range of the VFD is 0.00 to 60.00 Hz. A TSI VelociCheck Model 8330 anemometer was originally used to create a rough VFD setting (Hz) to wind speed (m/s) calibration curve. The results of this calibration were used to estimate the VFD frequency setting for the 2 km/hr (15 Hz) and 8 km/hr (31 Hz) target velocity

characterization tests. Table D-2 in 40 CFR 53.42 (USEPA 1987) specifies the need to test at 24 km/hr as well, but the tunnel as configured (with HEPA filters and a Fantech FSD 26 duct fan) was not capable of achieving this speed inside the tunnel section. Using the TSI PIV Laser System, two individual runs of 60 image pairs over two minutes each (1 pair per two seconds) were taken at every subsection (A1-E2), resulting in 120 images taken over a four minute span at each subsection, thus allowing sufficient time for any transient features in the flow to pass. For the 2 km/hr and 8 km/hr tests, Δt settings of 1200 microseconds (μs) and 240 μs were used, respectively. These settings yielded displacements of 5 to 15 pixels between paired images, which resulted in an excellent percentage (>99 percent) of "true" vectors per calculated velocity field. The percentage of "true" velocity vectors is a direct function of the software's ability to track seed aerosol patterns from one image to the other with high statistical confidence, which is achieved when the trajectories over a sufficiently small sample time are nearly straight with a constant velocity (TSI 1994). The flow was seeded with oil-based liquid aerosols produced by a theatrical fogger (Chuvet Hurricane 1100).

The droplets produced were polydisperse and very small (geometric mean diameter [GMD]) was < 0.5 μm as measured by the Aerodynamic Particle Sizer, or APS, see section 3.2.2 for details). The fog was injected through a port in the back of the inlet filter box, immediately upwind of the entrance to the tunnel section and the turbulator. Due to the low inertia of the small droplets, they faithfully followed excursions in the flow field. This allowed for accurate flow visualization and displacement.

Figure 12: Theatrical Fogger

Fogger used to seed the aerosol wind tunnel with oil-based droplets for PIV interrogation. Pictured here with remote control.

The flow rate of the fogger provided a sufficient aerosol concentration in the test chamber for excellent PIV image density. The fogger was triggered by remote control at the beginning of each data run and re-triggered every twenty seconds for a nearly-continuous flow seeding. The subsections were interrogated in order, starting with A1. After the images were taken from a subsection and uploaded to the computer, the camera was moved in the Z direction along the chord line to the next position. Once the interrogation of an entire chord line had been completed, the NIST traceable ruler was repositioned inside the test chamber across the next chord line, the laser light sheet optics were adjusted to illuminate the new planar sheet, the camera was re-focused on the new

ruler position (using the numbers on the ruler to determine image clarity), and a new calibration image was taken. A new experiment file was created in the software and the subsections were interrogated again in order.

Once the images were captured and stored, the following procedures were followed to analyze the velocity flow fields at each subsection.

1. Velocity flow field vectors were calculated using the Insight software, creating an individual vector file for each image pair.

2. The individual vector files were opened in the Tecplot program, and a new single average velocity vector file was created, one for each subsection.

3. Using the data extraction tool, 50 discrete data points were taken along the Z axis of each subsection's average velocity flow field and exported to a text file. Each data point described an average velocity vector, complete with the *u* and *v* components of the vector (velocity in the X and Z directions, respectively), as well as the velocity magnitude of the vector, which combines the *u* and *v* components and describes the overall velocity as well as direction. Only the *u* velocity component was used in this research, however, as that was the direction of the flow.

4. The image-specific coordinates of each extracted data point were converted to the overall Cartesian coordinate system describing the entire cross section and effectively "stitched" together to create evenly-spaced, continuous data points across an entire chord line.

5. The point averaged velocities served as the data points to map the flow field across the entire section. For chords A and E, only the single data point at the

center of the chord was used, as defined by the 0.457 m cross section. Statistical analysis was performed on the data points as a whole to establish the mean velocity ($\bar{u}$) and the standard deviation of the velocity measurements (s_u) of the cross section. These values were in turn used in the following equation to determine the overall $C_{v\%}$.

$$C_{v\%} = \frac{s_u}{\bar{u}} * 100$$

3.2 Aerosol Concentration Characterization

The second phase of this research was to ensure that the aerosol concentration profile of the defined cross section complied with the USEPA standards promulgated in 40 CFR 53 Subpart D (USEPA, 1987) and Subpart F (USEPA, 1997). The methods for conducting these compliance tests are also described in the above regulations. For this phase, the procedures discussed in the Chapter 2 used by Ranade et al. (1990), Chen et al. (2004) and Lee et al. (2013) were followed. Monodisperse oleic acid aerosols tagged with uranine were generated with the use of a VOAG (TSI Model 3450), the functionality of which was verified as sufficiently precise (generating droplets with an aerodynamic diameter within 2 percent of the target aerodynamic diameter, see Berglund and Lieu, 1973) and generating no more than 10 percent multiplets per the standard set by regulation (USEPA, 1997). The process and results of this VOAG verification are detailed in Appendix E.

Figure 13: Vibrating Orifice Aerosol Generator (VOAG)

VOAG used to generate highly monodisperse oleic acid droplets tagged with fluorescent uranine tracers.

Once the VOAG verification was complete, a "rake" fitted with four isokinetic samplers (see section 3.2.2 for description) was used in conjunction with the VOAG to determine the spatial uniformity of aerosol concentration over a sampling period. Borosilicate glass fiber filters housed within the samplers (Figure 19) collected the uranine-tagged droplets, and a fluorometer (Turner Designs Model 10AU-005-CE) was employed to determine the mass concentration of the uranine collected upon them after a run time sufficient for analysis (see section 3.2.4). Using the concentration values determined from the fluorometer, the $C_{v\%}$ for the concentration profile was calculated to ensure it fell below the threshold set in the CFR (USEPA, 1987 and 1997).

3.2.1 Vibrating Orifice Aerosol Generator (VOAG)

The TSI Model 3450 VOAG is capable of generating highly monodisperse liquid droplets via the principles described in the Chapter 2 and by Berglund and Lieu (1973). Per 40 CFR 53.62 (USEPA, 1997), in order for the test aerosols to comply with the regulation, the geometric standard deviation for the target particle size being generated must not exceed 1.1. The geometric standard deviation is the standard deviation of a population around the geometric mean. The purpose of using the geometric mean instead of the more common arithmetic mean is to minimize the influence of outliers for a more precise approximation of the central tendency of a log-normally distributed (which VOAG-generated aerosols for the most part are) data set. The geometric mean (μ_g) of a data set $\{x_1, x_2 \dots x_n\}$ can be calculated by multiplying the sample values together and taking the n^{th} root of the number of samples (Wilson and Martin, 2006):

$$\mu_g = \sqrt[n]{x_1 * x_2 * \dots * x_n}$$

or

$$\mu_g = \prod_{i=1}^{n} x_i^{\frac{1}{n}}$$

The geometric mean (σ_g) is also the arithmetic mean of the log-transformed data within the population. Therefore the geometric standard deviation is given as:

$$\sigma_g = \exp\sqrt{\frac{\sum_{i=1}^{n}(ln\frac{x_i}{\mu_g})^2}{n}}$$

In addition to the geometric standard deviation constraint, the droplet-laden test atmosphere cannot contain more than 10 percent multiplets (particles with two or more times the mass) of the target droplet size. Appendix E describes the particle size

verification guidelines set in 40 CFR 53.62 (EPA, 1997) and the test procedures used to ensure this criteria was met when using the VOAG.

Once the operational procedures for using the VOAG were verified as producing monodisperse aerosols compliant with the regulation, the generator was located at the inlet filter box, which had been modified to receive generated aerosols through a port via vacuum hose. This port was cut at the center of the rear wall so the entry of these aerosols would be as spatially symmetrical as possible, lowering the likelihood of any directional bias that might affect the concentration profile downwind.

3.2.2 Aerodynamic Particle Sizer

The TSI Model 3321 APS uses time-of-flight sensing technology to calculate the aerodynamic diameter and light-scattering intensity of particles passing through the sensor chamber (TSI 2009). The particles are drawn into the centerline of a sheath of air, which accelerates the aerosols as they pass through two focused laser beams.

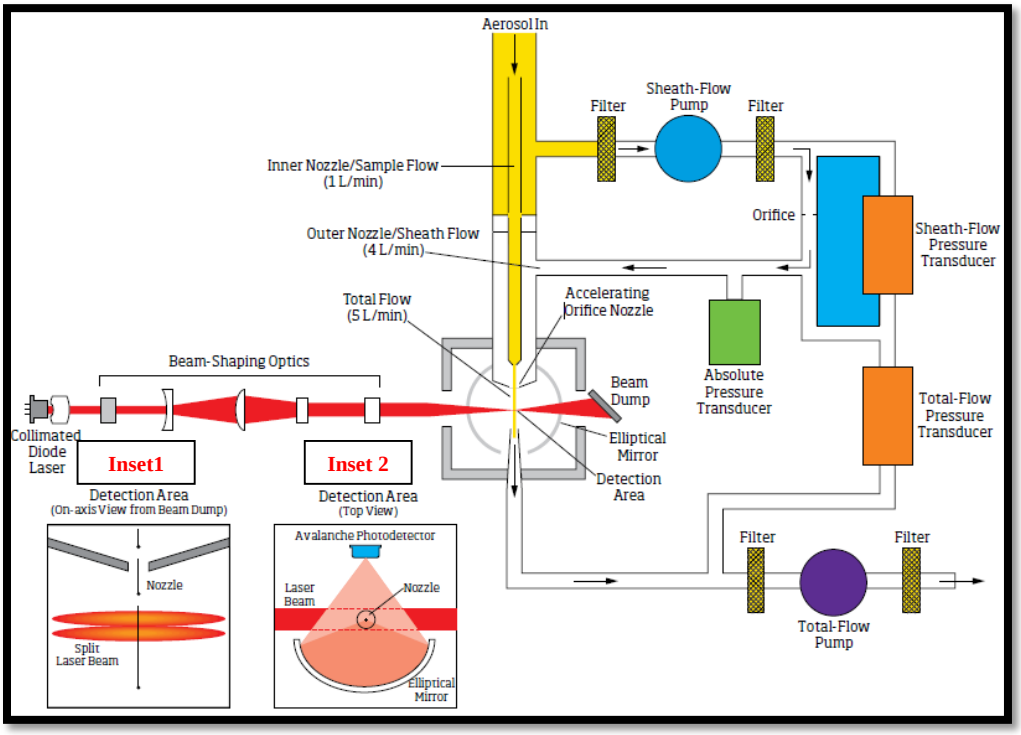

Figure 14: APS Theory of Operation Diagram
(TSI Inc., 2012)

The detail describes the flow path of the particles as they enter the APS. The droplets are accelerated as they exit the inner nozzle and enter the detection area. A collimated diode laser beam passes through a series of beam-shaping optics and enters the detection area. The insets at the bottom left hand corner of the figure depict how the aerosol is interrogated. Inset 1 shows how the beam is split, and the time-of-flight of the aerosol is calculated by the scattered light signals gathered by the elliptical mirror and collected by the Avalanche Photodetector (Inset 2).

As the particle passes in front of the first beam, the laser light scattered by the aerosol is focused by an elliptical mirror onto a photodetector, which translates the light signal into an electrical pulse. When crossing the second beam, another electrical pulse is created in the same manner. The time-of-flight is then calculated by timing between the peaks of each electrical pulse. These velocities are then stored in 1024 “time-of-flight bins,”, with each bin assigned to a velocity value. Using this velocity data, the inertia of each particle is calculated, which directly correlates to its aerodynamic diameter. A larger particle will

have greater inertia, and thus a lower velocity in an accelerated flow than a smaller particle (TSI, 2009).

Figure 15: Aerodynamic Particle Sizer (APS)

The APS uses time-of-flight technology to measure the inertia of an aerosol as it is accelerated past a split laser beam. The aerosol scatters the laser light onto an elliptical mirror and an Avalanche Photodetector translates the scattered light signal into an electrical signal. The time-of-flight is used to calculate the aerodynamic diameter of a passing aerosol.

While the APS is effective in calculating the aerodynamic diameter of solid particles, which remain rigid as they are accelerated through the time-of-flight chamber, it is less accurate in calculating the diameters of liquid droplets. Baron (1986) conducted a study regarding this phenomenon and found that because a liquid particle deforms as it is accelerated, especially larger liquid particles with lower surface area to volume ratios, the APS will underestimate oil-based droplets by a significant factor (up to 20 percent for droplets with a 15 µm aerodynamic diameter). This tendency to underestimate large droplet diameter was also observed in this research (up to 14 percent at 8 µm, see

Appendix E for details). As such, the APS was not used in this research to verify the aerodynamic diameters produced by the VOAG, but instead was used qualitatively to assess the geometric standard deviation of the aerodynamic diameters within aerosol population and as a "quick check" for periodic quality assurance during testing.

3.2.3 Isokinetic Rake

In order to characterize properly the wind tunnel for concentration distribution, an isokinetic "rake" was constructed from schedule 40 PVC pipe. Due to vacuum pump restrictions, isokinetic velocities were achieved with 4 samplers instead of the prescribed 5 when running at the 8 km/hr setting. For the purposes of this research, however, 4 samplers were found to be adequate to characterize the cross section due mainly to the rake design. The center point of the rake was fitted with sampler cone 1. At the center, three arms were attached. Samplers 2, 3, and 4 were fitted at 7.47 cm, 14.94 cm, and 22.40 cm from the center point along their respective arms. The arms could then be rotated 360 degrees, creating three concentric sampling rings around the center sampler 1. Figures 16 and 17 demonstrate.

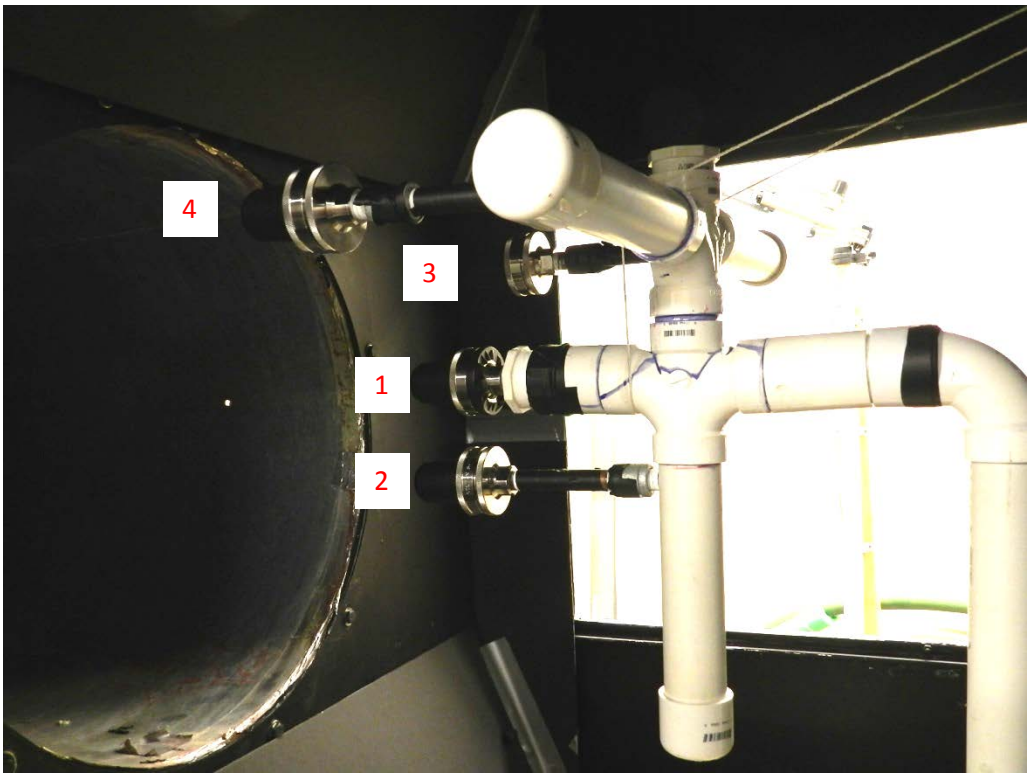

Figure 16: Isokinetic Rake (Side View)

Side view of the isokinetic rake. The manifold head rotates around Cone 1 (center).

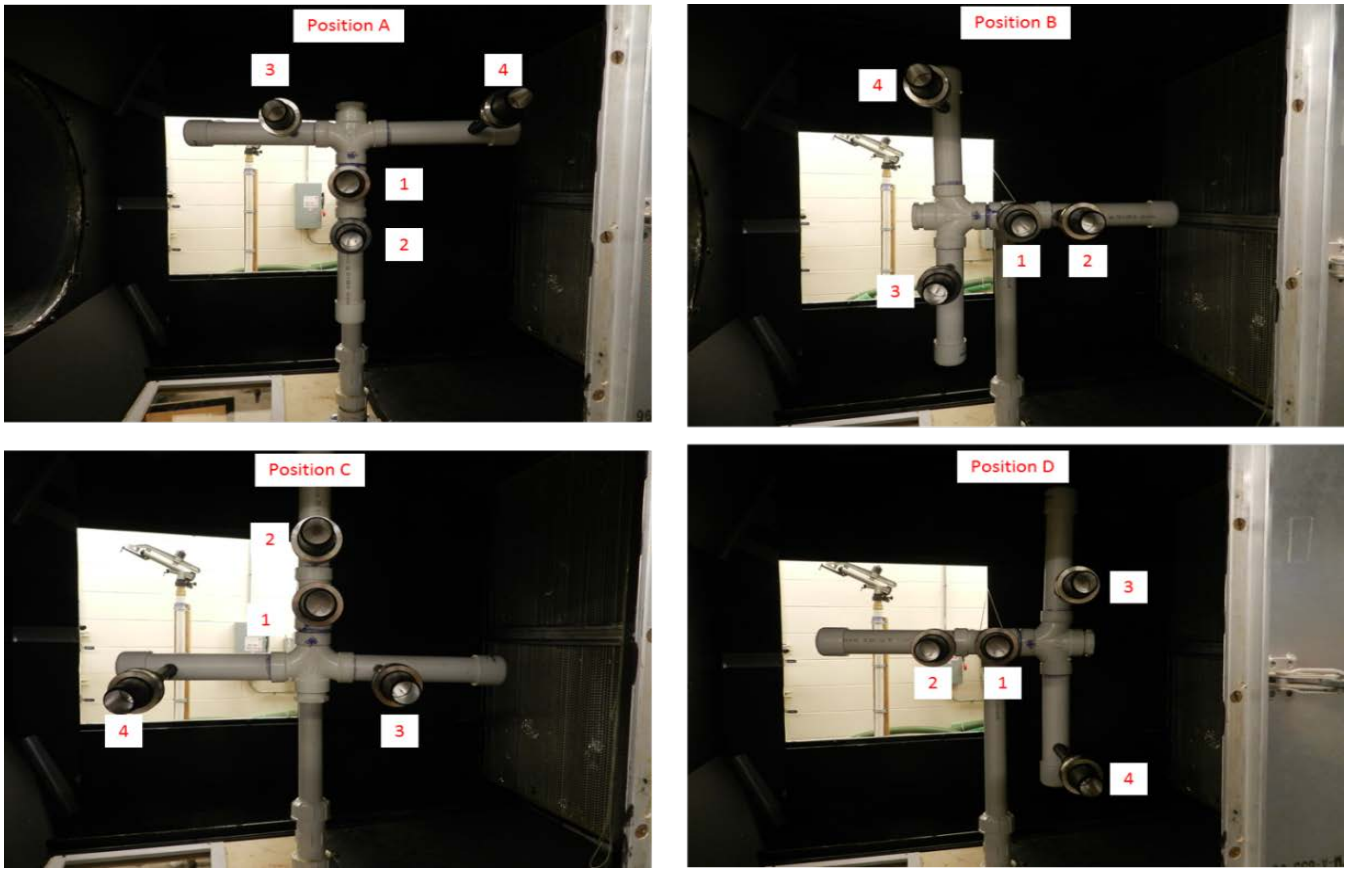

Figure 17: Isokinetic Rake Positions and Cone Numbers

The four sampling positions (A,B,C, and D) are demonstrated above. The manifold head rotates counter-clockwise around Cone 1, which remains in the center throughout testing.

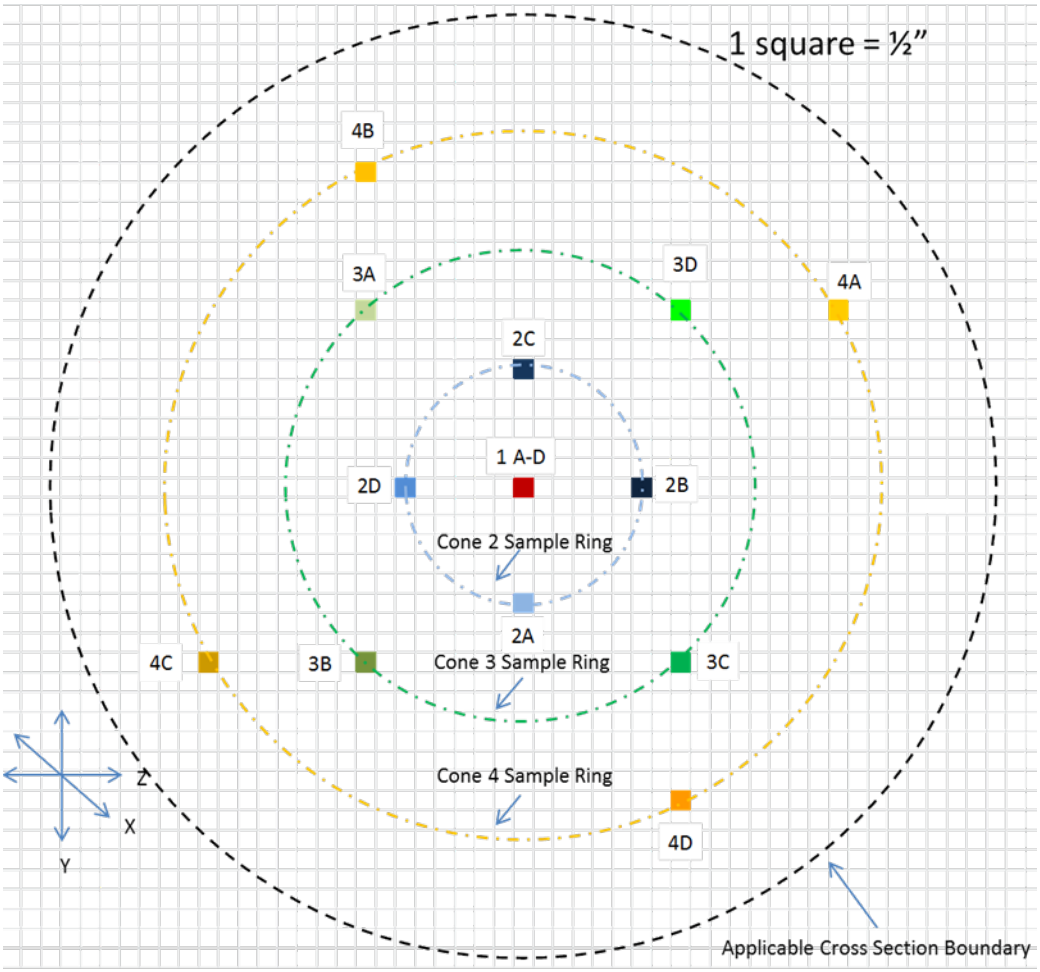

Figure 18: Isokinetic Sampling Diagram of Applicable Cross Section

The detail shows the sampling positions as the manifold head is rotated 90 degrees through positions A, B, C, and D. The applicable cross section boundary is represented by the black dashed line. The concentric “sampling rings” are represented by the dashed yellow ring (Cone 4); green ring (Cone 3), and blue ring (Cone 2). Cone 1 remains at the center position throughout testing.

Each isokinetic sampler was comprised of a stainless steel 47 mm in-line filter holder (Pall, Inc.) designed to hold 47 mm ProWeigh glass fiber filters (Environmental Express, Inc.). The front plate of the filter holder was removed and a machined aluminum cone with a knife edge was secured in its place.

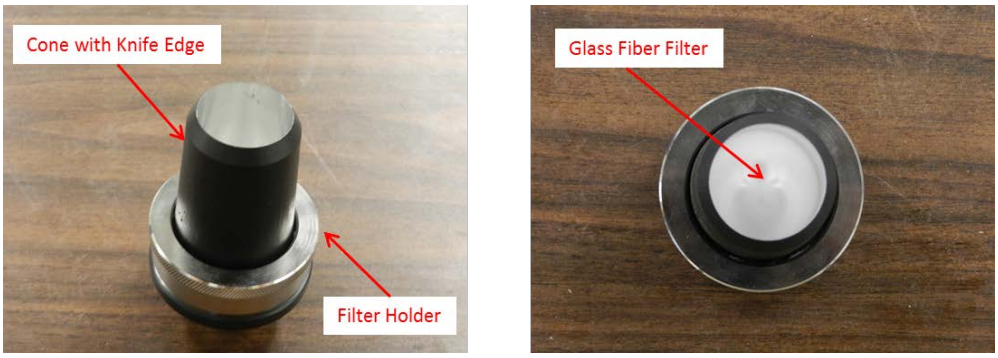

Figure 19: Isokinetic Sampler

Each isokinetic cone was machined from aluminum and honed with a knife edge to reduce boundary layer effects at the inlet. The cone was connected to a Pall 47 mm in-line filter holder, each holding a borosilicate glass fiber filter.

The samplers were connected to their respective arms, completing the rake. Isokinetic conditions were established using two Gast 0823 oil-less rotary vane vacuum pumps in parallel, each capable of achieving 13.59 m^3/hr flow rates of operating at vacuum pressures up to 897.29 millibars to draw the air through the rake. Dwyer air flow meters provided measurement of flow rate which could be adjusted with ball valves downstream of the meter. Setting the flow rate such that the velocity entering the cone was the same as the test section established the isokinetic condition. If the flow being pulled into the cone is slower than the approaching streamlines, the streamlines will be diverted around the cone inlet. Some of the particles entrained within these bending streamlines will have too much inertia to make the turn and will exit their normal flow and enter the cone, causing over-sampling. If the flow is too fast at the inlet, then the reverse is true. Streamlines being pulled into the cone will eject their entrained particles around the cone as they turn, causing a condition of under-sampling.

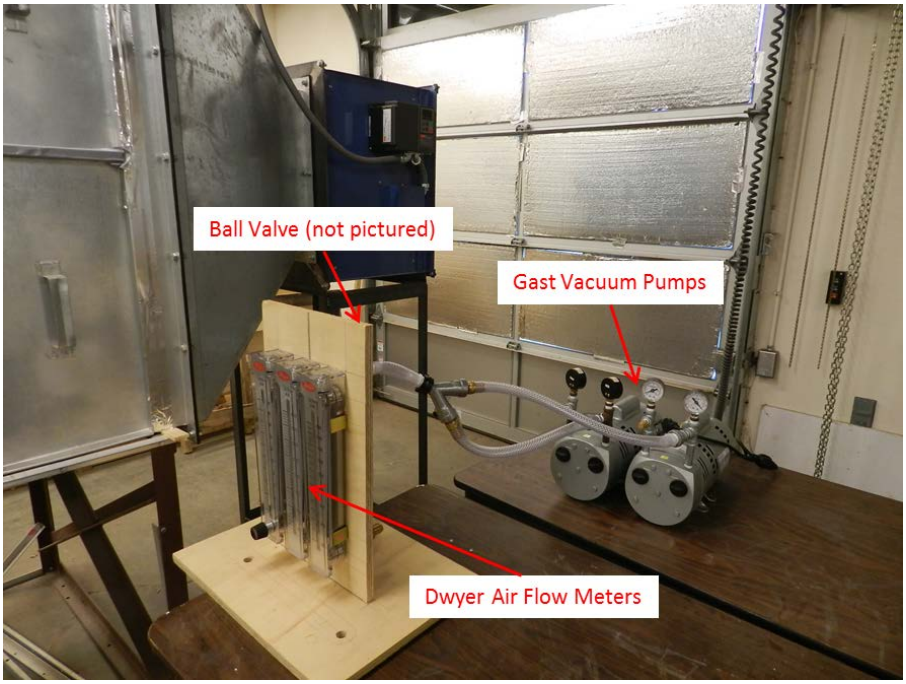

Figure 20: Isokinetic Flow Control Setup

Isokinetic conditions were established and maintained between the cones and the wind tunnel flow by employing two Gast rotary vane vacuum pumps to pull air through the isokinetic manifold. The flow through the pumps was controlled with a ball valve downstream of the Dwyer flow meters, which were used to set and monitor the appropriate flow rate.

To ensure that proper isokinetic conditions were established, the PIV Laser System was used to image the entrained particles and to calculate velocities around the cone inlets. Figures 21 through 23 are examples of sub-isokinetic, supra-isokinetic, and substantially isokinetic conditions, respectively, at a cone inlet.

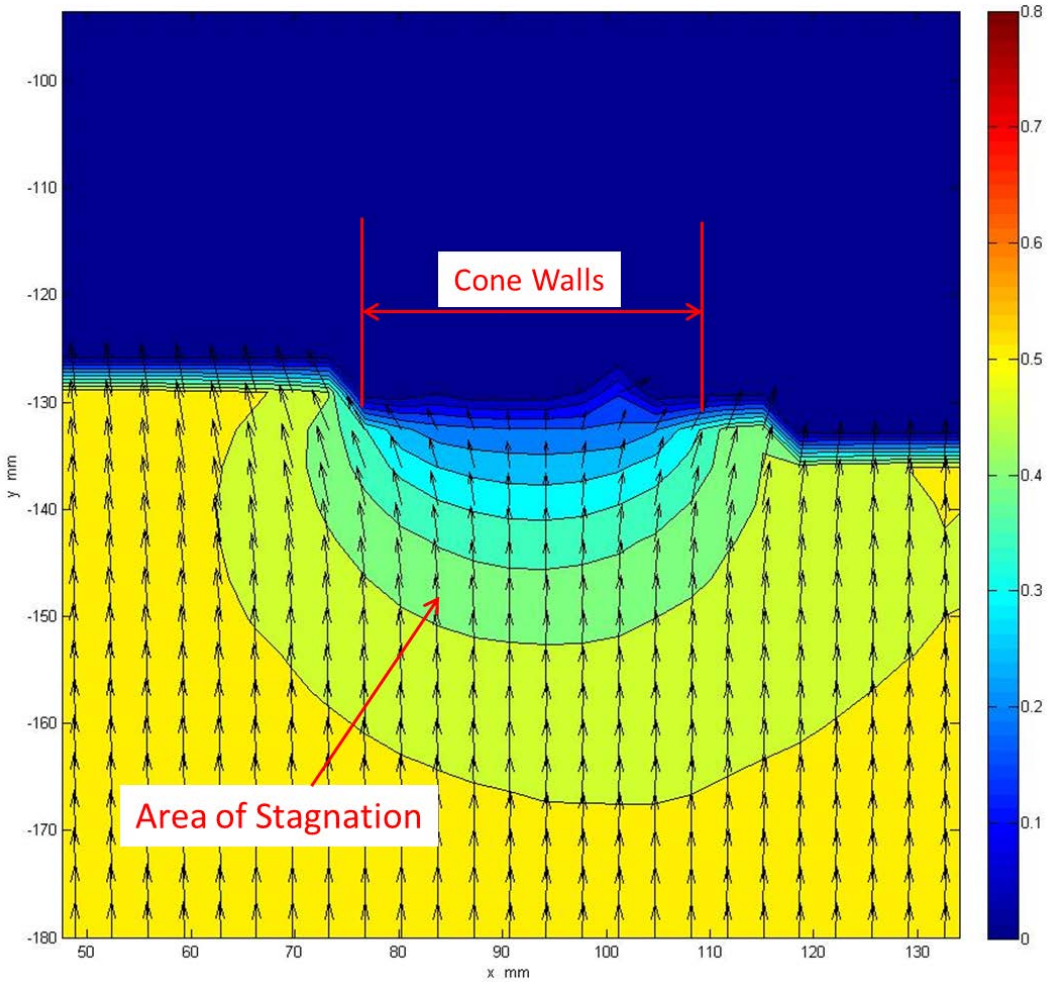

Figure 21: Example of Sub-Isokinetic Flow at a Cone Inlet

The colors in this image represent velocity ranges as described by the color bar on the right side of the figure, in m/s. The black arrows throughout the color floods represent the time average velocity vectors taken from 50 image pairs. The large area of stagnation in front of the cone, as shown by the tight velocity color gradient, is due to insufficient flow through the cone, and causes the streamlines to divert around the inlet. This condition will result in over-sampling, as the inertia of the droplets will cause them to leave the flow and enter the cone as the streamlines bend.

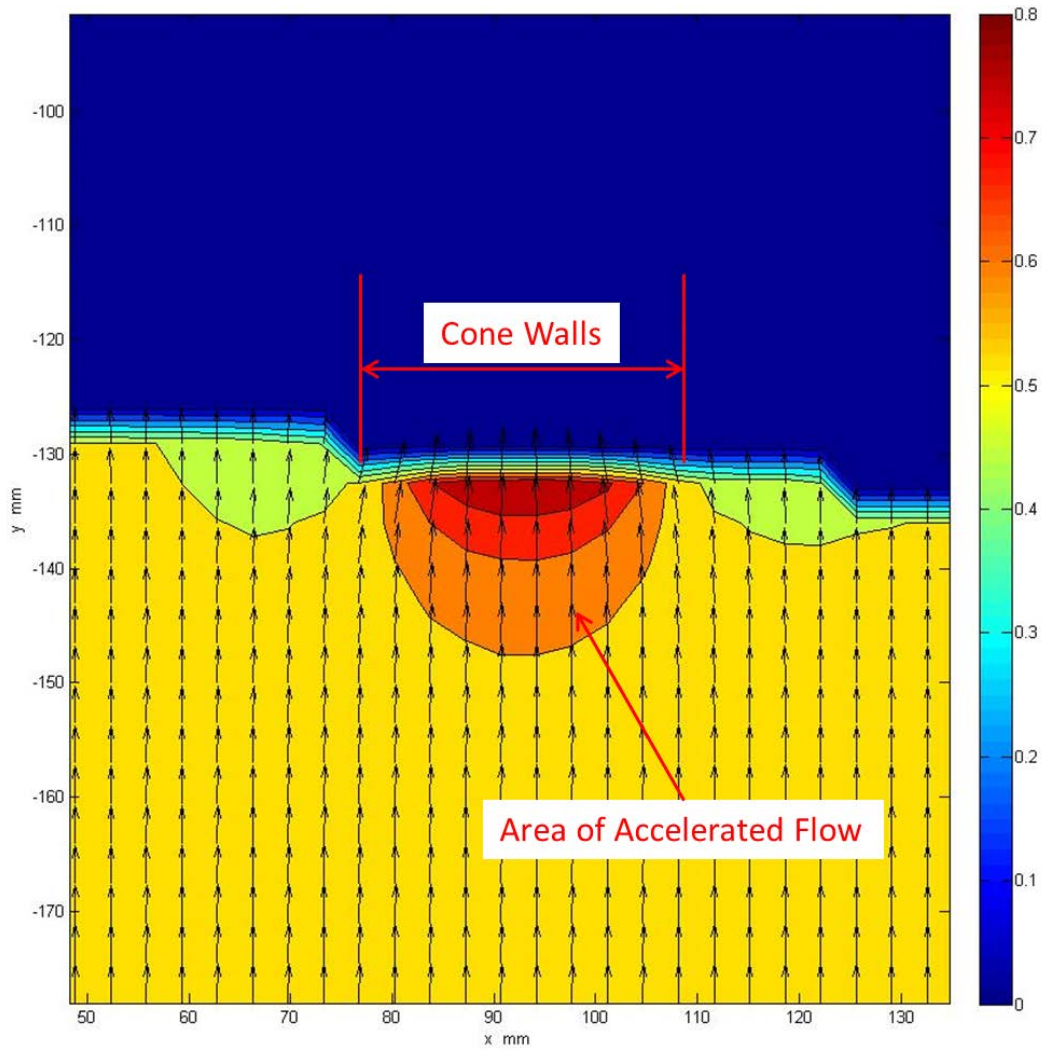

Figure 22: Example of Supra-Isokinetic Flow at a Cone Inlet

The colors in this image represent velocity ranges as described by the color bar on the right side of the figure, in m/s. The black arrows throughout the color floods represent the time average velocity vectors taken from 50 image pairs. The area of acceleration at the cone inlet, as shown by the tight velocity color gradient, is caused by excess air flow being drawn through the cone. This causes a condition of under-sampling, as the streamlines are diverted into the cone. The inertia of the droplets causes them to leave the flow and miss the inlet.

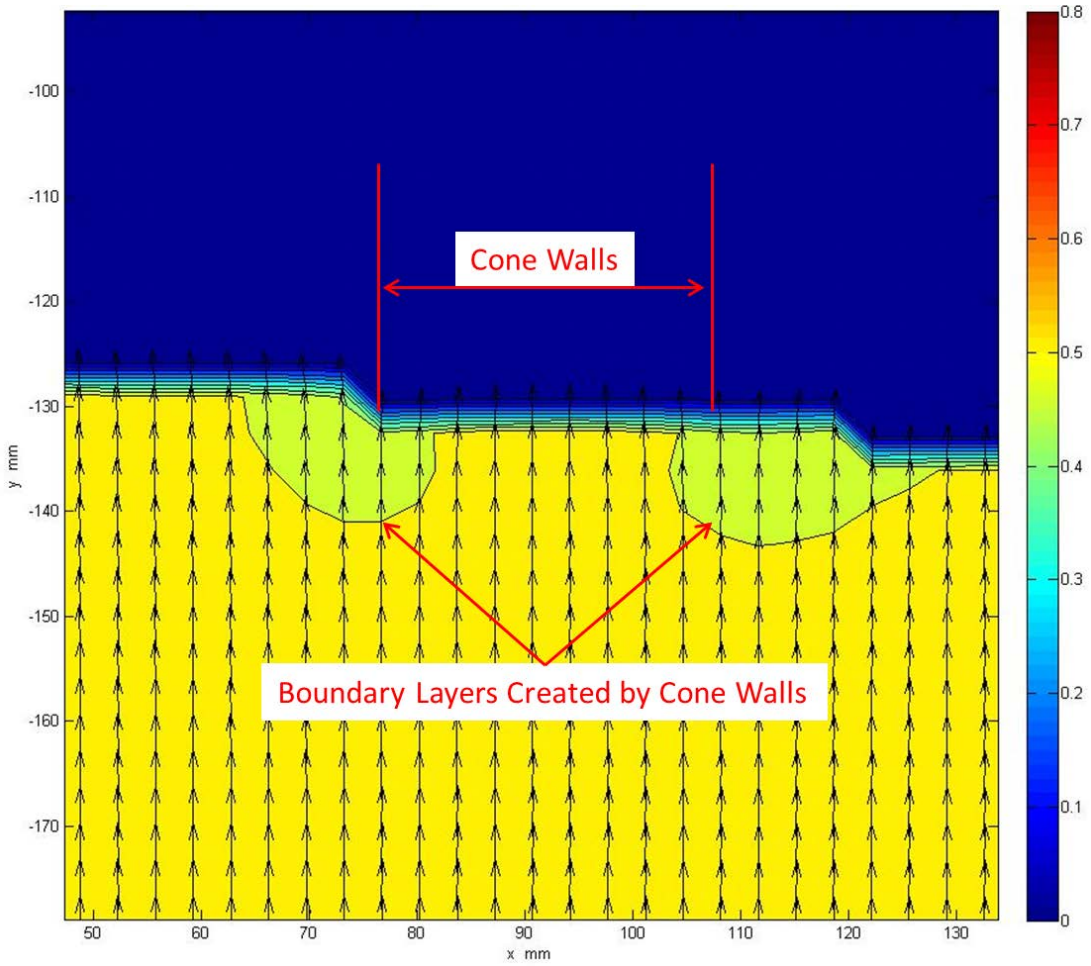

Figure 23: Example of Substantially Isokinetic Flow at a Cone Inlet

The colors in this image represent velocity ranges as described by the color bar on the right side of the figure, in m/s. The black arrows throughout the color floods represent the average velocity vectors taken from 50 image pairs. The areas shaded in green are regions of decreased velocity due to the boundary layers created by the cone walls, which are minimized by the cone's knife edges. The straight velocity vectors show the streamlines are entering the cone inlet with very little deviation, thus providing an aerosol concentration sample that is representative of the actual flow.

As can be seen in Figure 23, the entrance velocity at the cone inlet is nearly identical to that of the normal flow within the cross section, and the velocity vectors are straight, indicating approximately isokinetic flow.

3.2.4 Fluorometer

Figure 24: 10-AU Fluorometer

The calibrated fluorometer used in fluorometric analysis of solution concentrations is far more accurate and precise than a mass balance used in gravimetric analysis. The Turner Designs 10-AU Fluorometer, when analyzing concentrations of fluorecien in solutions, is capable of a 0.01 part per billion precision.

The Turner Designs 10-AU-005-CE Fluorometer measures the concentrations of fluorescent material (analytes) within a sample (Turner Designs 1997). Fluorescent material absorbs light, thus exciting the molecules, which then almost immediately emit new light at a longer wavelength. The fluorometer uses a light from an internal source passed through a color filter, which provides the proper initial excitation wavelength specific to the fluorescent material being analyzed, to excite the fluorescent material in the sample. The material then re-emits its absorbed energy in the form of a second wavelength. This emitted light is collected by a photomultiplier tube after it passes through a second filter to block out any scattered light or any other possible light emissions from fluorescent material that may be unintentionally present in the sample. The amount of light collected by the photomultiplier is proportional to the concentration

of fluorescent material within the sample, the value of which is displayed on the instrument screen (Turner Designs, 1997).

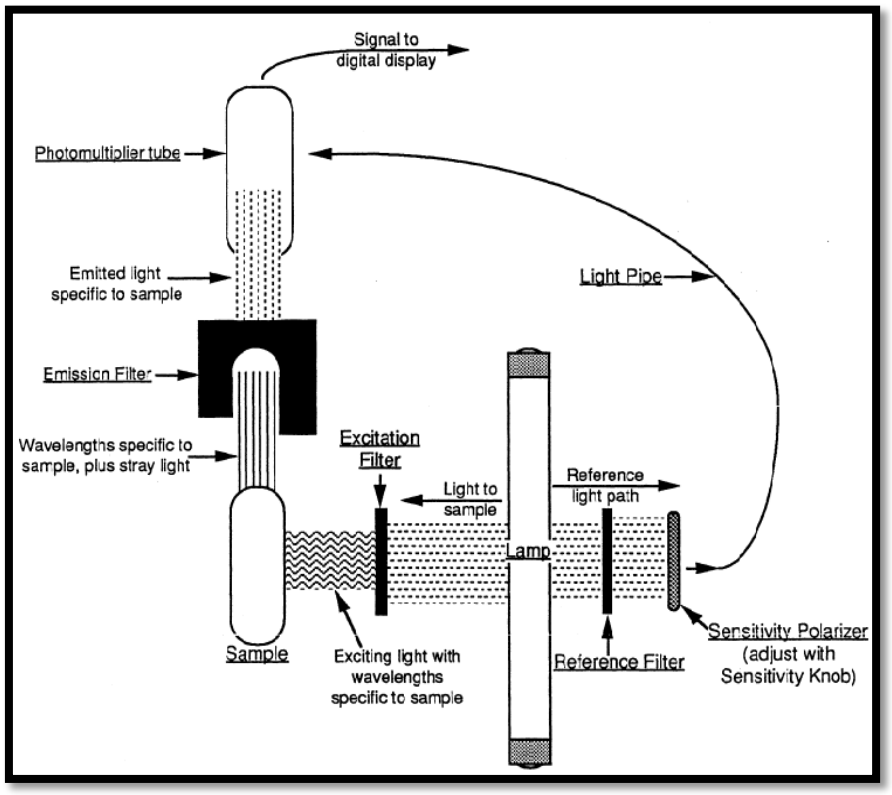

Figure 25: Optical System of the Model 10 AU Fluorometer (Turner Designs, 1997)

The lamp emits a light sample that is filtered by the excitation filter to a wavelength specific to the material under study (in this case, uranine). The fluorescent material absorbs the light and immediately re-emits light at a longer wavelength. This re-emitted light travels through the emission filter and is collected by the photomultiplier tube. The light from the lamp also travels through a reference filter to provide a reference light signal. This is used for continuous internal re-calibration and is also used to set the sensitivity of the instrument prior to testing.

The fluorometer used in this research is extremely sensitive, and when analyzing fluorecein (or uranine) in a solution has a precision of 0.01 parts per billion (ppb). In addition to being user-friendly, fluorometers are more accurate and precise than a mass

balance; consequently, extremely small concentrations can be measured with a high level of confidence.

The calibration of the instrument is fairly straightforward. A solution of 50/50 distilled water/isopropyl alcohol (including 4-6 drops of NaOH to stabilize the solution's pH) is used to "blank" the instrument. A standard solution of approximately 50 percent of the expected concentration range is then made up by the user and read by the instrument, providing the data for a calibration curve. If the calibration mode of the unit is set on manual, a third and fourth standard should be prepared to establish a concentration curve; however, this is not necessary when using the pre-set sensitivity settings (Turner Designs, 1997). For this study, the fluorometer was calibrated under the "medium" sensitivity range, as recommended by the manufacturer for samples with concentrations between 5 and 100 ppb and is reported as accurate to the nearest 0.01 ppb (Turner Designs, 1997).

3.2.5 Testing Procedures / Coefficient of Variation ($C_{v\%}$) Calculation

Table 4 below summarizes the sampling scheme used in this research. Five target aerosol sizes (3, 7, 10, 13 and 17 µm) were used to characterize the concentration profile of the cross section in four rake positions (A-D) over the two target wind speeds (2 km/hr and 8 km/hr), resulting in 160 total isokinetic samples.

		2km/hr																			
	Target Aerosol Size	3µm				7µm				10µm				13µm				17µm			
	Rake Position	A	B	C	D	A	B	C	D	A	B	C	D	A	B	C	D	A	B	C	D
Sampling Cone	1																				
	2																				
	3																				
	4																				
		8km/hr																			
	Target Aerosol Size	3µm				7µm				10µm				13µm				17µm			
	Rake Position	A	B	C	D	A	B	C	D	A	B	C	D	A	B	C	D	A	B	C	D
Sampling Cone	1																				
	2																				
	3																				
	4																				

Table 3: Sampling Scheme Summary

The sampling scheme of the concentration characterization tests is organized as shown. The cross section of the wind tunnel was analyzed for concentration distribution by introducing five monodisperse aerosol populations into the tunnel (3, 7, 10, 13 and 17 µm). For each specific size, the rake was rotated 90 degrees four times (positions A-D), totaling 80 samples. This procedure was performed at both 2 km/hr and 8 km/hr, resulting in 160 total samples.

The sampling cones are numbered 1 through 4, with 1 being the center (see Figure 18 for cone numbering example). For each new rake position, the manifold was rotated clockwise 90 degrees, with A at 0 degrees rotation; B at 90 degrees rotation; C at 180 degrees rotation; and D at 270 degrees rotation. The sample naming convention consisted of velocity, rake position, target particle size, and cone number (for example 2B7-3 for 2km/hr, position B, 7µm, cone number 3). For each run, clean glass fiber filters were placed in the filter holder / cone assemblies and screwed in place on the rake.

Using the principles discussed in Chapter 2 from Berglund and Liu (1973) and Faulkner and Haglund (2012), a solution of 5 percent uranine to oleic acid (by mass) was diluted by isopropyl alcohol at ratios specific to each desired aerosol diameter (see Table 3 for solution ratios). The isopropyl alcohol served as the volatile portion of the solution

and is evaporated from the VOAG jet by the dilution air source. The 5 percent uranine to oleic acid solution served as the non-volatile portion and therefore does not evaporate out of the jet, resulting in monodisperse oleic acid droplets tagged with a uranine fluorescent tracer. Prior to use in the VOAG, the prepared solutions were filtered three times through a borosilicate glass fiber filter to remove unwanted nonvolatile solids that may plug the 20 μm VOAG orifice, and were placed for no less than thirty minutes in a sonic bath to ensure a uniform solution mixture.

To introduce the aerosols into the wind tunnel, the VOAG was set up at the tunnel entrance. A pressurized, 3.8 liter can equipped with a regulator provided adequate liquid flow for extended continuous testing runs without interrupting the jet. This proved extremely important, as it was nearly impossible to reproduce perfectly identical droplets with the exact same population characteristics between one run and the next if the jet was stopped and re-started. As suggested by Dr. William B. Faulkner during a phone conversation, a Model 4003A BK Precision 4 Megahertz Function Generator generated the desired frequency (the VOAG is equipped with its own frequency generator; however, by using the external function generator a square wave instead of a sinusoidal wave could be employed, generated a more forgiving and homogenous aerosol population).

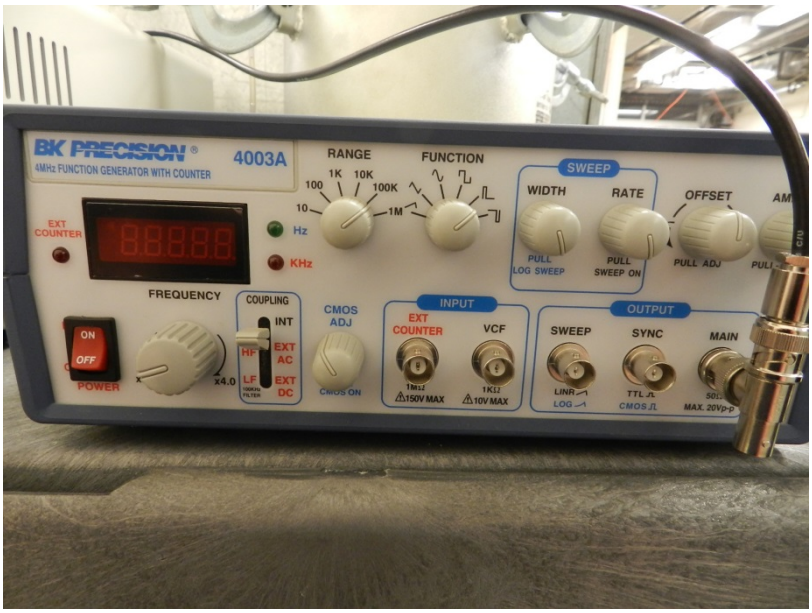

Figure 26: BK Precision 4003A External Function Generator

The external function generator was used in place of the internal function generator supplied with the VOAG unit. The external unit provided a square wave to the VOAG, resulting in a more uniform size population of aerosol aerodynamic diameters.

The Kr-85 (TSI, Inc.) radioactive neutralizer minimized the charge (from approximately 7300 charges per particle to 4) by ionizing the atmosphere within the tube into positive and negative ions. As a charged particle passed through the ionization tube, it collected ions of the opposite polarity (TSI, 2012b), thus minimizing the number of charged particles of opposite polarity joining together to form multiplets. From the neutralizer, the droplets passed through a delivery hose and into the APS sampling inlet. Small adjustments were made to the frequency, dilution and dispersion airflow, and solution delivery pressure from the pressurized can as the APS was used to size and calculate the population geometric standard deviation of aerosol mass in real time.

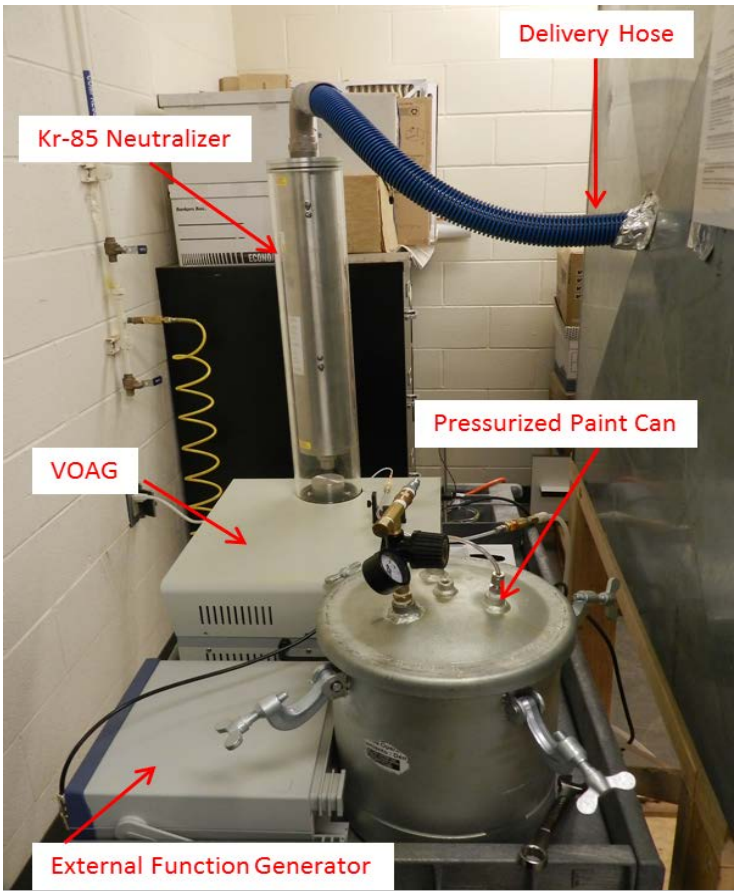

Figure 27: VOAG Experimental Setup

The aerosol generation and delivery system consisted of a pressurized can used to deliver a continuous flow of solution to the VOAG; the function generator to supply a square wave to the VOAG piezoelectric ceramic; the VOAG; the Kr-85 Neurtralizer to minimize the charge on the particles exiting the VOAG; and the delivery hose.

As discussed in section 3.2.2, the APS cannot be used to size the liquid aerosols accurately on its own. Therefore, prior to each run, a Buck BioSlide Bioaerosol Air Sampling Pump impactor (A.P. Buck, Inc.) was used to collect aerosols generated by the VOAG and impact them onto glass slides coated with Type L oleophobic surfactant. The slides were first cleaned using a 50/50 solution of isopropyl alcohol / distilled water (by volume) and left to dry. Once the slides were dry, 3-5 drops of surfactant were applied to

the center of one slide, which was immediately pushed against a second slide, ensuring relatively even distribution across the impaction surfaces of both slides. The treated slides were then left to dry a second time.

Figure 28: Buck BioSlide Impactor

The impactor was used to draw droplets produced by the VOAG from the air near the delivery hose and impact them at 15 liters per minute upon a glass slide treated with NyeBar Type L oleophobic surfactant. Impactor pictured here with the included calibration rotameter.

The impactor was calibrated to 15 liters per minute (LPM) flow rate using a rotameter that was supplied with the unit (maximum flowrate for the unit was 20 LPM). This procedure was repeated once per day prior to aerosol collection. A dry, pretreated glass slide was then put into the chamber of the impactor and the unit was turned on. Once the motor reached full operational speed, the impactor sampled the air at the outlet of the VOAG neutralizer tube for 0.5 to 10 seconds. The variation in time was a function of the aerosol size being captured, as too long of exposure at the larger sizes resulted in over-collection and a falsely high percentage of observed multiplets (caused by droplets impacting on top of another). The newly exposed slide was examined using the

EQRTL's Nikon Eclipse ME600 microscope equipped with a PixeLink Megapixel Firewire Camera linked to a computer with Omnimet Digital Imaging System software. The viewing image was displayed in real time on the computer screen using the software, where the spheroids were brought into focus using the 20x microscope objective. Once in focus, an image was captured, and the next interrogation region was imaged (each slide was analyzed at minimum of five different points along the impaction area, A through E, see Figure 29).

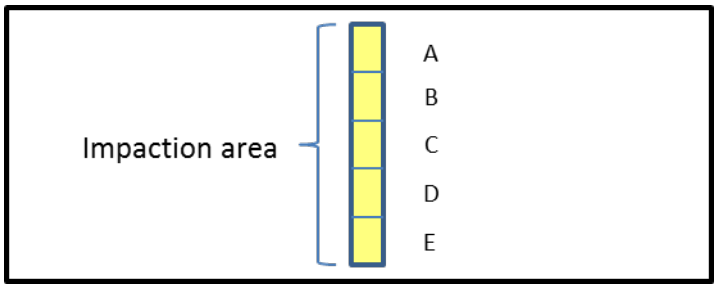

Figure 29: Microscope Impaction Area and Interrogation Regions

The impaction area of each slide was divided into five interrogation regions to ensure a representative sample of the population. Each region was imaged and analyzed for droplet diameter of singlets and presence of multiplets.

The diameters of the spheroids were measured using the software's click-and-drag sizing function (see Figure 30 for example), which converted a pixel count along the line into length in micrometers. The objective was calibrated using an Edmunds Optics stage micrometer calibration slide to create a pixel/µm calibration factor. The original diameters of the spheroids were calculated using the NyeBar Type L flattening coefficient of 1.297, as reported by Faulkner and Haglund (2012). In addition to measuring the diameter, a count of multiplets was performed in each image to determine their percentage of the whole. Figure 30 shows the presence of a doublet within the

viewing range measuring 20.91 pixel diameter. The precision of the click-and-drag function was ± 1 pixel (1 pixel = 0.53 µm, as defined by the calibration of the 20x objective using the stage micrometer calibration slide), which led to low accuracy of measurement for the smaller diameters, as demonstrated in Table 5 below. Therefore the geometric mean of no fewer than 50 measurements was calculated to determine a representative diameter of singlets for each population size.

aerodynamic diameter (µm)	precision (± 1 pixel)	accuracy (%)
3	± 0.53 µm	± 17.67
7	± 0.53 µm	± 7.57
10	± 0.53 µm	± 5.30
13	± 0.53 µm	± 4.08
17	± 0.53 µm	± 3.12

Table 4: Precision and Accuracy of Click-and-Drag Function by Aerodynamic Diameter (µm)

The precision of the Omnimet click-and-drag measurement function is ± 1 pixel. After calibrating the 20x objective of the microscope using the Edmunds Optics stage micrometer calibration slide, this precision equates to ± 0.53 µm. This led to low accuracies (>5 percent) for the 3, 7, and 10 µm population measurements.

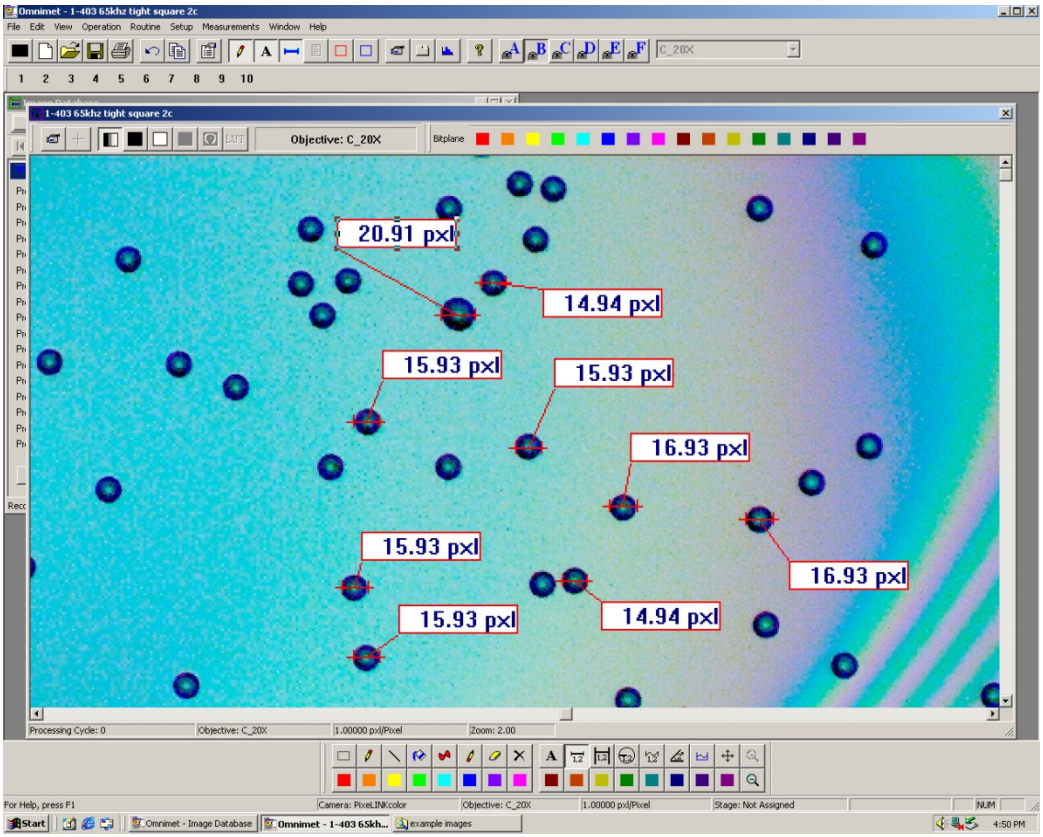

Figure 30: Microscopy Analysis Example

The impacted spheroids were measured in pixel length across the diameters using the click-and-drag sizing function of the Omnimet software. The pixel lengths were converted to length in µm via a calibration factor. The precision of the sizing function is ± 1 pixel, as demonstrated by the sizes of the singlet droplets varying between 14.94 pixels and 16.93 pixels (the decimal out to the one hundredths place is misleading, as it is a result of the calibration factor). To account for this variation in measurement, the geometric mean of no less than 50 singlets was used as the actual measured value for each interrogation region. In addition, the number of multiplets was counted to ensure no population had more than 10 percent. A single multiplet (20.91 pixels) is visible in the image above.

Table 5 summarizes the solution ratios, VOAG settings, and function generator settings used for this research, as well as the geometric standard deviations of aerosol aerodynamic diameters (as calculated by mass) for each test population. Each setting was adjusted as the APS analyzed the geometric standard deviation of the droplet diameters within the population in real time. At the smaller sizes (3, 7, and 10 µm), the geometric

standard deviations were lowest when operating with a liquid flow rate of 0.002825 cm^3/ s and an operating frequency of 75 to 80 kHz. By contrast, the geometric standard deviations for the aerosol populations with larger diameters (13 and 17 µm) were much too high at these flow rates and frequencies (up to 1.3 for the 17 µm tests). When the flow rate was dropped to 0.002317 cm^3/ s and the frequency to 47 and 45 kHz, the geometric standard deviations dropped back into an acceptable range.

	3µm	7µm	10µm	13µm	17µm
VOAG solution concentration (ml oleic acid/ml isopropyl alcohol)	1:2449	1:199	1:60	1:50	1:23
Function Generator Frequency (kHz)	75	75	80	47	45
Calculated size by frequency and solution ratio (µm)	3.14	7.19	10.45	12.48	16.4
Geometric mean of singlet diameters as measured by the microscope (µm)	n/a*	7.10	10.55	12.58	16.64
Solution flow rate through the VOAG (cm^3/s)	0.002825	0.002825	0.002825	0.002317	0.002317
Average APS Geometric Standard Deviation	1.06	1.09	1.12†	1.12†	1.10

Table 5: Experimental Aerosol Information

The VOAG solution concentrations and function generator settings (± 0.0005 kHz) were set as shown, and the calculated size is based on the equations derived by Berglund and Liu (1973). The geometric mean of singlet diameters as measured by the microscope values are the results of the microscopy inspection (± 0.53 µm). The solution flow rate of each test was calculated using the liquid pressure of the solution at the orifice. Finally, geometric standard deviations of aerosol aerodynamic diameters for each sample population are listed, as measured by mass with the APS.
** Low inertia of the 3µm droplets caused singlets to miss the impactor slide, therefore microscopy verification of the aerosol population was not possible given the equipment used.*
† The geometric standard deviation of these two populations would not fall below 1.1 as measured by the APS during testing; however, microscope analysis showed the population was in fact sufficiently monodisperse (less than 10 percent multiplets) and all singlets fell within ± 1 pixel of the geometric mean.

The goal of this research was not to match perfectly the target aerosol size with the VOAG output and quantify the accuracy and precision of doing so, but to generate sufficiently monodisperse aerosols with aerodynamic diameters that can be reliably verified as within ± 0.5 µm of the target sizes for wind tunnel characterization. The precision of the microscopy analysis used here (± 0.53 µm) is not sufficient to achieve this goal alone. Therefore a combination of the following was used for droplet size verification:

1. The theoretical aerosol diameter calculation as described by Berglund and Liu (1973)

2. The microscopy sizing analysis

3. The derived performance curve between the average APS aerodynamic diameter calculations and the microscopy sizing analysis. (See Appendix E for more detail).

Once the droplet geometric standard deviation was equal or less than below 1.1 and/or the population could be determined via microscopy to be within limits set by the regulation, the vacuum hose was removed and a second hose leading into the inlet filter box of the tunnel was placed over the neutralizer nozzle, directing the aerosols into the tunnel upwind of the turbulator. The fan was switched on, and the variable speed drive was set to produce the desired wind speed (13 Hz = 2 km/hr, 32 Hz = 8 km/hr). At the same time, the vacuum pumps drew air through the isokinetic rake, and the volumetric flow rates were controlled with the ball valve as a throttle and the manometers to monitor flow. The volumetric flow rates set for 2 km/hr and 8 km/hr to achieve isokinetic conditions were 190 cubic feet per hour (CFH) (5.38 m^3/hr) and 800 CFH (22.68 m^3/hr), respectively. At this point the timer was started with the run time determined by targeting a final mass concentration of uranine within a sample that fell between 20 ppb and 80 ppb (middle of the fluorometer calibrated range), assuming that 50 percent of the test aerosol made it through the tunnel and into the test chamber (0.5 efficiency coefficient). These middle ranges were targeted to account for the as-of-then unknown wind tunnel efficiency coefficient, which was calculated for each aerosol size after the testing was complete, and is discussed in Chapter 4. Table 7 summarizes the variables

used to calculate the expected fluorometer results assuming a 0.5 efficiency coefficient for the wind tunnel.

	3µm	7µm	10µm	13µm	17µm
Run Time (minutes)	360	60	60	30	30
Function Generator Frequency (kHz)	75	75	80	47	45
Target Mass (mg)	0.023	0.099	0.326	0.170	0.384
Amount of Aliquot Solution Used (ml)	50	50	125	80	150
Actual Size as Measured by the Microscope (µm)	n/a*	7.1	10.55	12.58	16.64
Calculated Fluorometer Reading Assuming 50% Efficiency (ppb)	26.54	49.8	69.7	54.25	64.11

Table 6: Summary of Run Variables and Expected Fluorometer Results

The run times for each test were calculated by targeting a mass to be collected upon the filters, with the VOAG operating at the listed frequency, assuming a 0.5 efficiency coefficient. The targeted mass and amount of aliquot solution used for dilution was determined by calculating the concentration of uranine tracer in the final sample necessary to fall within the calibration range of the fluorometer.
** The 3µm size could not be inspected by microscopy, so the target value of 3.0 µm was used for calculations.*

Upon completion of the run, all the equipment was shut off except the VOAG, which was kept running during testing to avoid restarting the jet, and the isokinetic cones were removed from the rake. To extract the oleic acid and uranine from the borosilicate glass fiber filters at the end of each run, we:

1. Removed the filters from the cone filter holder with a pair of tweezers and placed into a clean canning jar, pre-rinsed with the 50/50 isopropyl alcohol / distilled water aliquot.
2. Rinsed the inside of the cones with the aliquot from a squirt bottle to collect any aerosols that may have been clinging to the inside wall of the cone; collected rinse water in a 200 milliliter (ml) beaker and transferred to a clean and rinsed 50 ml

graduated cylinder; and rinsed the beaker with aliquot to recover any fluorescent material, again transferring the liquid to the graduated cylinder.

3. Added clean aliquot to the cylinder until the desired amount of solution was obtained, and then poured the volume into the canning jar where the corresponding filter was contained.
4. Added 4-6 drops of 1 molar NaOH to the jar to stabilize the pH of the solution; secured the lid.
5. Left the solutions to sit for at least 24 hours, allowing the uranine and aerosol solution to be extracted from the filter and dispersed throughout the solution.
6. Marked the jar using the naming convention discussed above.
7. Triple rinsed the beaker and graduated cylinder and repeated the above procedure for each sample.

Once the settling time had elapsed, each sample was analyzed by the calibrated fluorometer by pouring part of the solution into the cuvette and placing the sample in the test chamber. From these ppb values, the mass of uranine deposited upon each filter was calculated, and the following equation was used to calculate the isokinetic concentrations (C_{iso}) as directed by 40 CFR 53.43(2)(vii) (USEPA 1987):

$$C_{iso} = \frac{mass\ of\ material\ collected\ by\ the\ isokinietic\ sampler}{sample\ flow\ rate * sampling\ time}$$

The coefficient of variation $C_{v\%}$ for each run (for example, run 2A7, which is 7 µm droplets with the wind tunnel set to 2 km/hr and the rake in the A position) was calculated using the equation

$$C_{v\%} = \left(\frac{s_u}{\bar{u}}\right) * 100$$

where s_u = standard deviation and ū = sample mean.

Using the procedures discussed in this chapter, the $C_{v\%}$ values of both the velocity and concentration distribution were analyzed and characterized. The TSI PIV system successfully mapped the velocity flow fields across the applicable cross section through the five designated chord lines (A-D), which were used to determine velocity distribution within the wind tunnel test section. Isokinetic sampling cones, in conjunction with the VOAG and fluorometer, characterized the concentration profile at 13 discrete points within the applicable test section. Chapter 4 presents the results of these tests. The velocity flow fields across all chord lines have been effectively "stitched" together to give both a numerical and visual characterization of the flow through the test section at the two tunnel test speeds. In addition, the aerosol concentration profile has been quantified at the five droplet size tests for both the 2 and 8 km/hr test speeds, yielding a total of 40 $C_{v\%}$ calculations.

CHAPTER 4

RESULTS

Per 40 CFR 53 subparts D and F (EPA, 1987 and 1997), in order for an air dispersion wind tunnel to be used as an official test station for FRM air quality sensors, no discrete velocity measurement within the applicable cross section can exceed 10 percent of the mean velocity, nor can the overall $C_{v\%}$ value of concentration measurements throughout the cross section exceed 10 percent. Chapter 3 described the procedures used in this research to quantify the velocity and aerosol concentration profiles of the EQRTL Aerosol Dispersion Wind Tunnel. This chapter presents the results of those tests.

4.1 Results of Velocity Profile Characterization

Each chord subsection was imaged 120 times over 2 minutes with the PIV system, creating 60 image pairs and 60 instantaneous velocity vector files. Using the Tecplot software, the individual instantaneous velocity vector files were averaged, creating a single time-averaged velocity vector file and corresponding velocity field image for each subsection. 50 discrete velocity vector data points were extracted across the Z axis (X=0). These data included the horizontal (X) and vertical (Z) image-specific coordinates of each extracted point, as well as *u* component (velocity in the X direction), *v* component (velocity in the Z direction), and magnitude (velocity in both directions, or $\sqrt{u^2 + v^2}$) of the velocity vector. Using Microsoft Excel, these image-specific

coordinates and vector components were converted to an overall Cartesian coordinate system describing the applicable cross section of the wind tunnel. Table 8 demonstrates this conversion.

C1		
image z (mm)	tunnel z (mm)	velocity u (m/s)
212.73	-253.51	0.01
208.60	-249.38	0.07
204.48	-245.26	0.35
200.35	-241.13	0.55
196.22	-237.00	0.56
192.10	-232.87	0.57
187.97	-228.75	0.57
183.84	-224.62	0.57
179.72	-220.49	0.58
175.59	-216.37	0.58
171.46	-212.24	0.58
167.34	-208.11	0.58

Table 7: Example Coordinate Conversion from Image-Specific to Tunnel-Specific

For chord subsection C1, the extracted velocity vector data was put into a Microsoft Excel file, organized by the image-specific Z coordinate (in mm) and the u component (direction of flow, in m/s) of the extracted velocity vectors. A third column was created to convert the image-specific Z coordinates to the overall tunnel Z coordinates. The red fields indicate data points outside the defined cross section (within 228.6 mm of the origin for Chord C) and were omitted from analysis.

After the coordinates for the individual chord subsections were converted, they were stitched together to describe the velocities along the Z-axis over all subsections of a chord line. Tables 9 and 10 demonstrate this procedure.

C4		
image z (mm)	tunnel z (mm)	u velocity (m/s)
72.42	-36.99	0.64
68.29	-32.87	0.65
64.16	-28.74	0.65
60.04	-24.61	0.65
55.91	-20.49	0.65
51.78	-16.36	0.65
47.66	-12.23	0.65
43.53	-8.11	0.65
39.40	-3.98	0.65
35.27	0.15	0.65
31.15	4.27	0.64
27.02	8.40	0.64
22.89	12.53	0.64
18.77	16.66	0.64
14.64	20.78	0.64
10.51	24.91	0.64

C3		
image z (mm)	tunnel z (mm)	u velocity (m/s)
212.73	-24.91	0.64
208.60	-20.78	0.64
204.48	-16.66	0.64
200.35	-12.53	0.64
196.22	-8.40	0.64
192.10	-4.27	0.64
187.97	-0.15	0.64
183.84	3.98	0.64
179.72	8.11	0.64
175.59	12.23	0.64
171.46	16.36	0.65
167.34	20.49	0.65
163.21	24.61	0.65
159.08	28.74	0.65
154.96	32.87	0.65
150.83	36.99	0.65
146.70	41.12	0.65
142.57	45.25	0.65

Table 8: Example of Stitching Procedure for Subsections E1 and E2

Excerpts from subsections C4 and C3 are shown here. The data tables were placed side-by-side, positioned so that the tunnel-specific Z coordinates (middle column on both charts) were sequential. The fields highlighted in yellow represent overlapping data and were omitted from analysis.

Chord C	
tunnel z (mm)	u velocity (m/s)
-36.99	0.64
-32.87	0.65
-28.74	0.65
-24.61	0.65
-20.49	0.65
-16.36	0.65
-12.23	0.65
-8.11	0.65
-3.98	0.65
3.98	0.64
8.11	0.64
12.23	0.64
16.36	0.65
20.49	0.65
24.61	0.65
28.74	0.65
32.87	0.65
36.99	0.65
41.12	0.65
45.25	0.65

Table 9: Results of Stitching Subsections C3 and C4

The tunnel-specific coordinates and corresponding u velocity values of C3 and C4 are combined into one continuous data set that describes the flow about the origin of the cross section.

Figures 31-35 show the mapped average velocity flow fields for each chord line at the 2 km/hr target wind velocity (15 Hz VFD setting), and figures 36 - 40 show the same for the 8 km/hr target wind velocity (30 Hz VFD setting). The 15 and 30 Hz VFD setting designation is used instead of the target velocity in the figures below to emphasize that the flow rate (thus wind velocity) was controlled by manipulating the frequency setting of the FSD 26 fan. These VFD settings were chosen by employing a rough wind velocity to VFD frequency calibration curve to target velocities near the test speeds specified in 40 CFR 53 (USEPA, 1987 and 1997). The color-contoured velocity flow field images in each figure were made using the MATLAB (Mathworks, Inc.) program. Each velocity flow field image (with the exception of Figures 30 and 35, both representing Chord A) are comprised of individual subsection images also stitched together to represent the flow

of the chord line. The perspective of each two-dimensional plane is that of the X and Z directions (see Figure 1 in Chapter 3 for interrogation chord positions and 3-dimensional perspective). Below each field is a scatter plot of the individual extracted velocity values across the midpoint of the chord in the Z direction. The only values in Chords A and E that fall into the defined cross section are at the origin (denoted in their respective figures with a green circle), however for demonstration, an inch on either side of the origin was included in the figures.

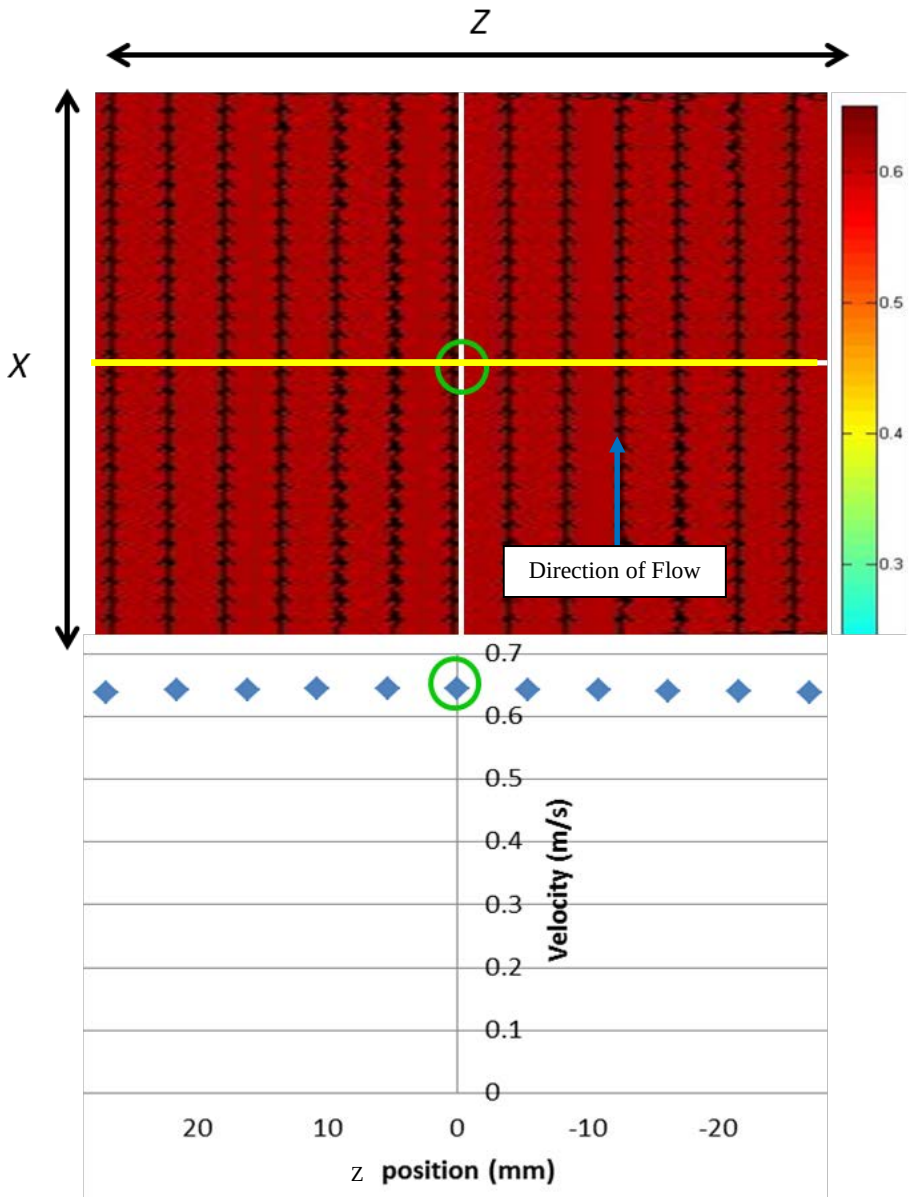

Figure 31: Velocity Profile of Chord A (15 Hz VFD Setting)

The background color in the velocity field image represents the flow velocity (m/s), as described by the color bar on the right side of the figure. The direction of flow is in the positive X direction, as denoted by the blue arrow. The green circle around the origin at the center of the velocity field represents the single point used for analysis, as this is the only point that fell within the circular applicable cross section (see Figure 1 in Chapter 3 for applicable cross section diagram). Discrete velocity data extracted along the Z axis (at X=0, denoted by the yellow line) are represented in the scatter plot below the velocity field image. The single velocity point used is also circled in green in the plot.

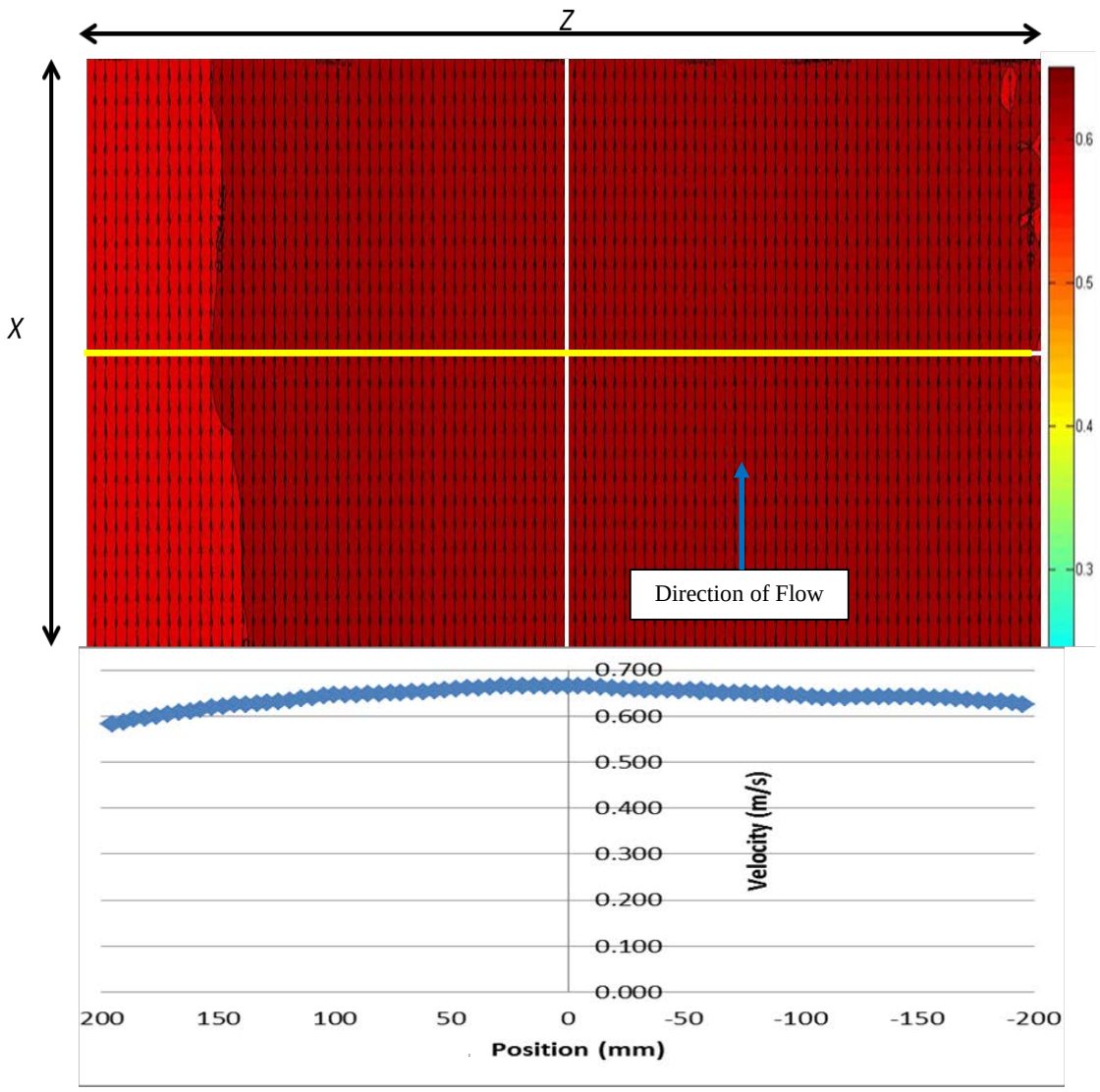

Figure 32: Velocity Profile of Chord B (15 Hz VFD Setting)

The background colors in the velocity field image represent the flow velocity (m/s), as described by the color bar on the right side of the figure. The direction of flow is in the positive X direction, as denoted by the blue arrow. Discrete velocity data extracted along the Z axis (at X=0, denoted by the yellow line) are represented in the scatter plot below the velocity field image. The apparent asymmetry of the color flood indicates that either the camera was not exactly centered when establishing the center of the chord line or that there is a slight imbalance of velocity flow at the edges of the applicable cross section.

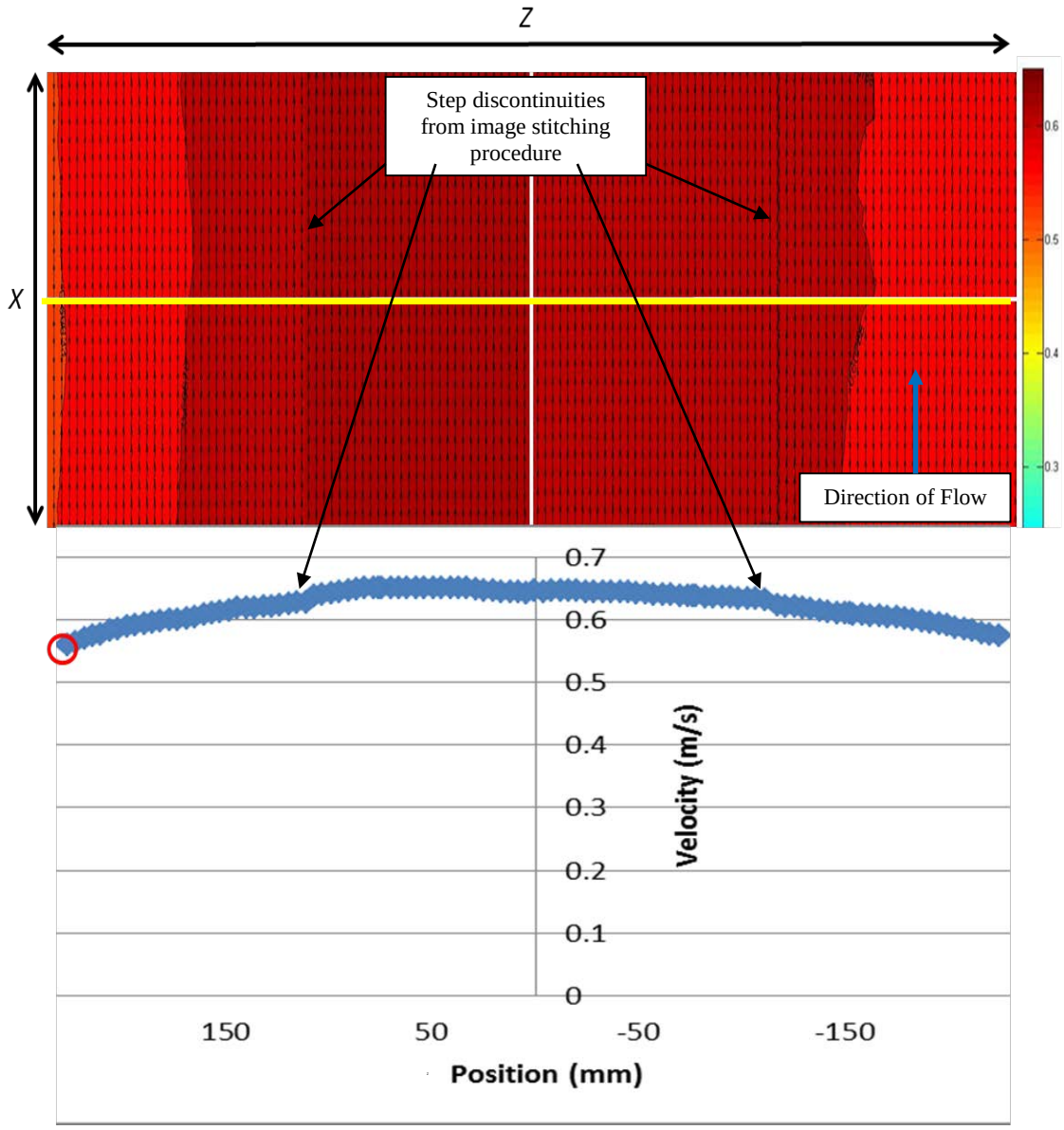

Figure 33: Velocity Profile of Chord C (15 Hz VFD Setting)

The background color in the velocity field image represents the flow velocity (m/s), as described by the color bar on the right side of the figure. The direction of flow is in the positive X direction, as denoted by the blue arrow. Discrete velocity data extracted along the Z axis (at X=0, denoted by the yellow line) are represented in the scatter plot below the velocity field image. The step discontinuities in the velocity field are the results of imperfect stitching between subsections. The red circle represents the single data point that fell outside the ±10 percent of the overall mean velocity requirement.

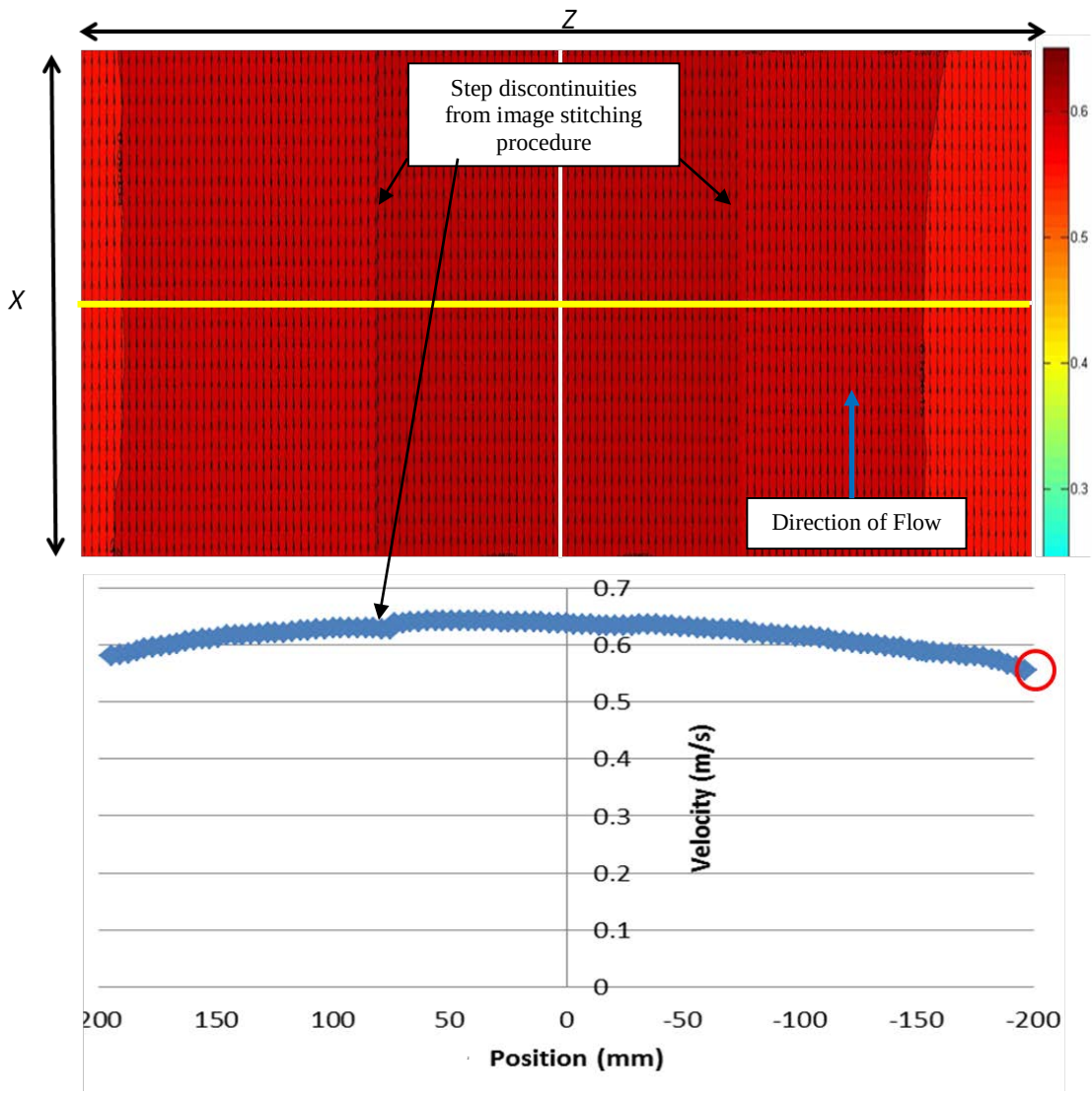

Figure 34: Velocity Profile of Chord D (15 Hz VFD Setting)

The background color in the velocity field image represents the flow velocity (m/s), as described by the color bar on the right side of the figure. The direction of flow is in the positive X direction, as denoted by the blue arrow. Discrete velocity data extracted along the Z axis (at X=0, denoted by the yellow line) are represented in the scatter plot below the velocity field image. The step discontinuities in the velocity field are the results of imperfect stitching between subsections. The red circle represents the two data points that fell outside the ±10 percent of the overall mean velocity requirement.

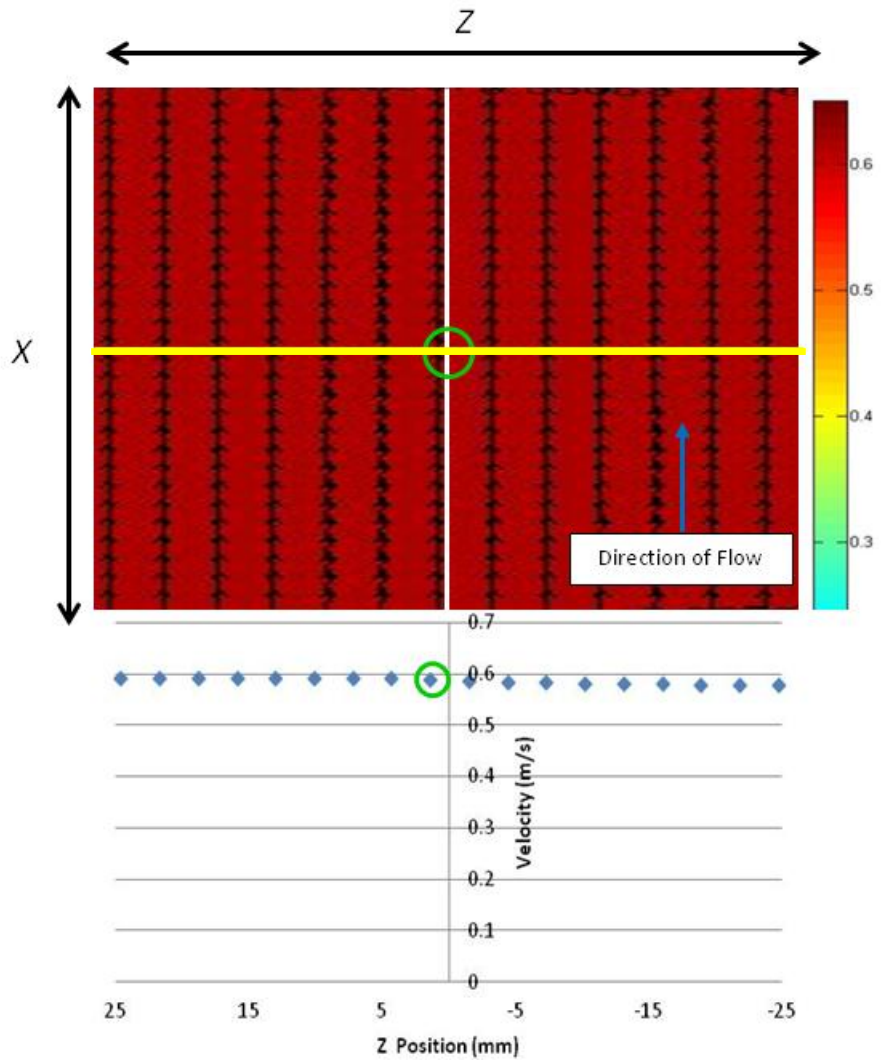

Figure 35: Velocity Profile of Chord E (15 Hz VFD Setting)

The background color in the velocity field image represents the flow velocity (m/s), as described by the color bar on the right side of the figure. The direction of flow is in the positive X direction, as denoted by the blue arrow. The green circle around the origin at the center of the velocity field represents the single point used for analysis, as this is the only point that fell within the circular applicable cross section (see Figure 1 in Chapter 3 for applicable cross section diagram). Discrete velocity data extracted along the Z axis (at X=0, denoted by the yellow line) are represented in the scatter plot below the velocity field image. The single velocity point used is also circled in green in the plot.

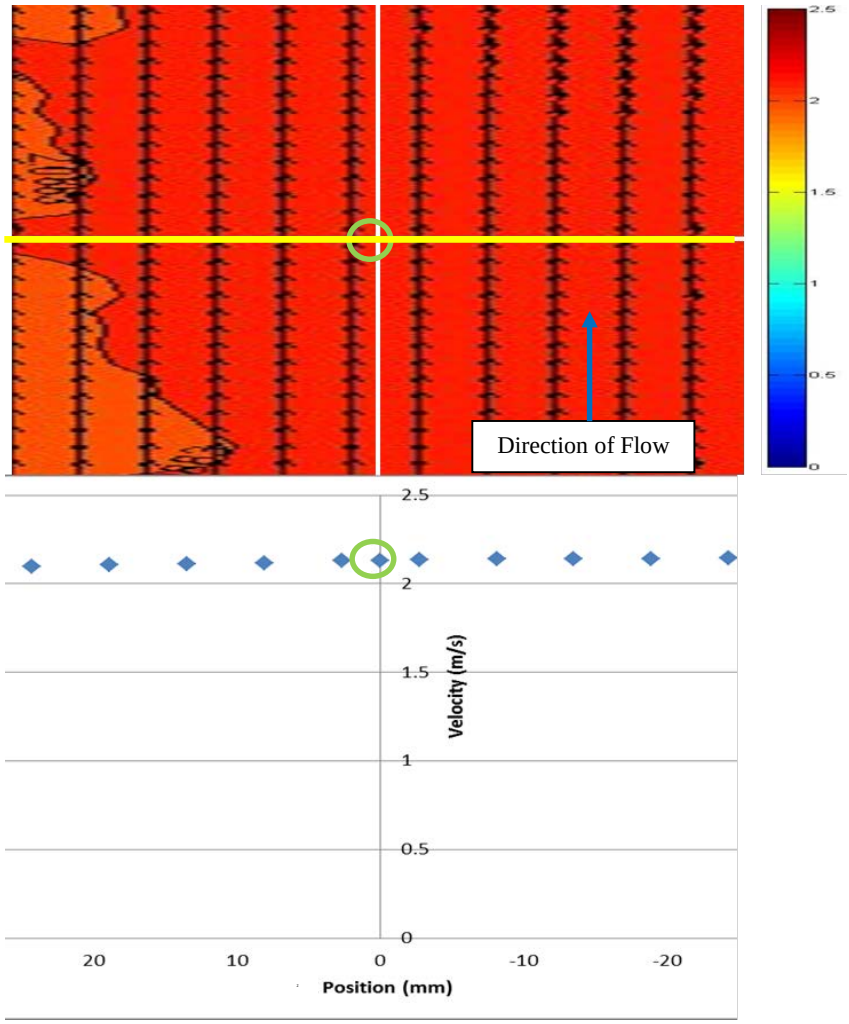

Figure 36: Velocity Profile of Chord A (30 Hz VFD Setting)

The background color in the velocity field image represents the flow velocity (m/s), as described by the color bar on the right side of the figure. The direction of flow is in the positive X direction, as denoted by the blue arrow. The green circle around the origin at the center of the velocity field represents the single point used for analysis, as this is the only point that fell within the circular applicable cross section (see Figure 1 in Chapter 3 for applicable cross section diagram). Discrete velocity data extracted along the Z axis (at X=0, denoted by the yellow line) are represented in the scatter plot below the velocity field image. The single velocity point used is also circled in green in the plot.

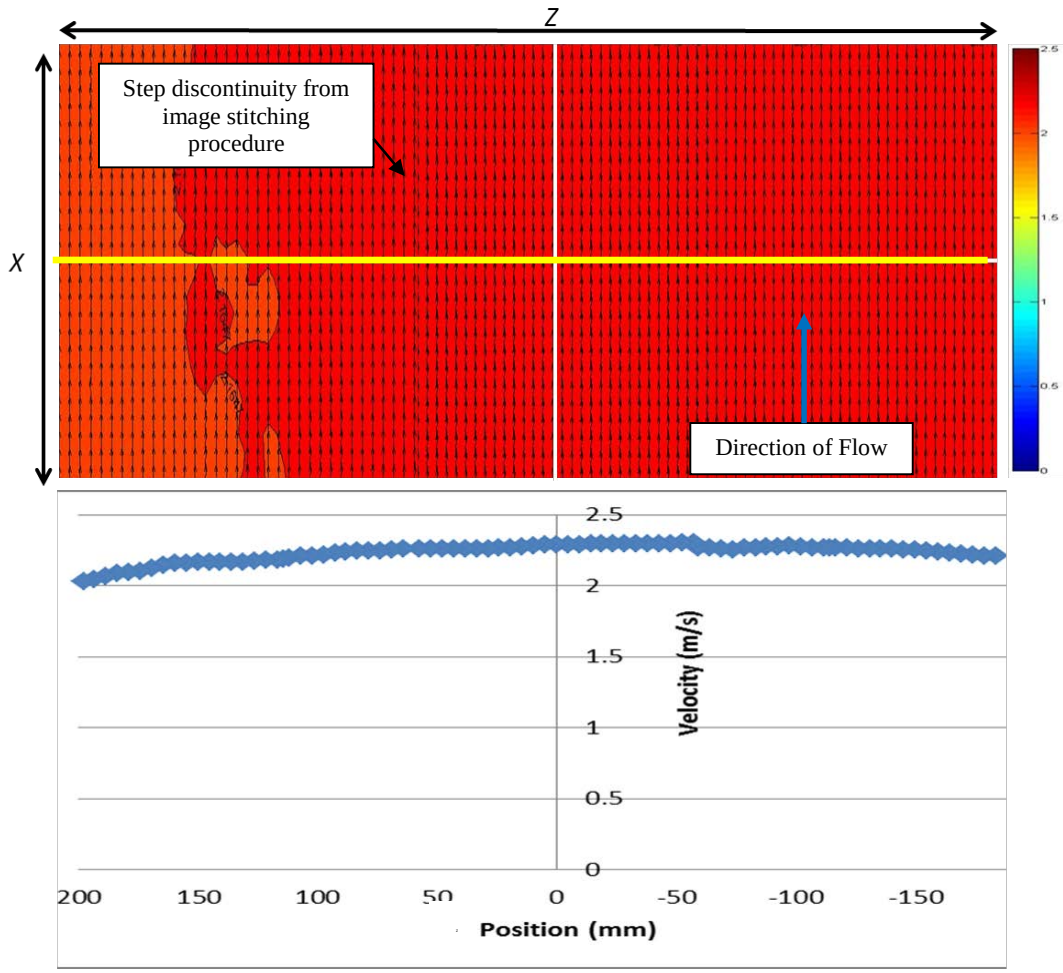

Figure 37: Velocity Profile of Chord B (30 Hz VFD Setting)

The background color in the velocity field image represents the flow velocity (m/s), as described by the color bar on the right side of the figure. The direction of flow is in the positive X direction, as denoted by the blue arrow. Discrete velocity data extracted along the Z axis (at X=0, denoted by the yellow line) are represented in the scatter plot below the velocity field image. The apparent asymmetry of the color flood indicates that either the camera was not exactly centered when establishing the center of the chord line or that there is a slight imbalance of velocity flow at the edges of the applicable cross section. The step discontinuities in the velocity field are the results of imperfect stitching between subsections.

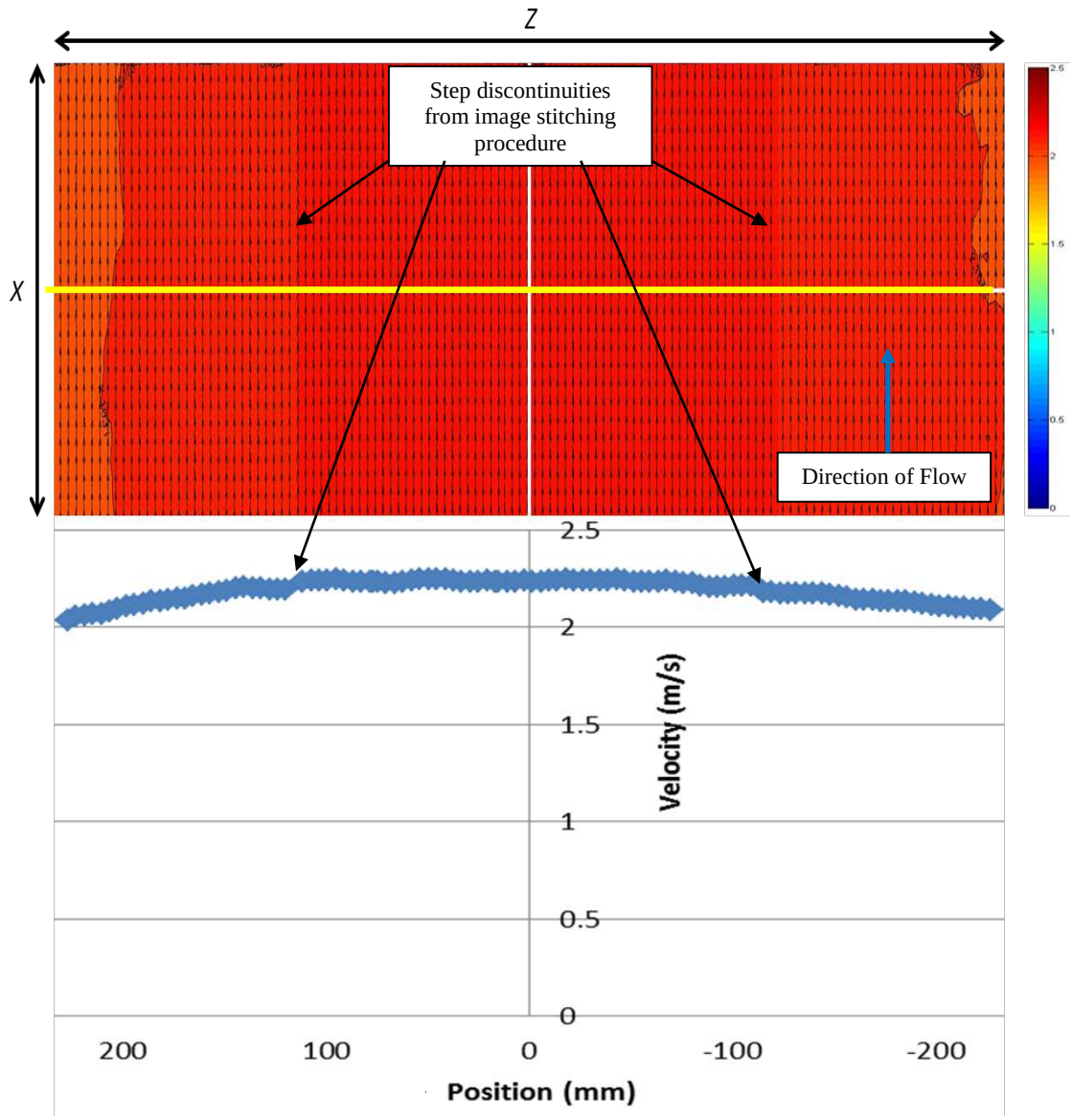

Figure 38: Velocity Profile of Chord C (30 Hz VFD Setting)

The background color in the velocity field image represents the flow velocity (m/s), as described by the color bar on the right side of the figure. The direction of flow is in the positive X direction, as denoted by the blue arrow. Discrete velocity data extracted along the Z axis (at X=0, denoted by the yellow line) are represented in the scatter plot below the velocity field image. The step discontinuities in the velocity field are the results of imperfect stitching between subsections.

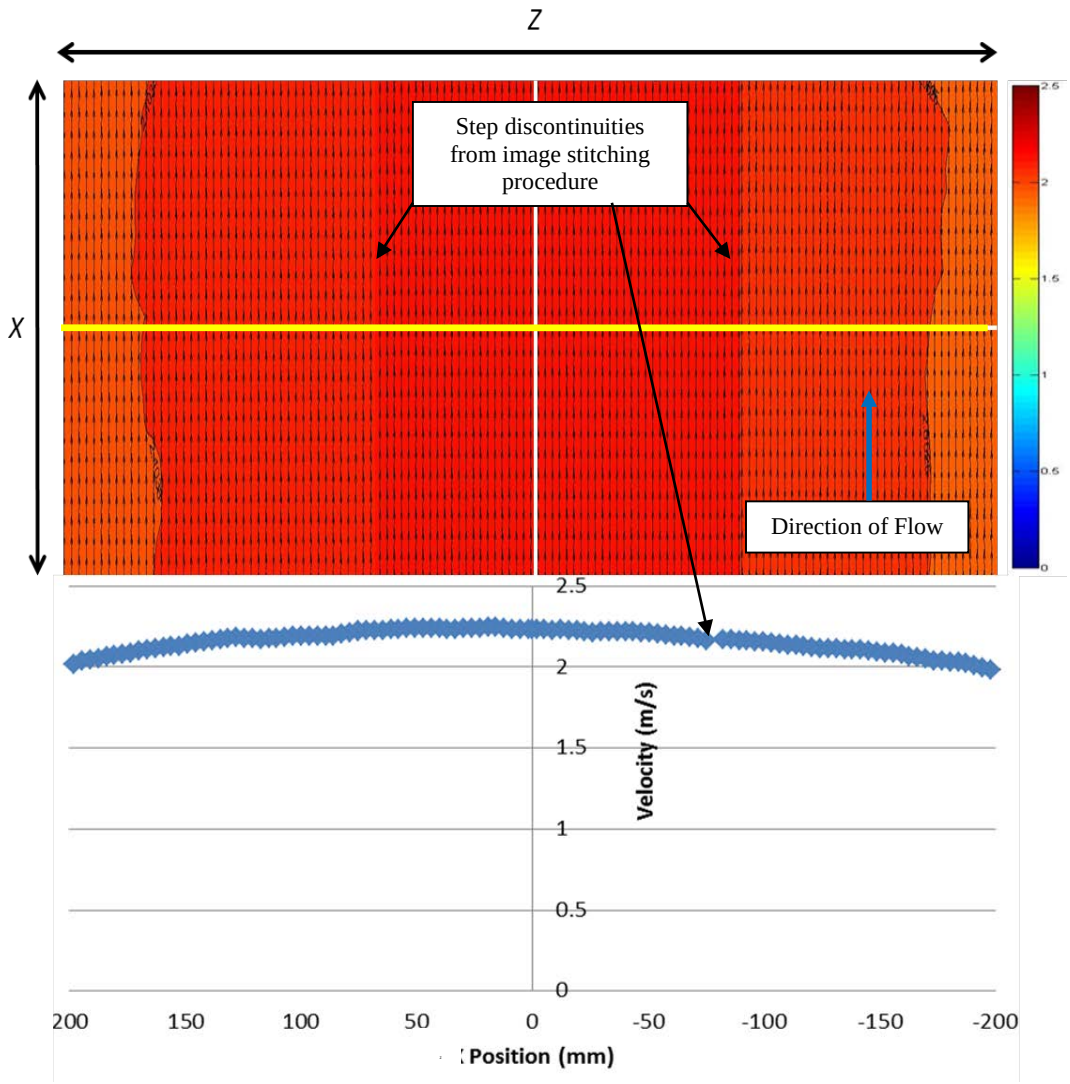

Figure 39: Velocity Profile of Chord D (30 Hz VFD Setting)

The background colors in the velocity field image represent the flow velocity (m/s), as described by the color bar on the right side of the figure. The direction of flow is in the positive X direction, as denoted by the blue arrow. Discrete velocity data extracted along the Z axis (at X=0, denoted by the yellow line) are represented in the scatter plot below the velocity field image. The step discontinuities in the velocity field are the results of imperfect stitching between subsections.

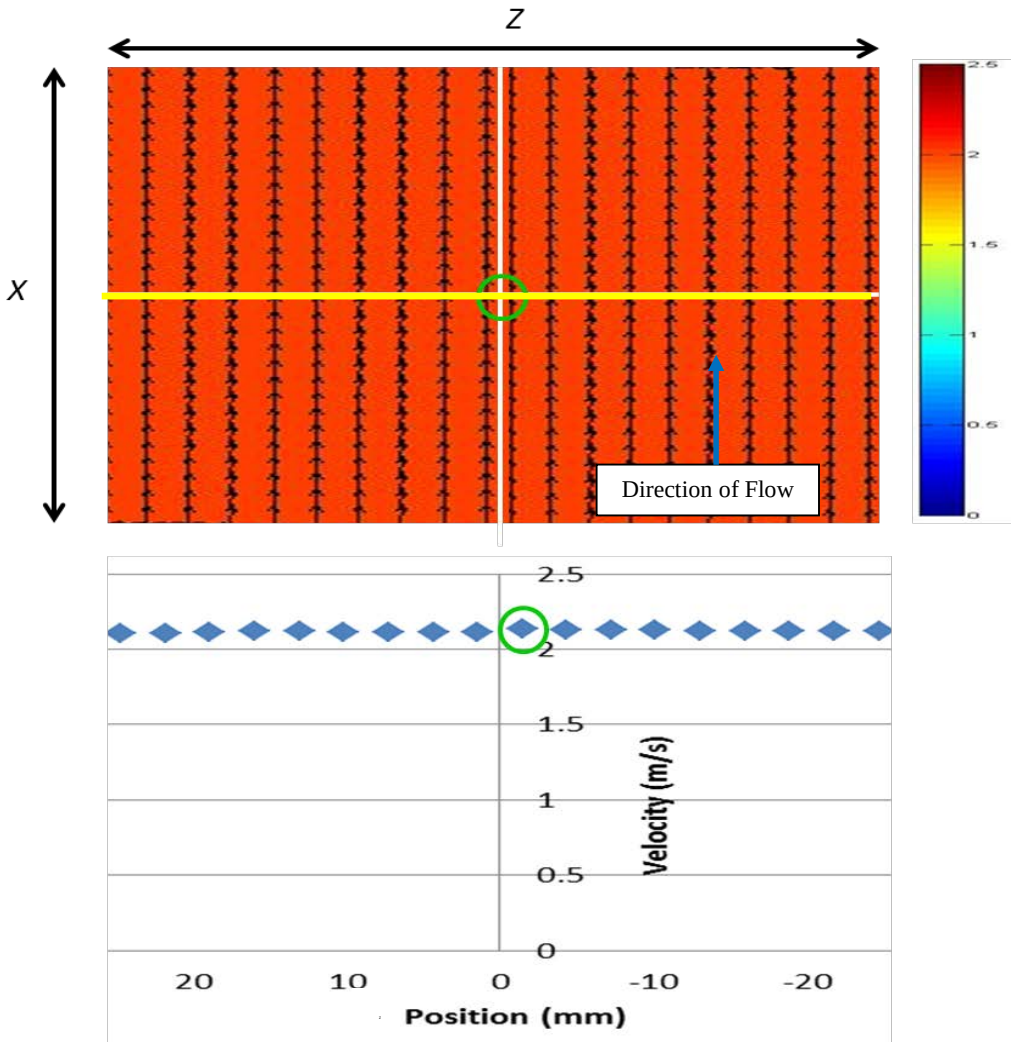

Figure 40: Velocity Profile of Chord E (30 Hz VFD Setting)

The background color in the velocity field image represents the flow velocity (m/s), as described by the color bar on the right side of the figure. The direction of flow is in the positive X direction, as denoted by the blue arrow. The green circle around the origin at the center of the velocity field represents the single point used for analysis, as this is the only point that fell within the circular applicable cross section (see Figure 1 in Chapter 3 for applicable cross section diagram). Discrete velocity data extracted along the Z axis (at X=0, denoted by the yellow line) is represented in the scatter plot below the velocity field image. The single velocity point used is also circled in green in the plot.

The results of the 15 Hz VFD setting velocity tests found only three points at the extreme edges of the defined cross section that exceeded the 10 percent of mean limitation (denoted with red circles in Figures 33 and 34), and the 30 Hz VFD setting velocity tests

found zero points falling outside the acceptable range (see Appendix A for PIV precision analysis and Appendix B for PIV accuracy analysis). Figures 41 and 42 are box-and-whisker plots of the velocity profiles for 15 Hz and 30 Hz VSD setting tests, respectively, across all chord lines, A-E.

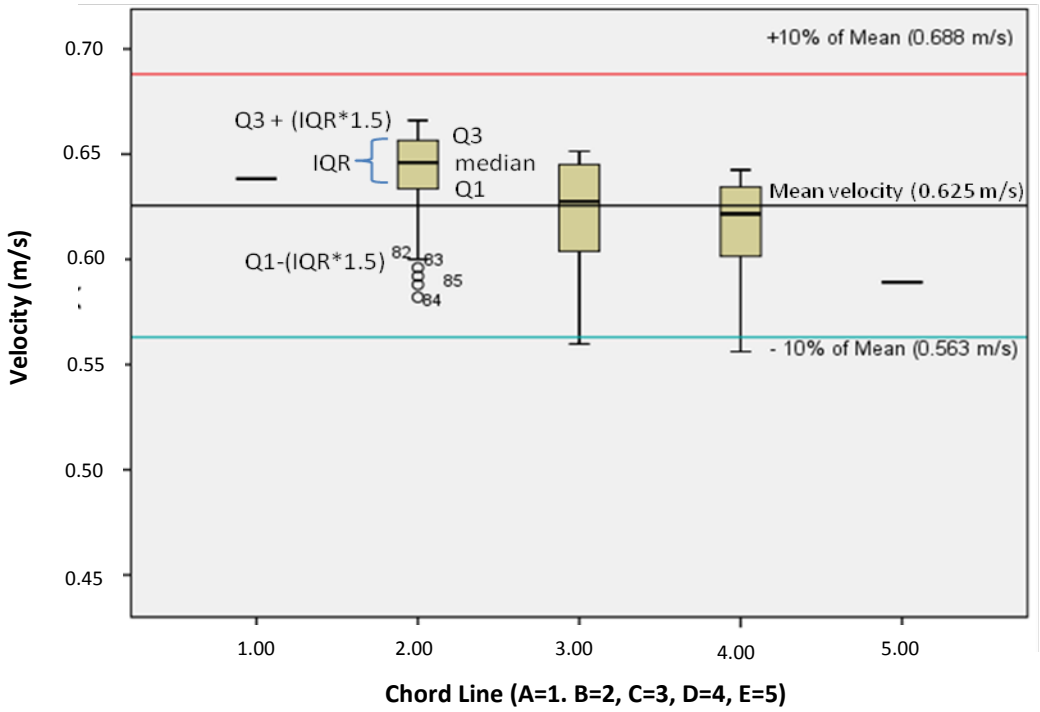

Figure 41: Box and Whisker Plot of Velocity (m/s) vs. Chord Line for the 15 Hz VFD Test

The distribution of discrete velocity values extracted along each chord line (A-E, represented along the X axis as 1-5, respectively) are shown as individual boxes in the box-and-whisker plot. Chords A and E consisted only of a single point each and are therefore shown here as single horizontal lines. The yellow boxes describe the inter- quartile ranges (IQR) of the velocity value populations for Chords B, C, and D. The black line running across each box represents the median value of each velocity value population (Q2). The 5 circles below the Chord B lower whisker end represent outliers that fell outside of this range. The solid black line running across the plot represents the mean velocity of all chord lines (0.625 m/s); the blue line represents 0.563 m/s (-10 percent of the overall mean); and the red line represents 0.688 m/s (+ 10 percent of the overall mean).

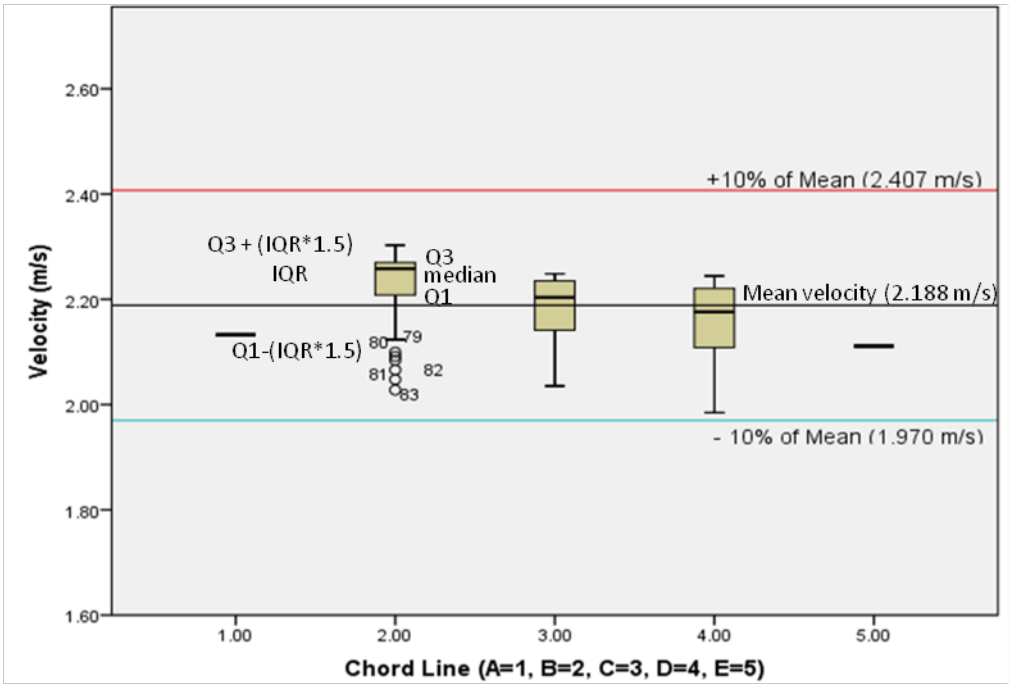

Figure 42: Box and Whisker Plot of Velocity (m/s) vs. Chord Line for the 30 Hz VFD Test

The distribution of discrete velocity values extracted along each chord line are shown as individual boxes in the box-and-whisker plot. Chords A and E consisted only of a single point each and are therefore shown here as single horizontal lines. The inter-quartile (IQR) range (Q1 through Q3) is represented by the yellow boxes, with the whisker ends representing ± 1.5 times the IQR. The circles below the Chord B lower whisker end represent outliers that fell outside of this range. The solid black line running across the plot represents the mean velocity of all chord lines (2.188 m/s); the blue line represents 1.907 m/s (-10 percent of the overall mean); and the red line represents 2.407 m/s (+ 10 percent of the overall mean).

Figure 41 demonstrates that the points falling outside the 10 percent of the mean limitation on Chords C and D were outside of the interquartile ranges (IQR) for their respective chord lengths. Figure 42 shows that all velocity values from the 30 Hz test were within the 10 percent of the mean standard. Tables 11 and 12 summarize the average velocities by chord and VFD setting.

	15 Hz VFD Setting	
	Average Nominal Velocity (m/s)	PIV Velocity Uncertainty (± m/s)
Chord A	0.626	0.012
Chord B	0.643	0.011
Chord C	0.617	0.009
Chord D	0.607	0.008
Chord E	0.574	0.007
Avg	0.6134	0.012

	30 Hz VFD Setting	
	Average Nominal Velocity (m/s)	PIV Velocity Uncertainty (± m/s)
Chord A	2.127	0.060
Chord B	2.323	0.053
Chord C	2.187	0.046
Chord D	2.16	0.039
Chord E	2.119	0.033
Avg	2.1832	0.06

Tables 10 (Left) and 11 (Right): Average PIV Velocities by Chord and VFD Setting

The average velocities across each chord length for the two VFD settings are presented in the tables above. The nominal velocities represent the average of the PIV output. The PIV velocity uncertainties were calculated for each chord line using the methods outlined in Kline and McClintock (1953). The nominal PIV velocities were averaged to establish an overall mean velocity against which individual velocity measurements are compared. The PIV uncertainty of the overall mean is assumed to be the worst-case uncertainty from the individual chords.

The PIV velocity uncertainties were determined with confidence intervals of 95 percent (19:1) by employing the methods outlined in 1953 by Kline and McClintock (see Appendix A for details).

Chord B contained the highest number of low outliers, which is likely due to the apparent asymmetry of the chord as a whole, which will be discussed further in Chapter 5 (see Figures 32 and 37 for velocity field visualization). Additionally, after the velocity profiles had been characterized, it was apparent that the VFD settings needed to be adjusted (see section 3.1.3 for discussion on initial VFD settings). The 30 Hz setting was slightly lower than the targeted 2.22 m/s (-1.76 percent averaged across all chord lines), and the 15 Hz setting was much too high, as the average overall velocity for this test was greater than 10 percent of the 0.556 m/s target (+10.3 percent averaged across all chord lines). Consequently, before beginning the next phase of aerosol concentration characterization, the VSD frequency settings were adjusted to 13 Hz for the 2 km/hr target and 31.5 Hz for the 8 km/hr target.

To help quantify the entire velocity value populations for each test beyond the within ± 10 percent of the mean standard, the $C_{v\%}$ statistic was calculated for each test (see Chapter 3 for calculation method) to shed light on how closely related the measured velocities were across all chord lines for each of the two VFD settings. The $C_{v\%}$ values were found to be 3.8 percent for the 15 Hz test and 3.4 percent for the 30 Hz test, which demonstrates the high degree of velocity uniformity across the test section.

4.2 Results of Aerosol Concentration Characterization

40 CFR 53 Subparts D and F (EPA, 1987 and 1997) state that for each aerosol aerodynamic diameter / target wind tunnel velocity combination, 5 evenly-spaced isokinetic samplers must be used to collect test aerosols upon a glass fiber filter. The glass fiber filter is soaked in a specific volume of aliquot solution to extract the 5 percent uranine / oleic acid (m/m) solution resulting from the collected aerosols, and a calibrated fluorometer is employed to calculate the concentration (ppb) of fluorescent dye (uranine) present in the new sample solution. From that data, the aerosol concentration at the inlet of an individual sampling cone (C_{iso}) is calculated ($\mathrm{mg/m^3}$). For the experimental setup used in this research, a single isokinetic test run was conducted for each 90 degree rotation of the rake head, totaling 40 runs (4 rotations per target aerosol size; 5 target aerosol sizes per VFD frequency setting; 2 VFD frequency settings). From each run, 4 mass concentration samples were taken with isokinetic sampling cones, resulting in 160 total concentration samples for which C_{iso} values were calculated. Tables 12-16 show the $C_{v\%}$ values for each individual test run, with each run consisting of 4 individual samples.

Size	Speed	Position	Cv%
3µm	2km/hr	Position A	1.33
		Position B	3.18
		Position C	6.07
		Position D	2.52
	8km/hr	Position A	12.48
		Position B	4.45
		Position C	4.37
		Position D	7.69

Size	Speed	Position	Cv%
7µm	2km/hr	Position A	16.03
		Position B	5.80
		Position C	2.14
		Position D	3.32
	8km/hr	Position A	2.03
		Position B	4.50
		Position C	2.08
		Position D	2.37

Size	Speed	Position	Cv%
10µm	2km/hr	Position A	4.74
		Position B	12.53
		Position C	2.48
		Position D	4.66
	8km/hr	Position A	3.50
		Position B	3.89
		Position C	5.62
		Position D	3.66

Size	Speed	Position	Cv%
13µm	2km/hr	Position A	8.72
		Position B	11.45
		Position C	2.80
		Position D	5.23
	8km/hr	Position A	12.93
		Position B	7.43
		Position C	8.63
		Position D	7.76

Size	Speed	Position	Cv%
17µm	2km/hr	Position A	8.88
		Position B	10.30
		Position C	12.50
		Position D	9.84
	8km/hr	Position A	14.40
		Position B	8.75
		Position C	13.61
		Position D	1.76

Tables 12-16 (Upper Left to Bottom Right): $C_{v\%}$ Calculations By Isokinetic Test Run

The tables are organized by target aerodynamic diameter (3, 7, 10, 13, and 17 µm). Each size was tested at two target wind tunnel velocities (speed), 2 km/ hr (13 Hz VFD setting) and 8 km/hr (31.5 Hz VFD setting). For each speed / size combination, the isokinetic rake head was rotated 90 degrees four times (positions A though D). Finally, for each size / speed / position combination (or individual test run), the $C_{v\%}$ value was calculated for the 4 isokinetic cone samples using the procedures discussed in section 3.2.5 of Chapter 3. The fields highlighted in yellow indicate $C_{v\%}$ values where one of the samples was discarded due to the sample C_{iso} concentration value exceeding 2 standard deviations of the mean for an entire size / speed combination. The fields highlighted in red are values that exceed the 10 percent standard.

Once all samples were analyzed with the fluorometer and the C_{iso} values calculated, they were grouped in individual runs as shown in Tables 12-16, as well as together in aerodynamic diameter / target wind velocity combinations (16 samples each). The mean C_{iso} for the 16 samples was calculated, and any C_{iso} value that fell outside two standard deviations of the mean was assumed to be an error in sampling procedure and discarded. The $C_{v\%}$ values highlighted in yellow in indicate individual test runs where a sample was omitted. The fields highlighted in red indicate $C_{v\%}$ that exceed the 10 percent standard.

The $C_{v\%}$ values were lowest in the middle range of sizes. The 3 µm tests were conducted over a period of 5 days, as each test run lasted six hours, making it difficult to keep the VOAG jet running continuously throughout that time. The individual C_{iso} concentrations for these runs were also on the low end of the fluorometer's calibrated range (approximately 15 ppb), despite initial calculations targeting the values at approximately 30 ppb. Performance at the 17 µm aerosol diameter tests was poor, particularly over the 2 km/hr target tests.

The original goal of this concentration characterization plan was to calculate a $C_{v\%}$ value for every mean aerosol aerodynamic diameter / wind tunnel velocity combination. If all the C_{iso} values from all four rake positions (A-D) could have been combined and analyzed together, then a single value describing how effectively the wind tunnel disperses a specific particle size at a specific wind speed could have been calculated. However, because there was a significant variation of the average C_{iso} between individual runs (each individual rake position), and because all 16 samples were

not taken simultaneously and concentration can shift between runs, direct combination of all 16 C_{iso} values was invalidated. This could indicate that the change in experimental setup between runs (rotation of the rake and the removal and re-installment of isokinetic assemblies) has a large impact on the imprecision of the sampling procedure (further discussed in section 5.2.3). A comparison between the $C_{v\%}$ values for each individual run, however, can be made to quantify the overall performance of the wind tunnel to gain a better understanding of the concentration profile for each aerodynamic diameter / wind tunnel velocity combination. One must be cautious in interpreting this comparison, however. It cannot be used as a substitute for an overall $C_{v\%}$ value, as it does not compare the C_{iso} values directly. If only the median $C_{v\%}$ values were examined, the overall variation of the $C_{v\%}$ values would be masked, and one may reach the incorrect conclusion that the tunnel aerosol concentration characterization only suffered unacceptably high $C_{v\%}$ values when testing with the 17 µm aerosols. The box and whisker plots in Figure 43 show not only the median $C_{v\%}$ for each aerosol aerodynamic diameter / target wind tunnel velocity combination, but also illustrate the variation of the data.

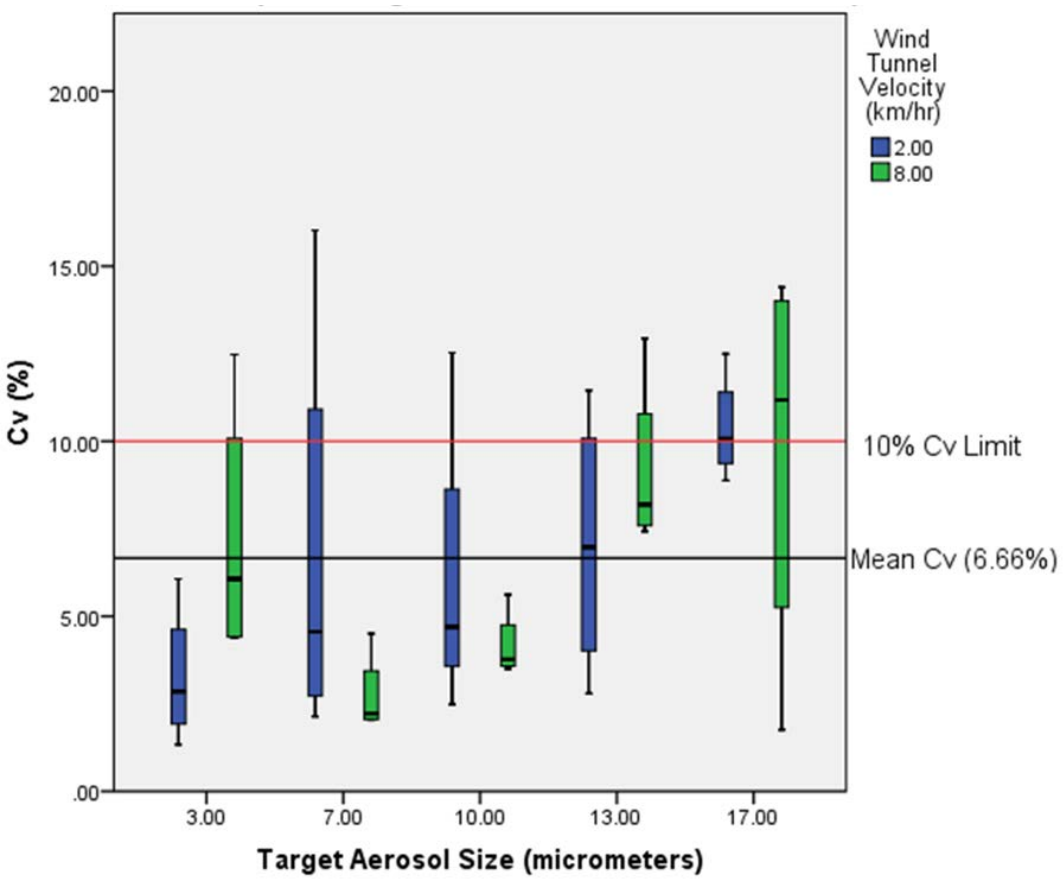

Figure 43: $C_{v\%}$ of Sample Runs vs. Target Aerosol Size Sorted by Velocity

Each box and whisker plot represents the 4 $C_{v\%}$ values calculated for each target aerosol size (µm) / wind velocity (km/hr) combination. For example, the first plot at the left hand side of the chart shows the results of the 3 µm tests at a target wind tunnel velocity of 2 km/hr, and is comprised of the $C_{v\%}$ values 1.33 percent (rake position A), 3.18 percent (rake position B), 6.07 percent (rake position C), and 2.52 percent (rake position D). The solid black line through the middle of each box represents the median value of the data set and is not representative of any single sample. The blue boxes represent the 2 km/hr tests, and the green the 8 km/hr tests. The solid red line running across the chart represents the 10 percent C_v limit. The solid black line running across the chart represents the overall mean $C_{v\%}$ value of 6.66 percent.

Figure 34 shows that despite the fact that the majority of the median $C_{v\%}$ values for each size / velocity combination fall below the 10 percent limit, there are 9 $C_{v\%}$ values for individual runs that exceeded the standard. Additionally, the median value for the 17 µm tests exceeded the 10 percent limit.

The aerosol dispersion wind tunnel efficiency coefficient (or percent efficiency) quantifies the concentration of the aerosol droplets observed in the test section versus the concentration expected assuming no losses. The expected concentration was calculated from the function generator frequency, which is the aerosol flow rate from the VOAG, for example 75,000 Hz = 75,000 droplets / second, aerodynamic diameter of the droplets, and wind speed. The observed value was calculated from the isokinetic samples (C_{iso}).

size	velocity	expected (mg/m^3)	observed (mg/m^3)	% efficiency
3 µm	2 km/hr	0.00272	0.00195	71.69
	8 km/hr	0.00065	0.00043	66.15
7 µm	2 km/hr	0.03678	0.02911	79.15
	8 km/hr	0.00874	0.00729	83.41
10 µm	2 km/hr	0.24224	0.14681	60.61
	8 km/hr	0.05756	0.02766	48.05
13 µm	2 km/hr	0.25264	0.13963	55.27
	8 km/hr	0.06003	0.03287	54.76
17 µm	2 km/hr	0.57066	0.11159	19.55
	8 km/hr	0.13561	0.02820	20.79

Table 17: Efficiency Coefficients (percent) for Size and Speed
The efficiency coefficients (percent) were determined by calculating the ratio between the expected concentration in the test section (assuming no losses) and the observed isokinetic sampler concentrations (C_{iso}).

This chapter presented the results of the velocity and concentration profile tests. The velocity profiles at both the 2 km/hr target wind velocity (15 Hz VFD setting) and 8 km/hr target wind velocity (30 Hz VFD setting) showed a high degree of uniformity, with only three total 2 km/hr target velocity values falling outside the required ± 10 percent of the overall mean at the very far edges of the applicable cross section in Chords C and D.

The $C_{v\%}$ values for the extracted velocity vectors in the 2 km/hr and 8 km/hr tests were 3.8% and 3.4%, respectively, which again demonstrates the homogeneity of the velocity field throughout the applicable cross section. The concentration profile showed variations in $C_{v\%}$ values between droplet sizes and target wind tunnel airflow velocities, with a significant decline in performance from the larger (13 and 17 µm) aerosol tests. In Chapter 5 the results of the PIV Velocity Characterization are discussed, including the apparent asymmetry of the velocity flow fields, (particularly at Chord B), and the actual wind velocity versus the target wind velocity. Section 5.2 discusses in detail the aerosol concentration profile, including the high $C_{v\%}$ values, the possibility of an insufficient number of sampling positions, and the further discussion of C_{iso} values between test runs.

CHAPTER 5

DISCUSSION

Chapter 4 presented the results of the velocity profile and aerosol concentration characterization tests. These results showed strong uniformity in the velocity flow field at both target airflow velocities, with only 3 discrete velocity vectors exceeding the ± 10 percent of the overall mean standard at the extreme edges of the applicable cross section (Chords C and D from the 2 km/hr tests, see Figures 33 and 34). The aerosol concentration profile characterization showed the majority of the $C_{v\%}$ values for the runs (31 of the 40) were within the 10 percent $C_{v\%}$ standard. Generally, the smaller test aerosols had lower $C_{v\%}$ values than the larger, with the 17 µm test producing the highest number of values that did not meet the standard. Chapter 5 discusses these results in greater detail. For the PIV tests, this chapter specifically addresses the issues of velocity flow field asymmetry as well as the variation between the target wind speed velocity and the actual wind speed velocity. For the aerosol concentration characterization, this chapter discusses the high $C_{v\%}$ values; the possibility of an insufficient number of sampling positions; and the problem with direct comparison of C_{iso} values between test runs.

5.1 PIV Velocity Characterization

The results of the PIV characterization prove that the velocity profile across the applicable cross section is sufficiently uniform to satisfy the standards set by 40 CFR 50

Subparts D and F (EPA, 1987 and 1997). For the 15 Hz VFD setting tests, only three individual data points at the far edges of Chords C and D exceeded 10 percent of the mean, and zero points from the 30 Hz VFD setting tests exceeded the standard. The three points that fell outside the 10 percent limit can easily be avoided in future applications if the applicable cross section is reduced to correspond with the size of sampler being tested. In addition, two other concerns came to light upon data analysis. Chord B showed a distinct asymmetry in the positive Z direction, and the VFD settings needed to be adjusted in order to better achieve the 2km/hr (0.556 m/s) and 8 km/hr (2.22 m/s) targets. These issues are discussed below.

5.1.1 Apparent Asymmetry of the Velocity Flow Fields

The matching procedure from the PIV position coordinates to the overall Cartesian coordinate system describing the cross section appears to have been slightly skewed in some cases, as the center lines in reference to the apparent flow symmetry in Figures 32 and 37 appear to be shifted in the positive Z direction. The procedure for centering the CCD camera on the origin was done simply by turning the capture mode of the camera to “free and continuous,” (which did not fire the laser and allowed for continuous video-like imaging of the inside of the tunnel) and moving the camera with the traverse system until the center of the image was focused on the center of the NIST traceable ruler. Each subsection was then defined with fields-of-view as the camera was moved along the Z axis, using the ruler and the edges of the fields-of-view as reference. This may have proved to be imprecise in some instances and could be the reason for the shifts. Causes for this imprecision could stem from the ruler not being perfectly aligned with the Z axis, which would lead to an improper definition of the Chord center, skewing

it in the positive Z direction. It is unlikely that there is an imbalance in wind speed velocity, as this feature only presents itself in the Chord B tests. If there were such a severe spatial velocity imbalance within the cross section, there would be evidence of it in the other chord lines.

5.1.2 Actual Velocity vs. Target Velocity

40 CFR 53.42 states that when conducting a test on an instrument, the actual wind tunnel speed must be within 10 percent of the target velocity. As became apparent during the velocity characterization, the frequency setting of the VSD (15Hz) was too high, resulting in an inappropriate power setting during the 2km/hr (≈ 0.556 m/s) tests (+10.3 percent of target). Originally, a linear correlation curve of VSD frequency setting to velocity was determined experimentally using a hot-wire anemometer over a wide range of frequency settings (5Hz to 60 Hz), as multiple changes to the wind tunnel flow (see Appendix D for examples) were made. After the data was analyzed, it was found that the curve behaved poorly at the lower frequency settings, but adequate at the higher, as the frequency setting used when characterizing the flow at the ≈ 2.22 m/s target (30 Hz) resulted in a deviation of -1.4 percent. The correlation curve with higher data resolution should be re-analyzed over a narrower target range to produce a regression curve with a better fit.

5.2 Aerosol Concentration Characterization

The aerosol concentration characterization tests performed best in the mid-size range (7µm to 13µm), and relatively poorly at the 3µm and 17µm test runs. Additionally,

the isokinetic rake sampling scheme left data-sparse regions that should be resolved to better characterize the true concentration profile.

5.2.1 High $C_{v\%}$ Values

The 3 µm tests were the first set of tests conducted, as the test runs were by far the longest. 6 hours of testing was necessary for each individual run (as opposed to 2 hours for the 7 µm tests, 1 hour for the 10 µm tests, and 30 minutes for both the 13 µm and 17 µm tests) in order to collect sufficient mass to be read by the fluorometer. Because these test runs were so long, the VOAG jet had to be restarted between runs. Even though the mass geometric standard deviation for each run was relatively low (approximately1.07), the restarting of the VOAG jet resulted in individual test populations that were close, but not identical to each other. This made it difficult to truly compare across all rake positions for this size. Additionally, despite the length of the test, the concentrations gathered by the cones were still fairly low (approximately 15 ppb). As discussed in section 3.2.1, the "medium" sensitivity range was used for the fluorometer tests. Turner Designs (1997) suggests this sensitivity setting if a wide range of concentrations between 5 and 100 ppb is expected, and that the calibration standard be prepared near the 50% of range (50 ppb was used). Because the end concentrations were not yet known, these suggestions were used for this research, and as a result the end concentrations for the 3 µm tests fell at the lower end of the calibrated range. Even so, Turner Designs (1997) states that the fluorometer is extremely accurate and forgiving, often times regardless of the selected sensitivity range or calibration standard used. It is therefore possible, but unlikely, that the low concentration values are a significant source of error. It is far more likely that a significant imprecision in collection procedure is the cause of the wide

variation when dealing with lower concentrations. As discussed in section 3.2.5, the cones were removed from the manifold, the filters soaked in the aliquot, and the inside of the cones rinsed to collect any fluorescent tracer collected upon the inner surface. The thoroughness of the rinse and the collection of the rinse aliquot may have a significant effect in this concentration range.

The poor performance of the 17 µm tests could indicate two things. First, that the runs were not long enough and more droplets needed to be collected on the filters in order to get a representative value. It was assumed that a test length comparable to those of the 13 µm and 10 µm tests would be sufficient; however, as became apparent when calculating the dispersion efficiency coefficient at the 17 µm aerosol (approximately 20 percent, see Table 17 for efficiency coefficients), too many droplets were impacting upon the interior surfaces of the wind tunnel and not making it downstream into the test sections. Second, the larger droplets with their high inertia followed the flow imprecisely and were very susceptible to under-and-over sampling due to imperfect isokinetic conditions at the rake. The sharp drop-off in efficiency at 17µm demonstrates the importance of the balance between flow modification devices and efficiency.

5.2.2 Insufficient Sampling Positions

As shown in Figure 18, there are large areas of the cross section that, given the sampling design, went largely un-sampled. While the rake did comply with the regulation, which only calls for five sampling points per size / velocity test (USEPA 1987), the map of the sampling sites brings to light the holes in the sampling zone. This could be remedied by either constructing a new rake with more cones (this would require an additional vacuum pump to achieve sufficient flow through the rake), or by

performing additional rotations of the rake. For instance, instead of four rake positions at 90 degrees from one another, eight could be completed at 45 degrees from one another.

5.2.3 Comparing C_{iso} Values between Runs

Section 4.2 stated that the original intention was to compare all C_{iso} values from all four rake position runs over a given aerosol size test, yielding a complete concentration profile with a single overall $C_{v\%}$ value per aerosol size and speed. However, this comparison could not be made as the average C_{iso} values between runs were dissimilar, indicating the presence of a significantly imprecise element to the aerosol collection procedure. Between each run, the cones were removed and sampled, the rake rotated, and the cones re-installed. Due to these changes in experimental setup, it is inappropriate to directly compare the C_{iso} values between runs. To do so would be to mask the variability of the procedure, which could lead to incorrect assumptions of test performance. Therefore, the $C_{v\%}$ values of each run were compared to one another, but not averaged together. To average them would be to inappropriately describe the aerosol concentration distribution for each aerosol size over all rake positions. The best that can be achieved by using the methods described in this research is to describe the aerosol concentration by both aerosol size *and* rake position.

In this chapter, the results from Chapter 4 were analyzed and discussed in detail. The PIV velocity characterization showed that the measured velocity flow fields across the 5 chord lines (A-E) were sufficiently uniform (discrete velocity measurements within ± 10 percent of the overall mean velocity) at both target velocities (2 km/hr and 8 km/hr). Only three discrete measurements did not meet the standard at the extreme edges of Chords C and D for the 2 km/hr target velocity test (Figures 33 and 34 show these points

and their position within the flow field); however, simply reducing the diameter of the applicable cross section will resolve this issue. All velocity measurements within the flow field for the 8 km/hr target velocity tests met the standard. The apparent asymmetry of the velocity flow fields, particularly Chord B, is likely the result of an imprecise designation of the chord center and not the result of a physical imbalance in flow velocity along the Z axis. Additionally, a significant variation exists between the actual mean velocity within the test section and the target velocity, most notably for the 2 km/hr tests (+ 10.3 percent). This was due to the improper VFD frequency setting and was corrected by lowering the setting from 15 Hz to 13 Hz prior to characterizing the aerosol concentration profile.

The aerosol concentration characterization showed the highest uniformity over the mid-sized droplets (7, 10, and 13 µm). The 3 µm and 17 µm tests showed relatively poor concentration distribution. The high $C_{v\%}$ values over the 3 µm tests was attributed to lower than expected mass collection upon the glass fiber filters due to insufficient run time. The low concentrations allow for low precision in the sampling procedure, where small inconsistencies in sample processing have a large affect on the analysis. The high $C_{v\%}$ values for the 17 µm droplet tests was attributed to a low dispersion efficiency coefficient at this size, which also resulted in a lower than expected mass collected upon the filters. In both cases, a longer sampling time should be employed, and for the 17 µm tests, the 50% porosity flow straightener plate could be removed from the tunnel section to increase the dispersion efficiency coefficient.

Chapter 6 discusses possible remedies to the issues discussed above, and could be implemented in future research to achieve a truer picture of the velocity and

concentration profiles across the applicable cross section. In addition, Chapter 6 outlines recommendations for how to proceed in testing field nephelometers Auvermann (2012) plans to use to calculate the mass flux of a dust cloud over a beef cattle feedyard during the morning or evening dust peak.

CHAPTER 6

RECOMMENDATIONS FOR FUTURE RESEARCH

Chapter 5 discussed the results of the EQRTL Aerosol Dispersion Wind Tunnel velocity profile and aerosol concentration characterizations and gave insight on the possible causes of irregularities in the testing. The PIV velocity characterization showed high velocity uniformity within the applicable cross section at both target velocities; however, the overall velocity fields appeared to be skewed in the positive Z direction and the actual measured mean velocity, particularly at the 2 km/hr test, did not match the target velocity (the mean velocity must fall within 5 percent of the target velocity in order to be a valid test, EPA 1987 and 1997). The concentration distribution profile showed the highest degree of uniformity when testing with the mid-sized droplets (7, 10, and 13 µm), but relatively poor uniformity at the 3 µm and 17 µm droplet tests. Inconsistencies in isokinetic sampling procedures, low concentrations due to insufficient experimental run time, and a low dispersion efficiency coefficient (for the 17 µm test size) were discussed as primary reasons for these high $C_{v\%}$ values. Chapter 6 discusses possible solutions to these issues, as well as recommendations for increasing the precision of the PIV velocity measurements and recommendations on the future characterization of the field nephelometers proposed by Auvermann (2012) for use in air quality testing below an atmospheric inversion over a beef cattle feedyard.

6.1 Recommendation for Correcting the Apparent Asymmetry Chord B

As discussed in Chapter 5, Chord B appeared to be shifted in the positive Z direction, thus slightly skewing the velocity profile. This could be the result of a misalignment of the NIST traceable ruler when establishing camera fields-of-view across the test section. In the future, instead of relying on shifting the field-of-view along the ruler, the experimenter can use the Insight software to input pre-set traverse positions into the computer, which will automatically move the arm holding the camera to the specified coordinates. The experimenter could find the exact center of the chord line and perform the calibration procedure discussed in Chapter 3. From the calibration factor, the movements along the Z axis could be accurately calculated to center the camera in the next chord subsection with little to no perceptible asymmetry. This would remove much of the human error associated with the camera movement.

6.2 Recommendations for Improvement in PIV Precision

Appendix A describes the method used to calculate the overall precision of the PIV velocity measurements using the procedures described by Kline and McClintock (1953). While the study of PIV precision is ongoing and highly specific to the application for which it is being used, the uncertainty analysis described in Appendix A finds that the two single largest factors affecting the precision of measurement are the calibration procedure error and the CCD pixel displacement (the distance an aerosol pattern moves between images, in pixels). Table A-2 shows that if a Δt is selected which results in a pixel displacement of less than 5 pixels, the precision of measurement climbs above the required 2 percent. Therefore, care must be taken to be sure a proper Δt is

chosen that allows for both high precision of measurement (> 5 pixels) and high statistical confidence in tracking aerosol patterns between images (< 15 pixels).

6.3 Recommendations for Improved Isokinetic Aerosol Sampling

While the rake design and sampling scheme provided more than the required 5 evenly-spaced isokinetic testing positions per aerosol test size (EPA, 1987), problems with precision and sampling resolution became apparent as the data was analyzed. Therefore it would be beneficial to construct a new isokinetic rake with more sampling cones (which would require the acquisition of either stronger vacuum pumps or a third vacuum pump to be run in parallel to the others to establish sufficient flow through the rake). More cones sampling at once would allow for direct comparison between the C_{iso} values from each sampler, yielding a better characterization (with a higher statistical confidence, as more samples could be evaluated as a sample population) of aerosol distribution.

In addition, the isokinetic conditions, while verified as being very nearly isokinetic using the PIV system, could be improved by ensuring the cones are as exactly parallel to the air flow as possible between each sample run. Slight deviations in orientation could cause improper sampling conditions, especially with the larger aerosols. Because the cones were removed from the manifold, processed, and replaced for the new run, it is possible that the manifold, despite being secured by a clamp at its base, could have been slightly rotated and gone unnoticed. A quality assurance procedure using the PIV camera should thus be employed. Between each run, the ruler should be repositioned across Chord C, and the center cone of the manifold should be aligned with

the ruler. Using the PIV camera, the setup inside the tunnel could be observed using the "free and continuous" mode, and small adjustments made to the manifold orientation.

Regarding the poor performance of the 17 µm isokinetic tests, it may be beneficial to remove the 50 percent porosity flow straightener plate installed downwind of the turbulator. It is likely that the plate, while helping to minimize the induced swirl caused by the turbulator, is causing substantial impaction of droplets, especially at the larger sizes. The velocity distribution is likely to suffer (see Appendix C for velocity profile prior to tunnel modifications), but if it can be kept within limits, it may aid in improving the aerosol distribution efficiency (thus yielding more representative $C_{v\%}$ values) at the larger target aerosol sizes.

6.4 Recommendations to Improve Microscopy Inspection of Impacted Aerosol Spheroids

The precision of measuring the CCD-imaged impacted aerosol spheroid using the Omnimet click-and-drag sizing function (± 1 pixel) proved insufficient when sizing the smaller aerosols, and therefore could not be reliably used as singular direct sizing technique. By acquiring an ocular micrometer (a glass slide with a ruled scale that fits into the eyepiece of the microscope), much of this imprecision would be eliminated. The stage micrometer is used to calibrate the ocular micrometer. Once it is calibrated, the ocular micrometer can be used in real time to size magnified objects without relying on the click-and-drag sizing function.

6.5 Recommendations for Future Nephelometer Characterization

The EQRTL Aerosol Dispersion Wind Tunnel was modified, tested, and characterized to evaluate candidate ambient air quality sensors under controlled

conditions. One such sensor is a small nephelometer capable of measuring 0 to 16 milligrams per cubic meter (mg/m^3) of ambient dust in increments of 0.02 mg/m^3 (Klar). The Auvermann team has proposed to use a vertical array of these sensors situated downwind of a test concentrated animal feeding operation to measure the particulate matter concentration of an emitted dust cloud typical during the morning/evening dust peak, when both atmospheric stability and animal activity is high. Using this data in conjunction with wind velocity data from collocated sonic anemometers, the Auvermann team plans to employ an integrated horizontal flux method, which will aid in characterizing the "vertical plume/velocity structure in the confined layer during the development of the short-term, evening inversion" (Auvermann 2012). In the course of testing the concentration profile of the tunnel, however, it was found that the VOAG was not capable of producing a sufficient droplet concentration for a full characterization downwind in the test section, especially at the 8km/hr speed. The 2km/hr concentrations at 7, 10, and 13 µm sizes are within the level of detectability with the maximum observed concentration of 0.161 mg/m^3 (cone 3, position A, 2km/hr, 13µm), however this level is still too low to truly characterize the nephelometer over its sensing range. One possible remedy is to employ an atomizer capable of producing a sufficient aerosol concentration of polystyrene latex spheres with fluorescent tags at a high enough flow rate to achieve the required 16 mg/m^3 in the test section. Additionally, TSI, Inc. offers a wide range of atomizers and aerosol generators capable of much higher concentrations than the VOAG, however none are capable of producing monodisperse aerosols. The new aerosol generator would have to be characterized with the APS for size distribution. If the particles are solid rather than liquid, the APS will

accurately size the particles. Once the new aerosol generator was characterized against the APS (which itself should be validated against NIST-traceable polystyrene latex spheres), the dust sensors could then be tested in the wind tunnel.

It was also found that when testing the functionality of the dust sensors, each individual unit will need to be re-calibrated against a standard. The units were originally calibrated using a Dust-Trak II 8530 Aerosol Monitor. A kitchen blender was used to agitate a dust sample inside an acrylic box, and a shop vacuum drew the dust from the blender and into the box. The Dust-Trak monitor sensor was collocated inside the acrylic box with the nephelometers. The nephelometers were then calibrated using a linear regression (y=mx+b) to the Dust-Trak measurements as the concentrations dropped from 16 mg/m^3 to 0 mg/m^3 (Klar). The slope (m) and the y-intercept (b) for each sensor can be manually adjusted to fit the line. Since that procedure was conducted, the calibrations of at least 3 sensors (sensors 8, 9, and 10) have drifted substantially, as no two sensors read the same when turned on to sample ambient air (sensor 8 read 0.42 mg/m^3, sensor 9 read 0.56 mg/m^3, and sensor 10 read 0.72 mg/m^3). The slope and y-intercept of each sensor will need to be re-adjusted against a standard before they can be properly characterized. This procedure could be done in the wind tunnel as well, assuming the aerosol generator was verified and capable of producing a predictable flow rate so downwind concentration could be accurately calculated and compared to the sensor output. A single isokinetic cone should also be similarly located with the sensor, thus providing a fluorometric (or gravimetric) standard with which to compare data.

CHAPTER 7

SUMMARY

The EQRTL Aerosol Dispersion Wind Tunnel has been characterized for both wind velocity distribution and aerosol concentration uniformity using the procedures and standards outlined in 40 CFR 53 Subparts D and F (USEPA, 1987 and 1997). In order for a wind tunnel to be used as an official test facility for candidate PM_{10} and / or $PM_{2.5}$ Federal Reference Method samplers, the tunnel must be capable of achieving sustained wind velocities of 2, 8, and 24 km/hr. The wind flow velocity must be sufficiently uniform across the applicable cross section (no discrete velocity measurement greater than ± 10 percent of the mean velocity, measured at no fewer than 12 evenly spaced points across the test section, using a method capable of 5% precision or better). The aerosol concentration profile must be verified as having a $C_{v\%}$ of no greater than 10 percent for each test run (measured by no fewer than 5 evenly spaced isokinetic sampling cones per test run). For PM_{10} FRM testing, the concentration profile must be established for all droplet sizes and wind speeds specified in Table D-2 from 40 CFR 53 Subpart D (USEPA, 1987, see also Table G-1 in Appendix G), and for $PM_{2.5}$ FRM testing, Table F-2 from 40 CFR 53 Subpart F (USEPA, 1997, see also Table G-2 in Appendix G) must be used. The percentage of aerosol multiplets to singlets within a test aerosol population must not exceed 10% (verified by microscopy), and the geometric standard deviation of each particle size cannot exceed 1.1.

For this research, the standards stated above (see Appendix G for more detail) were used as a guide to establish the velocity and aerosol concentration profiles. Using a TSI PIV laser system, 13 instantaneous velocity flow fields were imaged, calculated, and processed to describe the uniformity of the wind flow across five horizontal chord lines (A-E) throughout the cross section (see Figure 1 for a diagram showing chord positions and subsections across the test section). The cross section was interrogated at both the 2 km/hr and 8 km/hr wind speeds. The 24 km/hr wind speed was not tested, as the FSD 26 fan was not capable of sustaining this speed in the wind tunnel as configured. The velocity characterization showed a high uniformity across all velocity flow fields, with the exception of three discrete velocity measurements taken at the extreme edges of Chords C and D for the 2 km/hr tests. However, by simply reducing the diameter of the applicable cross section, this issue can be eliminated. The overall flow fields, especially at Chord B, seemed to be skewed in the Z direction. This was most likely the result of improperly defining the center of the cross section, which in turn led to conversion errors between the PIV image-specific coordinates to the overall Cartesian coordinates describing the applicable cross section of the tunnel. This can be remedied by using the EQRTL traverse system to establish the field-of-view widths (hence the width of the subsections and individual velocity flow fields) rather than trying to establish the widths of the fields-of-view by moving the PIV camera along the Z axis and using the ruler inside the tunnel as a reference guide. The traverse system is programmable, and the coordinate system could be developed using basic geometry prior to interrogation, thus ensuring precise movements along the Z axis not as susceptible to human error.

The test droplets used for the characterization of the aerosol concentration profile were generated using a VOAG. The droplets were composed of a 5 percent (by mass) fluorescent tracer (uranine) to oleic acid solution diluted in isopropyl alcohol. The unique dilution of the oleic acid/uranine solution to the isopropyl alcohol for each target aerosol size was calculated using the principles outlined by Berglund and Liu (1973). Once the VOAG was producing monodisperse particles of the desired aerodynamic diameter and the geometric standard deviation of the droplet sizes was 1.1 or less (measured by the APS), an impactor collected a sample of the droplets upon a glass slide coated with Nyebar Type L surfactant and the impacted spheroids were analyzed for size as well as number of multiplets. This was repeated for each test droplet size (3, 7, 10, 13 and 17 μm). Each test aerosol was introduced into the wind tunnel at both 2 km/hr and 8 km/hr. An isokinetic rake fitted with four isokinetic sampling cones (cones 1-4), each cone housing a borosilicate glass fiber filter, was positioned inside the test chamber. Isokinetic conditions were established using two Gast rotary vane vacuum pumps, the airflow monitored using Dwyer manometers and controlled with a ball valve throttle. A test aerosol was introduced into the tunnel, and the isokinetic sampling cones collected droplets onto the glass fiber filters over a specific length of time. Each aerosol was run 4 times at both wind tunnel test velocities. For each run, the isokinetic rake was rotated 90 degrees around the center cone (rake positions A-D), resulting in 16 samples per test aerosol and wind velocity (160 total samples). The glass fiber filters were removed from the sampling cones after each run and soaked in a 1:1 (by volume) aliquot solution of isopropyl alcohol and distilled water for 24 hours (4 to 6 drops of sodium hydroxide were added to each sample stabilize the pH of the solution). A calibrated fluorometer

measured the concentration of fluorescent tracer within the samples (C_{iso}), and a $C_{v\%}$ was calculated for each test run. The results of these tests showed a higher uniformity ($C_{v\%}$ less than 10 percent) for the test aerosols in the mid-sized ranges (7, 10, and 13 µm) and poor uniformity ($C_{v\%}$ greater than 10%) at the 3 µm and 17 µm sizes. The poor uniformities at these sizes were both attributed to insufficient mass collected upon the filters, as the mean C_{iso} values for these test runs were lower than expected. These low concentrations exacerbate the impact of inconsistencies in the cone processing procedure (removal from the rake, precision of aliquot volume measurement using a graduated cylinder, and cone rinsing procedure). A simple increase in run time should help the consistency of the 3 µm results. For the 17 µm tests, however, it would also be prudent to remove the 50 percent porosity flow straightener plate located 1 diameter downwind of the turbulator in the tunnel section. This would decrease the degree of droplet impaction occurring inside the wind tunnel, allowing more of the 17 µm particles to make it into the test section for isokinetic sampling.

The original intent was to calculate a single $C_{v\%}$ value of each test aerosol size at a target wind velocity over all four rake positions; however the mean C_{iso} value of each run over all test sizes differed significantly, thus invalidating a direct comparison between individual runs. It is likely that a significant element of imprecision exists and was unaccounted for between the experimental configurations of each run (cones removed and re-installed, rake rotated, isokinetic flow rate re-established), which resulted in low repeatability of results. Therefore it is suggested that a new rake be constructed and fitted with more sampling cones, allowing for simultaneous isokinetic sampling of

the cross section at each aerosol test size and target wind velocity without inadvertently modifying the test conditions between runs.

The main goal of this research was to validate a wind tunnel testing facility that could be used to characterize ambient air samplers for air quality analysis. One such sampler is a nephelometer unit capable of quantifying the concentration of dust entrained in the air above a beef cattle feed yard during an atmospheric inversion. The results of this research show that the EQRTL Aerosol Dispersion Wind Tunnel is indeed capable of conducting these tests, but to calibrate and test the nephelometers properly, the concentration of test aerosols within the test section must be able to reach 16 mg/m^3 (the upper detection limit of the sensors). As currently configured with the VOAG and flow control devices, the maximum achievable concentration is 0.16 mg/m^3. While this is above the lower detection limit of the sensors, it is not sufficient to test the whole range of the unit. Therefore, it is suggested that an alternative to the VOAG be used capable of producing more particles at a higher feed rate (for example, a dust generator) for full nephelometer characterization.

APPENDIX A

PIV UNCERTAINTY ANALYSIS

Before there could be confidence in the PIV velocity measurements, it was necessary to quantify the accuracy and uncertainty of the data specific to the experimental setup used in this research. As discussed in Chapter 2, this is extremely important, as variances in PIV applications and experimental configurations result in vast differences in the influence of individual uncertainties propagated into the final measurements. It is not sufficient to simply look at previous PIV research using a wholly different setup for a dissimilar application. Therefore, the overall uncertainty of the PIV calculations were calculated using the single-sample uncertainty principles discussed in Kline and McClintock (1953), which are discussed below.

For most experiments, it is not practical to take multiple measurements with several instruments measured by multiple observers. If it were, one could simply use descriptive statistics and be confident in the reliability of measurement, as the biases of each observer and instrument type could be distributed across a single sample population. Experiments that are conducted in this manner are called multi-sample experiments. As it is, however, multi-sample experiments are usually not possible, and a single observer uses a single instrument to make an experimental measurement. This type of experiment is called a single-sample experiment (Kline and McClintock, 1953).

To quantify how the uncertainty values of data gathered from simple-sample experiments propagate and affect the final experimental results, Kline and McClintock (1953) state that the precision (or uncertainty) of each variable used in a particular calculation is identified with reference to a set uncertainty interval, assuming a normal distribution of the sample population if multiple measurements were made. For example, in this research, an analog manometer was used to measure pressure velocity inside the tunnel. The analog scale of the manometer was 0.005 inches or water (in H_2O). An observer can be nearly certain that his or her reading using this scale is within 0.005 in H_2O of the "true" value. Therefore, to apply this to a normal distribution, the observer can consider the end points along the X axis of the normal curve 0.000 in H_2O and 0.005 in H_2O, representing 4 standard deviations from the assumed mean (in this case, 0.0025 in H_2O). From here, the observer needs only to decide what level of confidence he or she would like to use. For this research, 2 standard deviations from the mean were used where applicable, equating to confidence interval of approximately 95 percent (or if using the notation of Kline and McClintock, 19:1). This confidence interval must be applied to each variable uncertainty value in order to know the confidence interval at the end of the procedure. The report of each nominal value for a measurement should have the following format (derived from Kline and McClintock, 1953):

$$m_n \pm w_n, \text{ (b to 1)}$$

where m_n = the nominal value of a measurement *n*; w = the uncertainty of the measurement *n*; and b = the numerator in the confidence interval. Again using the

manometer example, if a measurement of 0.022 in H_2O was observed, then the format of this value would be

$$0.022 \pm 0.00125 \text{ in } H_2O \text{ (19 to 1).}$$

Once the nominal values and uncertainties for each variable have been determined for a given function, the partial derivative of the function describing the calculation is taken with respect to each individual variable. For this example, consider the simple function describing a velocity calculation:

$$V = \frac{\Delta s}{\Delta t}$$

where V= velocity, Δs = displacement, and Δt = time elapsed. To convert to the nomenclature used in Kline and McClintock (1953), substitute R = V, m_1 = Δs, and m_2 = Δt.

$$R = \frac{m_1}{m_2}$$

Take the partial derivatives of the function R:

$$\partial R / \partial m_1 = \frac{1}{m_2}$$

$$\partial R / \partial m_2 = -\frac{m_1}{(m_2)^2}$$

Now the nominal values for the variables m_1 and m_2 are substituted. For this example, assume the arbitrary nominal values for m_1, m_2, w_1, and w_2:

m_1 = 6.4 ± 0.0125 m (19:1)

m_2 = 2.64 ± 0.00005 s (19:1)

Substitute:

$$R = 2.42 \text{ m/s}$$

$$\partial R/\partial m_1 = 0.15625$$

$$\delta R/\delta m_2 = -0.91827$$

Finally, the second-power equation defined in Kline and McClintock (1953) is applied:

$$w_R = [\left(\partial R/\partial m_1 \, w_1\right)^2 + \left(\partial R/\partial m_2 \, w_2\right)^2 + \cdots + \left(\partial R/\partial v_n \, w_n\right)^2]^{1/2}$$

Substitute and solve:

$$w_R = 0.00195$$

The velocity in this example would therefore be reported as 2.42 ± 0.00195 m/s (19:1). From here, a relative uncertainty can be calculated

$$=\left(\frac{w_R}{R}\right) * 100$$

resulting in a relative uncertainty of 0.0807 percent (19:1).

The following tables summarize the uncertainty analysis of the PIV velocity measurements when Kline and McClintock's uncertainty principles are applied. Each table represents a single calculation (or element of a calculation). These elements were identified as integral to the overall calculation of a single velocity vector within a velocity flow field.

First, the uncertainty of the calibration procedure was calculated across each of the 5 chord lines, as the calibration value of pixels/mm grew larger with a shorter camera focal distance between the camera lens and the interrogation region. The uncertainty of

the pixel length was assumed to be ± 0.5 pixels, as only a single pixel can be selected by clicking in the calibration procedure. The pixel lengths reported out to the hundredths place is misleading, because the length is determined by calculating the distance from the starting point (first click) to the end point (second click). If there is more than one dimension to the pixel length (for example, 387 pixels along the Z axis and 8 pixels along the X axis), the software will calculate the distance using the Pythagorean Theorem, rounded to the nearest hundredth. This does not mean it was possible to click down to $1/100^{th}$ of a pixel.

The reference length refers to the distance along the edge of the ruler over which the calibration was performed. The reference length for each calibration procedure was 2.00 inches (50.8 mm). The reference length uncertainty was based on the NIST traceable ruler used for calibration, with increments of 1/32 in. Applying the confidence interval of 95 percent, the uncertainty value 1/128 in (approximately 0.1984 mm) is reported.

	Pixel Length (±0.5 pixels)	Reference Length (±0.275 mm)	Nominal Calibration value (pixels/mm)	Calibration Precision (pixels/mm)	Calibration Uncertainty (%)
Chord A	358.00	50.8	7.05	0.0394	0.559
Chord B	405.08	50.8	7.97	0.0443	0.555
Chord C	465.03	50.8	9.15	0.0505	0.552
Chord D	550.01	50.8	10.83	0.0594	0.549
Chord E	665.09	50.8	13.09	0.0716	0.547

Table A-1: Uncertainty Analysis of the PIV Calibration Procedure

Pixel length measured by the click and drag feature of the image calibration function for the imaging software, and the reference length remained 50.8 mm for each calibration test. Nominal calibration values calculated by dividing pixel length by reference length. By applying the principles outlined in Kline and McClintock (1953), the calibration uncertainties for each chord line A-E were calculated using a confidence interval of 95 percent (19:1). As the nominal calibration value increased, the calibration uncertainty followed suit; however, the relative calibration uncertainty decreased.

The function describing the nominal calibration value calculation is straight forward (pixel length / reference length). As the pixel length grew, the corresponding nominal calibration value and respective calibration uncertainty did as well. However, the relative calibration uncertainty decreased as the nominal calibration value increased, indicating that a shorter focal distance (distance between the lens and the object being imaged) is preferable to a longer focal distance. This is because with a shorter focal distance, the field of view narrows (if leaning away from a ruler, one can see more of the ruler in their field of vision than if leaning toward the ruler), meaning more pixels can "fit" within the 50.8 mm reference length. This effectively results in a higher pixel to length resolution at the short focal distances than at the longer focal distances. With a higher pixel to length resolution, the influence of the calibration uncertainty is minimized with a larger nominal calibration value.

The individual nominal calibration values and uncertainties were used in turn to calculate the PIV velocity uncertainty. Like the example above, velocity is calculated simply be dividing displacement by Δt. With the PIV velocity calculations, however, the additional element of the PIV calibration is employed. The function used for this calculation is:

$$R = \frac{m_1}{m_2 * m_3}$$

where m_1= Δs ± 0.1 pixels; m_2= Δt ± 0.001 μs; and m_3= chord-specific calibration value ± the calibration uncertainties (pixel / mm) as defined in Table A-1.

The uncertainty of the Δt was taken from the published resolution of the synchronizer unit (1 nanosecond). The image specific displacement values come from

research conducted by Legrand et al. (2014) regarding the CCD error and the role it plays in PIV applications. The Legrand team discussed several sources of CCD error when used in PIV applications, including photon spillover between pixels (blooming); changes in ambient heat and humidity; data transfer "smearing" between the CCD sensor array and the CCD storage array (the second array allows for a faster Δt, as the image captured by the first array is immediately transposed to the second array where it awaits uploading to the data analysis system); and, most influentially, changes in illumination between laser pulses. Legrand et al. (2014) characterized a 4MP MegaPlus CCD camera, much like the camera used in this research, and found that when used in normal PIV operations with the typical difference in illumination between two pulses is approximately 20 percent, the associated CCD error equates to 0.005 pixels. It is possible, however, to minimize this difference by adjusting the power settings on the individual laser pulses through the Insight software (laser set-up menu). This was indeed accomplished in this research to achieve similar image brightness between the image pairs, which in turn aided in the number of "true" vectors when each image pair was analyzed for velocity vectors. The robust statistical model presented by Legrand et al. (2014), however, requires that the illumination values for each pulse be quantified for the associated uncertainty to be calculated, which was beyond the scope of this thesis. When combined with the error associated with peak-locking (referring to the statistical analysis to correlate aerosol patterns from one image to the next, see section 3.1.2), Legrand et al. (2014) found the overall pixel displacement error of the CCD camera / PIV system to be approximately 0.1 pixel. Despite the equalization of the EQRTL PIV laser pulse illumination, the conservative uncertainty value of 0.1 pixel was taken at face value, as it is uncertain to

what degree this equalization improved the uncertainty. Should this value be quantified, the model could be run and a new pixel displacement uncertainty could be applied. Table A-2 summarizes the velocity uncertainties as measured by the PIV, organized by chord line and Δt.

	Δt=1200 µs						
	CCD Pixel Displacement (±0.1 pixels)	Δt (±0.001 µs)	Nominal Calibration Value (pixels/mm)	Calibration Uncertainty (pixels/mm)	Nominal Velocity (m/s)	PIV Velocity Uncertainty (m/s)	Relative PIV Velocity Uncertainty (%)
Chord A	5.29	1200	7.05	0.0394	0.626	0.012	1.93
Chord B	6.07	1200	7.97	0.0443	0.634	0.011	1.70
Chord C	6.78	1200	9.15	0.0505	0.617	0.009	1.53
Chord D	7.89	1200	10.83	0.0594	0.607	0.008	1.33
Chord E	9.02	1200	13.09	0.0716	0.574	0.007	1.18
	Δt=240 µs						
	CCD Pixel Displacement (±0.1 pixels)	Δt (±0.001 µs)	Nominal Calibration Value (pixels/mm)	Calibration Uncertainty (pixels/mm)	Nominal Velocity (m/s)	PIV Velocity Uncertainty (m/s)	Relative PIV Velocity Uncertainty (%)
Chord A	3.60	240	7.05	0.0394	2.127	0.060	2.81
Chord B	4.45	240	7.97	0.0443	2.323	0.053	2.29
Chord C	4.80	240	9.15	0.0505	2.187	0.046	2.12
Chord D	5.61	240	10.83	0.0594	2.160	0.039	1.83
Chord E	6.66	240	13.09	0.0716	2.119	0.033	1.55

Table A-2: PIV Velocity Uncertainties by Chord Line and Δt

The uncertainties associated with the PIV velocity measurements vary by chord line (i.e. focal distance between the camera lens and the interrogation region), image pixel displacement (the number of apparent pixels the aerosol pattern traveled between images), Δt, and calibration value. The end uncertainties were calculated using the principles outlined in Kline and McClintock (1953). All uncertainty values were calculated using a confidence interval of 95 percent (19:1) where able; however, the CCD pixel displacement uncertainty was taken at face value from Legrand et al and was not transformed to a normal distribution.

To be compliant with 40 CFR 53 Subparts D and F, the measurement device used to characterize the velocity of the wind tunnel must have a precision of 2 percent or better. By applying the methods of Kline and McClintock (1953), all of the uncertainty values fall within that standard with the exception of Chords A-C when using a Δt of 240

μs. The reason for this becomes apparent when examining the short CCD pixel displacements associated with those chord line tests. TSI, Inc (2007) suggests employing a Δt that allows for at least a 5-pixel displacement. The stated reason for this was to ensure enough apparent displacement for the statistical analysis to follow the movement of the droplet patterns accurately between the two images. However, it becomes apparent that this 5 pixel threshold also plays a large part in the precision of measurement. By adjusting the Δt to a higher value (more time between images), the pixel displacement would increase to the required 5 to 15 pixels, which in turn would ensure that each velocity measurement pass the 5 percent uncertainty standard. Additionally, if a lens with a longer focal length were used in conjunction with the CCD camera, the calibration pixel to reference length resolution would be increased, thus reducing the calibration uncertainty value, which in turn would reduce the overall PIV velocity uncertainty value at the more distant chord lines (Chords A-C).

APPENDIX B

PIV ACCURACY VERIFICATION USING A PITOT PROBE WITH AN ANALOG MANOMETER

40 CFR 53.62, paragraph c-4, (USEPA, 1997) states that in a "full wind tunnel test" the velocity profile must be determined using no less than 12 discrete points within the cross sectional area. The measurement technique must be capable of a precision of 2 percent or better and accuracy of 5 percent or better. No single velocity at one any of these test points can deviate more than 10 percent of the mean velocity across all points. As shown in Appendix A, the precision of the PIV velocity measurements, when a Δt is used that allows for a pixel displacement of greater than 5 pixels, meets the precision (or uncertainty) standard. To calculate the PIV accuracy, however, the velocity values must be compared against a known, "true" number.

Using a Dwyer Series 160 stainless steel pitot probe and an Dwyer model 215 analog inclined scale manometer (original principle capable of measuring increments of ± 0.005 in H2O), the pressure velocity in the center of the tunnel's test section at three different blower frequency settings (40Hz, 50Hz and 60Hz) was measured and used to calculate air velocity using current barometric pressure and ambient temperature.

Figure B-1: Analog Manometer and Pitot Tube

With the pitot probe still inside the tunnel, the PIV laser sheet was aligned with the tip of the pitot probe and 100 pairs of images were taken at each fan speed setting. The spatial calibration factor was determined by taping a NIST certified ruler to the tip of the pitot probe, focusing the camera on the ruler, and capturing the calibration image. Figure B2 is an example of a single raw image captured of the pitot probe inside the tunnel (the pink shading on the side of the pitot tube is the result of over-exposed pixels associated with laser reflection from the stainless steel surface).

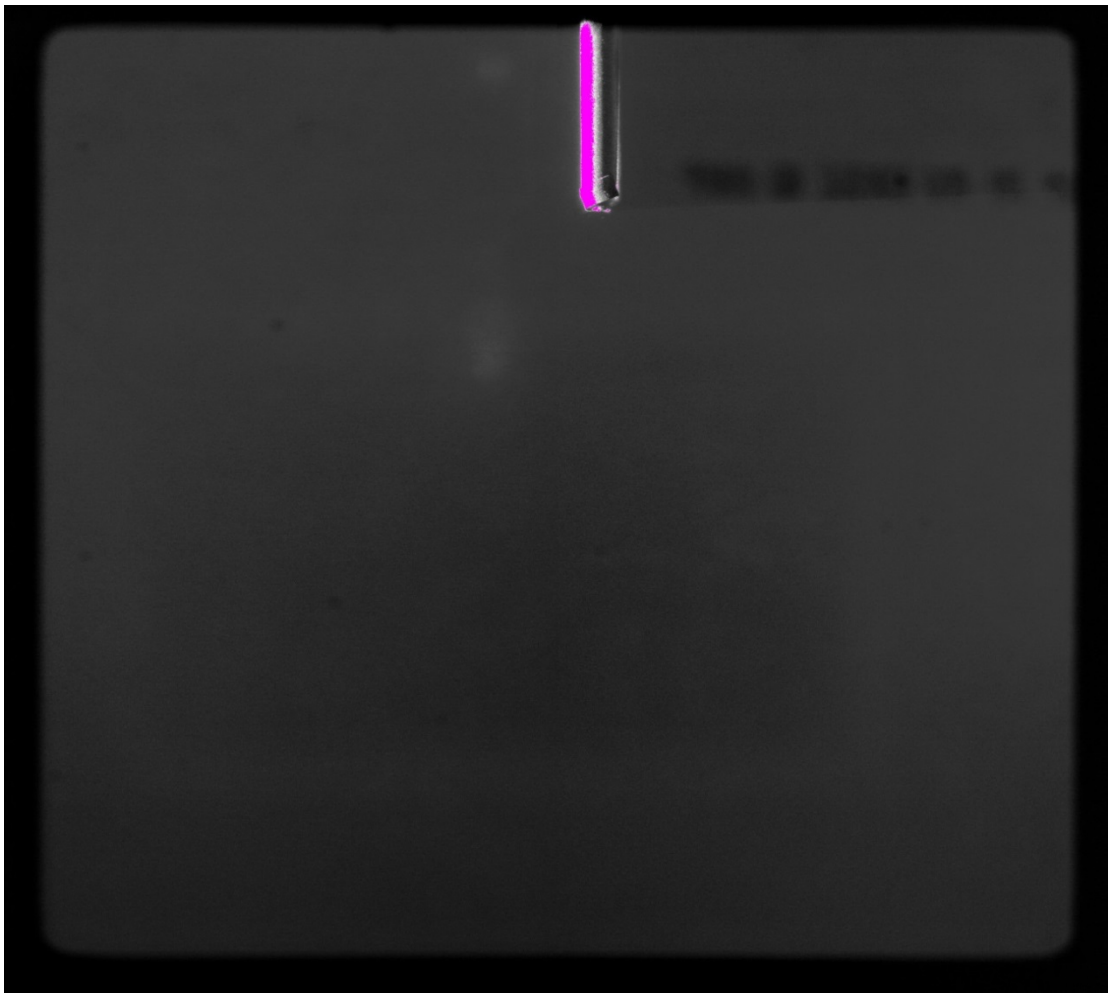

Figure B-2: Pitot Probe Raw Image

The tip of the pitot probe as aligned with the laser sheet at the center of the applicable cross section. The air flow is moving from the bottom of the image to the top. The pink pixels shading the left hand side of the probe are examples of over-exposed CCD pixels.

Once the image was captured, all images were processed, providing 100 velocity flow fields upstream of the pitot probe at each power setting. Figure B3 shows the calculated vectors over the raw pitot tube image.

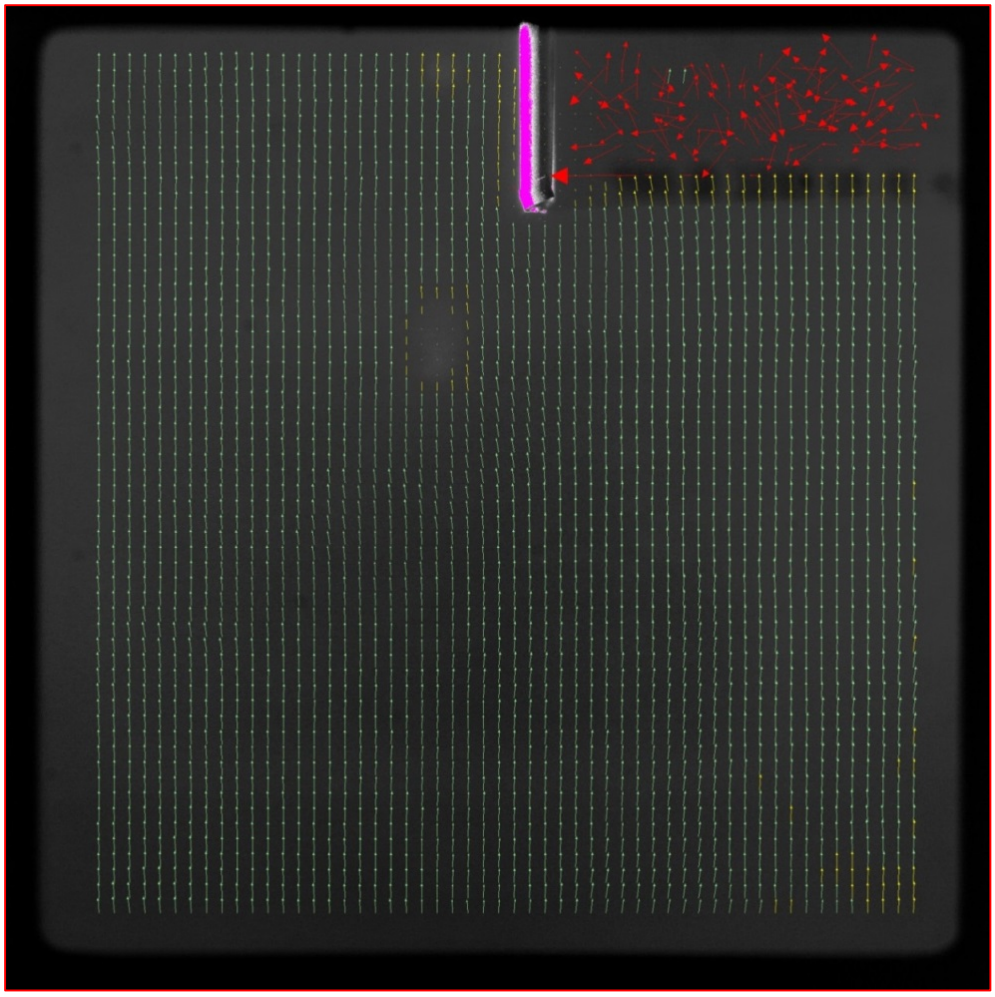

Figure B-3: Calculated Vectors from a Raw Image Pair

The green vectors indicate "true" values, meaning that the statistical analysis used to calculate the movement of aerosol patterns has a high statistical probability of being correctly determined. The red pixels in the upper right hand corner of the image show a number of "false" vectors, caused by the shadow of the pitot tube (the aerosols in that region were not illuminated, so the vector patterns could not be followed). Red vectors were excluded throughout the research.

Note the majority of the vectors are green in color, signifying strong statistical confidence that the vectors are "true." The interspersed yellow vectors represent interpolated velocity values over data-sparse regions. Red vectors represent low statistical confidence and were disregarded in data analysis throughout this research. The red vectors present in this figure are due to the shadow cast by the pitot tube, hiding the aerosol seed in this

region. It is also worth noting the small "dead spot" below and to the left of the pitot tip. This is likely the result of a smudge on the glass or a reflection on the ceiling of the test section that obscured the oleic acid droplets in this region.

Using Tecplot software, the velocity fields were averaged at each power setting, producing a total of 3 average velocity flow fields, one for each power setting. Then, using the average velocity flow field at each frequency setting, 50 velocity values were extracted along the streamline directly downwind to the tip of the pitot probe. Figure B4 shows an example of a single contoured Tecplot image of a velocity flow field around the pitot tube.

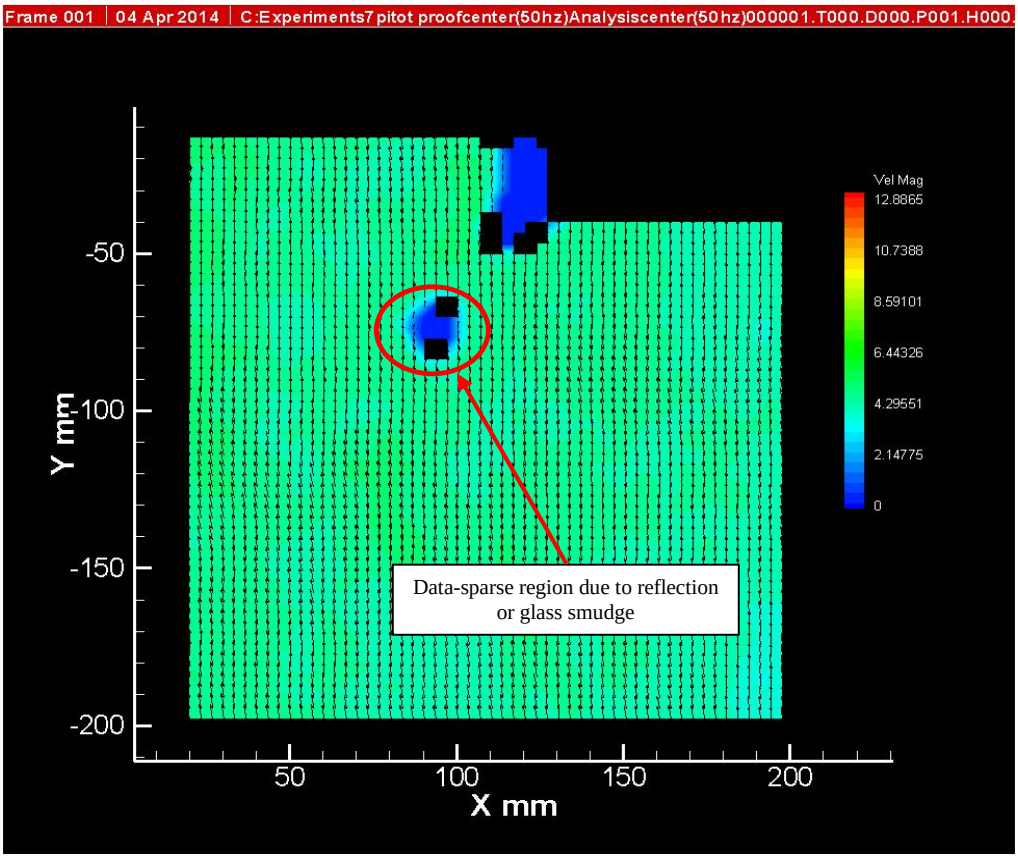

Figure B-4: Tecplot Image of Single Velocity Flowfield

The black vectors within the color flow field represent the direction and magnitude of air flow. The colors in the field represent velocities, as defined by the color bar on the right side of the figure. The ragged appearance of the color field shows how transient flow features move through the flow, and that the velocities across an area of interrogation at any one time are not distributed evenly. The area circled in red is the result of a data-sparse region where velocity aerosol patterns could not be resolved, likely the result of a smudge on the glass or a reflection inside the tunnel.

Figure B5 shows the calculated average velocity flow field around the pitot tube. The line drawn from the tip of the tube down to the bottom of the image represents the line from which 50 data points were extracted and analyzed.

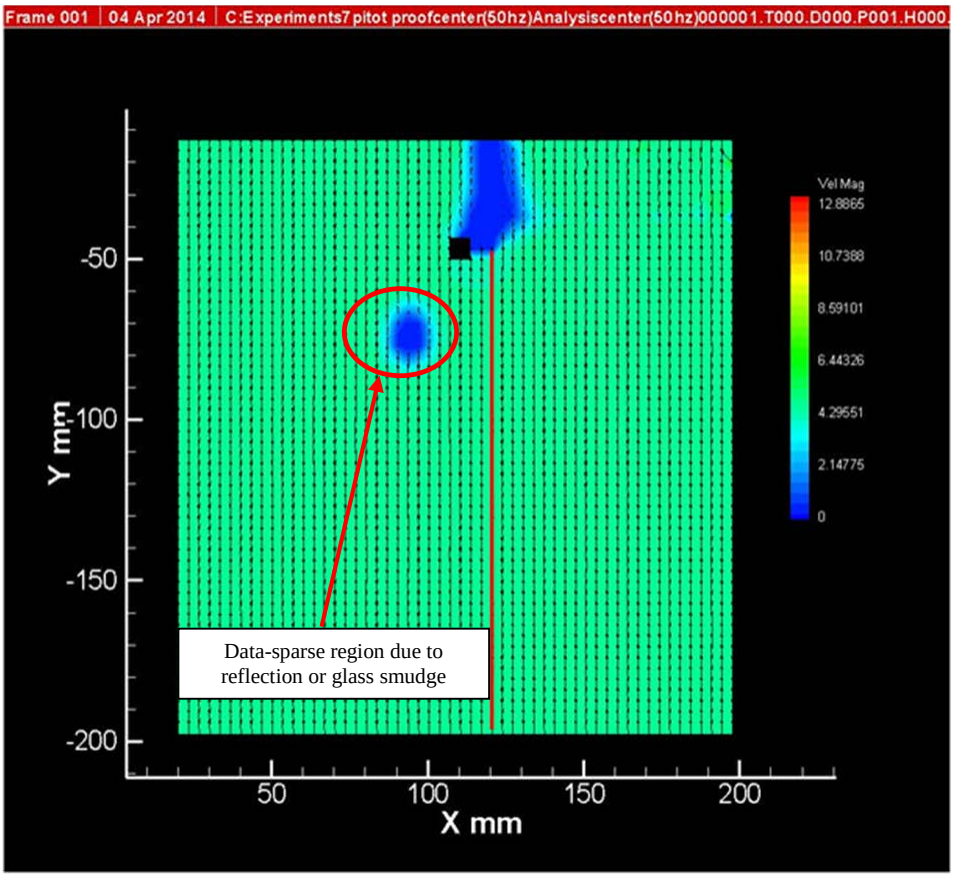

Figure B-5: Tecplot Image of an Averaged Velocity Flowfield

The black vectors within the color flow field represent the direction and magnitude of air flow. The colors in the field represent velocities, as defined by the color bar on the right side of the figure. The relatively smooth (as compared to Figure B-4) velocity flow field demonstrates how the transient features in the flow are averaged out to create a homogenous velocity flow field. The red line extending from the pitot tube tip represents the line from which the velocity values were extracted. The area circled in red is the result of a data-sparse region where velocity aerosol patterns could not be resolved, likely the result of a smudge on the glass or a reflection inside the tunnel.

While the pitot tube / manometer system is assumed to be a highly accurate velocity measurement standard (original principle method) and can thus be used to calculate the accuracy of the PIV system, the uncertainty of pitot tube / manometer measurement must be calculated to a 95 percent confidence level before a comparison

between the two can be truly made. To do this, the principles outlined in Appendix A (Kline and McClintock, 1953) were used. Table B1 summarizes.

VFD Setting	Air Density (±0.0000125 lbs/ft^3)*	Nominal Velocity Pressure (in H2O)	Velocity Pressure Precision (± in H2O)	Nominal Velocity (ft/min)	Velocity Uncertainty (ft/min)	Relative Velocity Uncertainty (%)
40 Hz	0.07509	0.022	0.000106	593	1.378	0.232
50 Hz	0.07509	0.043	0.000284	829	2.76	0.333
60 Hz	0.07509	0.073	0.000274	1080	1.97	0.182

Table B-1: Pitot Tube / Manometer Uncertainty Values by VFD Setting

**The air density was calculated using current barometric pressure and temperature. The air density uncertainty value of ± 0.0000125 lbs / ft^3 was calculated using the Kline and McClintock (1953) method. By contrast, the uncertainty for the nominal velocity pressure measurement was calculated by taking 20 velocity pressure readings over a minute at each VFD setting and setting the confidence interval at 95 percent (19:1). Using air density and velocity pressure as the two variables, the Kline and McClintock (1953) method was used to calculate the final velocity uncertainty for each VFD setting in m/s.*

The variables in this calculation were air density and velocity pressure. The function for the velocity calculation was described by the Bernoulli Principle. The uncertainty associated with the air density was calculated independently using the 1953 Kline and McClintock method, where ambient temperature (±0.005 degrees Fahrenheit) and barometric pressure (±0.005" Mercury) were used as variables (note that the original computations were made in standard units, as defined by the measurement equipment). For the pressure velocity uncertainty, repeated measurements were used (20 measurements over 60 seconds for each VFD setting) to determine the distribution of the values. From this distribution the uncertainty was determined relative to a 95 percent confidence interval (19:1). Finally, the Kline and McClintock method (1953) was employed to determine the uncertainty of the pitot tube / manometer velocity measurements (converted to m/s) with a 95 percent (19:1) confidence interval.

Tables B2 shows the PIV method meets the requirements specified by 40 CFR 53.62 (USEPA 1997) to conduct an official wind tunnel test. The accuracy of the PIV velocities as compared to the pitot probe/manometer, across the scale, is 4.12 percent (19:1)

VSD Setting (Hz)	Nominal Velocity: Pitot (m/s)	Nominal Velocity: PIV (m/s)	Accuracy (%)
40	3.01	3.14	4.32
50	4.21	4.38	4.04
60	5.49	5.71	4.01

Table B-2: PIV Accuracy

The average accuracy, across the scale, is 4.14 percent (19:1).

APPENDIX C

INITIAL VELOCITY CHARACTERIZATION OF THE EQRTL AEROSOL DISPERSION WIND TUNNEL

The initial characterization of the EQRTL Aerosol Wind Tunnel was set up using the methods described in section 3.1.3. However, once the center chord line was analyzed at the 15 Hz VFD setting, it became apparent that significant physical modifications were needed before the $C_{v\%} \leq 10$ percent requisite could be achieved. The results of this original test are shown in Figure C1. For this original test, the circular cross section was defined as having a 20 inch diameter.

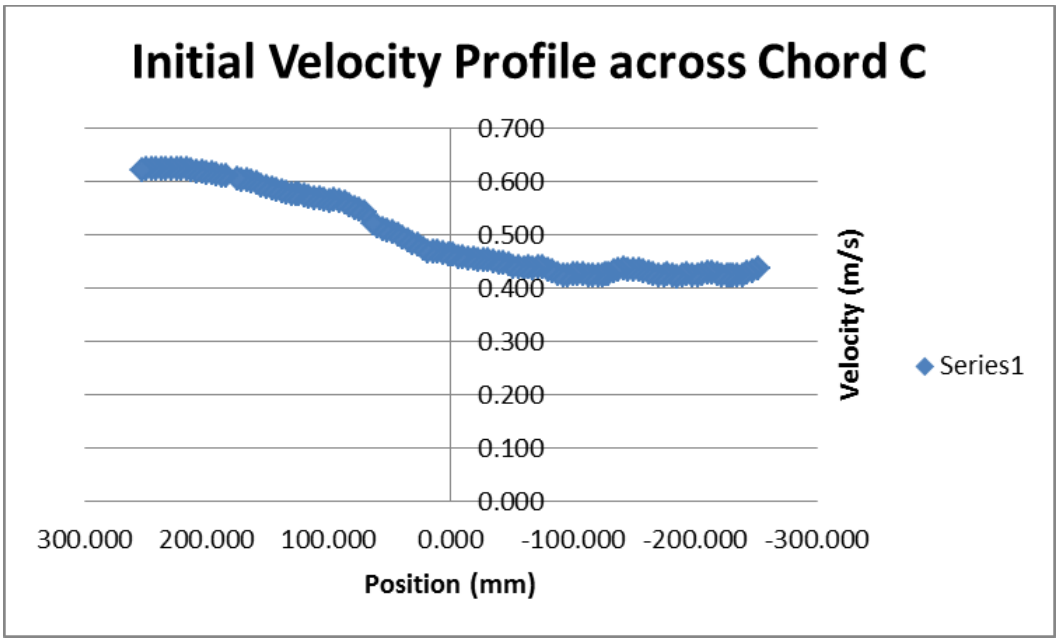

Figure C-1: Initial Velocity Profile across Chord C

The original velocity profile of Chord C is demonstrated by the scatter plot. Five chord subsections (C1-C5) were interrogated using the PIV and stitched together (see section 4.1 for explanation of stitching procedure). The velocities in the negative Z direction are substantially lower than those in the positive Z direction, indicating the presence of swirl induced by the turbulator.

As described in section 3.1.3, each chord subsection (C1-C5) was interrogated over two, two-minute collection runs, resulting in 60 image pairs per run (120 image pairs total). Each image pair was analyzed using the Insight 3G software, creating a single vector file for each image pair. Each vector file was then uploaded into the Tecplot program, where single time-averaged vector file was created for each subsection. Using this new vector file, 50 data points were extracted along the Z-axis at the image midpoint and put into an Excel file. The image-specific coordinates of each data point were converted to the coordinate system created to describe the entire cross section, and each data set was effectively "stitched" together for a continuous data set describing the entirety of chord C (note the Z-axis in Figure C1 appears reversed; however, this is how

the original cross section coordinate system was set up to reconcile images with traverse system movement of the CCD camera). The *u* component velocity values (in the X direction) of each data point were averaged to establish a mean velocity across the chord length, which was calculated as 1.79 km/hr (0.498 m/s). For the calculated velocities within the cross section to fall within 10 percent of the mean standard, there could be no values less than 1.61 km/hr (0.448 m/s), and no values greater than 1.97 km/hr (0.548 m/s). As can be seen in Figure C1, this was not the case, as the values varied as much as +25.4 percent from the mean.

APPENDIX D

PHYSICAL MODIFICATIONS TO THE EQRTL AEROSOL WIND TUNNEL

The initial configuration of the inlet consisted of a 1.03 m x 1.03 m x 1.42 m box holding four HEPA filters identical to those used at the tunnel exhaust to ensure only filtered air entered the tunnel. This filter box sat on the ground. At the top of the box a curved 90 degree elbow connected the filter box to the tunnel section. Immediately positioned downwind of this inlet was a circular Air Blender Turbulator mixing device, consisting of two concentric rings of wind vanes, each generating swirl counter-directional to the other. The original tunnel section was 6 diameters long (three, 0.102 m sections with 0.051 m diameters) and was connected directly to the testing chamber. The outlet of the circular tunnel section into the box testing chamber box was abrupt, with no expansion section. Multiple physical modifications to the wind tunnel were made to improve the homogeneity of the velocity profile. As discussed in the review of literature, there are numerous methods to accomplish this. First and foremost, it was recognized that the tunnel section itself must be lengthened, as a tunnel length should be roughly 10 times its diameter criteria for fully developed flow (Cenegal and Cimbala 2014). Consequently, two additional four foot sections were added, increasing the length from 6 diameters (3.66 meters) to 10 diameters (6.10 meters).

It was believed that the curved elbow leading up from the filter inlet box to the tunnel section might be introducing asymmetrical flow. After a new 0.61 m diameter

hole was cut in the front face of the filter box, a wooden platform was built to bring the filter box up from the floor and even with the tunnel section, eliminating the need for the curved inlet elbow entirely, providing a much more symmetrical airflow into the tunnel section.

Figure D-1: New EQRTL Aerosol Wind Tunnel Inlet Configuration

As can be seen by the initial velocity data shown in Appendix C, there was a strong velocity gradient from one side of the applicable test section to the other, indicating that the swirl induced by the Turbulator had not yet diminished at the testing point. To rectify this, a circular wooden plate with multiple, evenly-spaced 15.88 mm diameter holes (50 percent porosity) was placed 1 diameter downwind of the Turbulator. This design was based on the principles of flow straighteners as discussed by Pankhurst and Holder (1952), which are used to transfer the excess total head from the high velocity regions to the regions of lower velocity. This effectively breaks up the large-scale eddies

created by the blender, which require a long downstream fetch to diminish, into much smaller ones that diminish rapidly (see Chapter 2 for more details on flow modification devices).

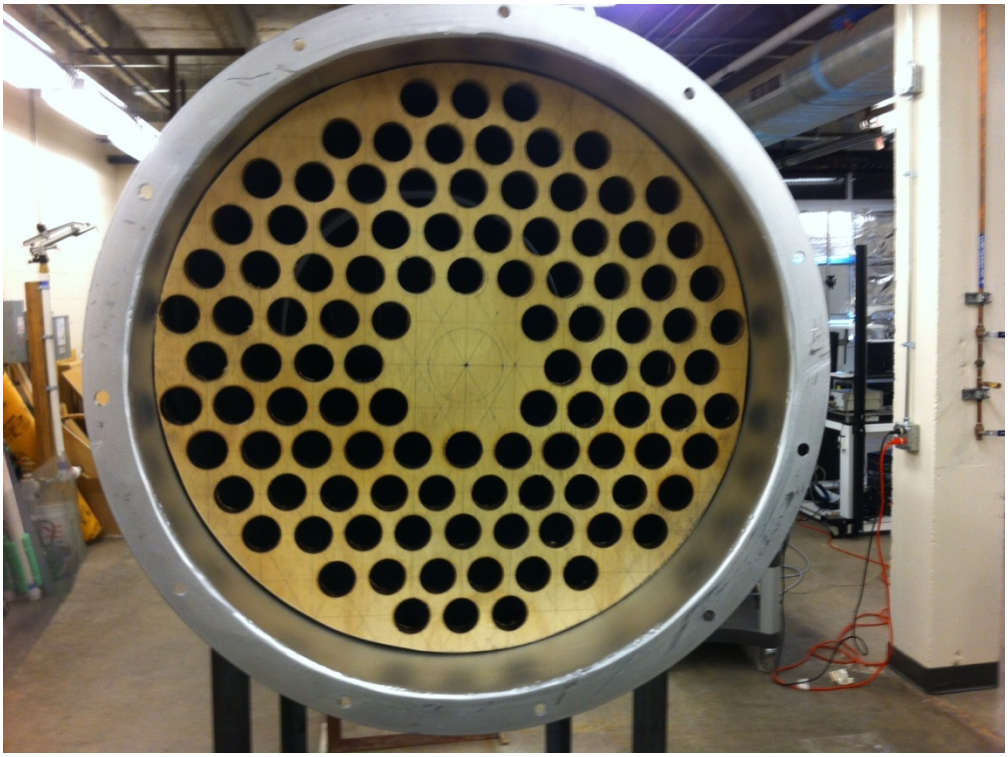

Figure D-2: Flow Straightener for EQRTL Aerosol Dispersion Wind Tunnel

The flow straightener is a 610 mm diameter wooden disk with 106 evenly-spaced 22 mm diameter holes, providing an approximate porosity of 50%. The plate breaks up the large eddies (swirl) induced by the turbulator by transferring the excess total head from the high velocity regions of the flow to the regions of lower velocity.

Lastly, the interface between the tunnel section and the test section was abrupt, likely causing large vortices in the corners of the box and distorting the velocity profile. Therefore, a shallow boxed flare expansion was constructed and placed at the outlet of the tunnel section, providing a more gradual exit into the test section.

APPENDIX E

VOAG VERIFICATION OF OPERATION

Before the VOAG could be used to characterize the concentration profile of the tunnel's cross section, the quality of the generated aerosol had to be verified as compliant with 60 CFR 53.42(a) (USEPA 1987), which states that the geometric standard deviation of the particle sizes produced could not exceed 1.1 and that the proportion of multiplets could not exceed 10 percent of the whole. The approved method for testing these requirements, as stated in 60 CFR 53.42(b) (USEPA 1987), is to capture sample aerosols via impaction onto a glass slide and to size the flattened spheroids using microscopy (see Chapter 2 for microscopy discussion). For each target test size, a minimum of three slides were exposed, resulting in no fewer than 15 interrogation images per size.

During the collection of droplets, the EQRTL's APS (see section 3.2.2) was used to size the aerosol population as well. In addition to continuously calculating the aerodynamic particle diameters in real time, the APS offers a convenient method of calculating the instantaneous geometric standard deviation of the aerodynamic diameters of the droplets within the generated population. Each APS data run was 20 seconds, at the end of which all data was averaged. The results of each data source (APS, microscope, and VOAG calculation) were compared. This verified that the VOAG was indeed generating highly-monodisperse aerosols, with an average geometric standard

deviation of 1.08 and a multiplet percentage of 6.99 over all testing sizes, with no individual test exceeding the maximums.

	µm	µm	µm	µm	µm	avg
Target	2	4	6	8	10	
Calculated	2	4.07	5.98	7.95	9.46	
Microscope	2.11	4.47	6.37	8.11	9.45	
APS	1.95	3.56	5.45	6.96	8.23	
Geometric stdv (APS)	1.07	1.06	1.08	1.09	1.09	1.08
% Multiplets	n/a	6.13	6.43	9.53	5.86	6.99

Table E-1: Results of VOAG, APS, and Microscope Comparison

The results are organized by target aerosol diameters (2, 4, 6, 8, and 10 µm). The values in the "calculated" row were derived from the methods described by Berglund and Liu (1973). Microscope analysis was performed on the flattened spheroids collected upon glass slides with the impactor to calculate the values in the "microscope" row. The values listed in the "APS" row represent the mean geometric aerodynamic diameter of the sample population as measured by the APS over 20 seconds, and the values listed in the "geometric stdv (APS)" show the geometric standard deviation of aerodynamic diameters of those same sample populations. The percent multiplet count lists the ratio of single droplets to droplets with 2 or more times the mass of a single droplet (multiplet). The percent multiplet count for the 2 µm tests is not applicable, as a reliable multiplet count could not be conducted. The average geometric standard deviation for all sizes was 1.08, and the average percent multiplet count across all sizes (except 2 µm) was 6.99 percent.

Table E-1 shows the results of these tests. The target values represent the aerodynamic diameters around which each test was designed. The calculated values are the results of applying the calculations described in Berglund and Liu (1973) and Faulkner and Haglund (2012) to the prepared oleic acid (with 5 percent uranine, by mass) and isopropyl alcohol solution. For each test, the ideal solution ratio at a set VOAG frequency (a frequency that, through observation of a "deflection test" as described in the TSI 2012 VOAG user's manual, proved to produce the most monodisperse population

when applied to a specific orifice plate) was calculated that would achieve the target aerosol diameter. The closest whole-number ratio to the ideal ratio was then used as a matter of practicality and ability given the EQRTL beakers and graduated cylinders (for example, if the ideal ratio for a 7 µm aerodynamic diameter at 70,000 Hz using a 20 µm orifice calculated to be 1:190.01, so 1:190 was used as a matter of practicality). Because of this, there are slight differences between the target and calculated values. These values were used as actual data points of comparison, while the target values were only used as guides when setting up the experiments.

The microscope values are the results of the calculated geometric mean of measured singlet spheroids on the treated glass slides after the flattening coefficient was applied. The precision of the microscope measurement using the click-and-drag measurement function of the software was +/- 1 pixel (much like the image calibration procedure for the PIV), as one can only click on a single whole pixel. Despite what is shown in Figure E-2 where pixel values are shown down to the hundredth decimal place, the user can only move between whole pixels. The decimal places are a result of the spatial calibration conversion between µm and pixel lengths. This measurement range is demonstrated in Figure E-2, as the pixel lengths across the singlet diameters range between 14.96 and 16.93 pixels. This resulted in large relative error of measurement values when analyzing smaller aerosols (as much as 38 percent for the 2µm tests). Therefore, to establish that the VOAG was indeed operating within acceptable ranges, three questions were asked:

1. Is the mass geometric standard deviation of a sample population below 1.1 as calculated by the APS?

2. Are there fewer than 10 percent multiplets present in a sample population?
3. Do the expected calculated values based on frequency and oleic acid / isopropyl alcohol ratio of the solution fall within the microscope measurement range after applying the +/- 1 pixel error?

In every instance, save one, the answer to these questions was “yes”, proving that the VOAG was indeed providing sufficiently monodisperse droplets for continued testing. The one instance where the answer was “unknown” occurred at the 2µm range when establishing the multiplet percentage. The 2 µm droplets did not have enough inertia to impact upon the center of the slide and were instead pulled out to the very edges of the impaction region (zones A and E) or missed the slides completely, while the multiplets impacted more toward the center of the slide (multiplets have at least twice the mass and inertia of a singlet, therefore multiplets will impact more readily upon the center of the slide). Because it could not be known with any confidence the ratio of singlets to multiplets in any single impaction zone, a ratio at this size was not given. However, the few singlets at the outer reaches of the impaction zone were sized to compare against the APS and calculated values. Regardless, given the results of the other tests and the high correlation between geometric standard deviation and multiplet percentage, it was assumed that the 2µm multiplet percentage was acceptable, especially given its low geometric standard deviation value as measured by the APS.

As the particle sizes increased, the deviation between the calculated and the APS values increased as well. This is due to the deformation of the liquid droplets as they are accelerated through the APS testing chamber (Baron, 1986). For the purposes of this research, the APS was not used as a precise sizing technique, but instead, given its proven

high reliability in calculating mass geometric standard deviations, was used as a qualitative check on the aerosol population during testing. In addition, using Microsoft Excel, a regression line and corresponding equation was calculated to describe the correlation between the APS values and the calculated values (Figure E-1), which resulted in a high coefficient of correlation (R^2 =0.9979). This made it possible to use the APS to serve as a "quick check" on aerosol sizes at intermittent times during testing, precluding the need for multiple microscope analysis for each test.

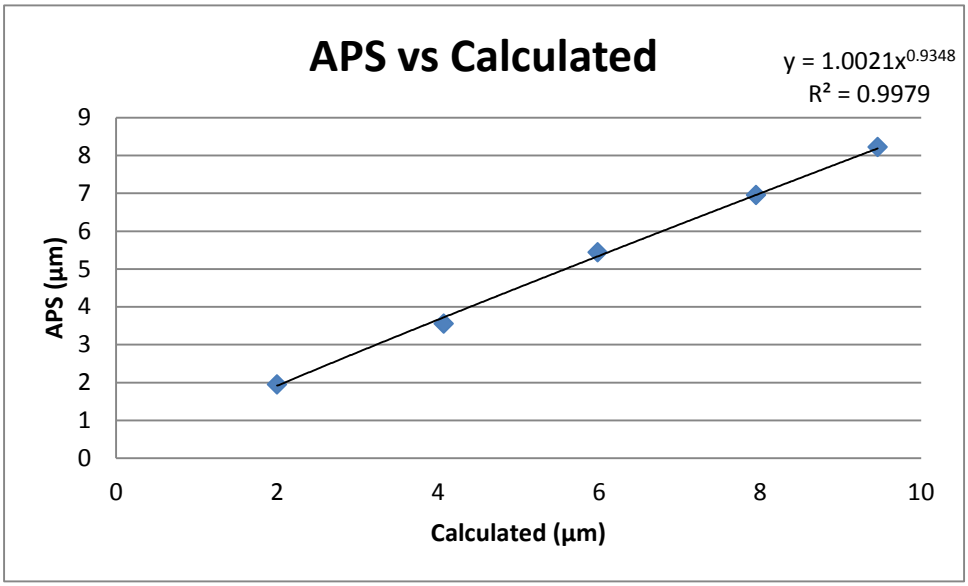

Figure E-1: APS Values versus Calculated Values

The geometric mean of the APS diameter measurements are plotted against the calculated aerodynamic diameters. The equation for the regression line is displayed in the upper right hand corner of the plot, along with the coefficient of determination (R^2) of 0.9979, which describes how well the regression line fits the data points. This equation was used as an intermittent "quick check" on aerosol sizes being produced by the VOAG throughout the concentration characterization phase of this research.

APPENDIX F

TROUBLESHOOTING

Nearly every user manual associated with each piece of instrumentation included troubleshooting procedures; however, this appendix lists the various troubleshooting procedures used to remedy issues unique to the experimental setup and application of this research.

F.1 TSI PIV System

General note: Never adjust objects in the laser light sheet without securing the CCD camera lens cap! This can easily result in severe damage to the CCD array!

1. ***Insight 3G Software will not initiate properly*:**

   Be sure the components to the PIV system were switched on in the proper order: CCD camera, synchronizer, laser power supply (on lowest power setting), then the software.

2. ***When viewing the objective with the CCD camera in "free" and "continuous" mode, there are areas in the image with pink pixels*:**

   When this occurs, immediately stop capturing, replace the lens cap, and adjust the f-stop on the camera lens to a lower setting. The pixels are becoming over-saturated in the areas where pink pixels are present. Continued over-saturation can result in damage to the camera's CCD array. Always start at the highest f-stop and adjust downward until the image becomes discernible to avoid damage to the camera.

3. ***When capturing an image pair in "synchronized" mode, one image is bright and the other is dark (or completely black):***

   a. Check the straddle settings (the point where the CCD array has completed assigning pixel values to make the first image and begins the second). If necessary, increase the PIV exposure time (μs) for the darker image by shifting the straddle point, which will allow for an increased exposure time for the darker image. A straddle point directly between two laser pulses means each image gets the exact same amount of exposure time; as mentioned in Appendix A, there is an illumination difference between laser pulses in most PIV systems (including the EQRTL system). Therefore, equal exposure time will result in an imbalance of image brightness, which could lead to poor data resolution when the software computes aerosol pattern displacement.

   b. It is also possible that one of the laser pulses (laser A or laser B) isn't properly illuminating the interrogation region. Turn on each laser pulse individually and fire it into the test section at the "low" power setting. Observe the alignment, position, and brightness of the laser sheet. Adjust the optics (mirrors, periscope assembly, etc) as necessary. Over the course of these experiments, it was found that the laser B pulse is perceptibly lower in illumination than laser A.

4. ***When capturing an image pair in "synchronized" mode, there are areas of pink pixels present:***

   Adjust the f-stop of the camera lens to a higher setting. Pixel over-saturation is occurring in those regions and can damage the CCD array. Always start at the highest f-stop and adjust downward until the image is properly illuminated without

excess over-saturation. Often one image will not have pink pixels while the second one does. Adjust the imaging straddle time so the illumination between the images is as equal as possible. Also consider reducing the aerosol seed density. Much like high beams of an automobile in the fog, an excess amount of light is scattered when the aerosol density is too high, resulting in pixel oversaturation.

5. ***When I fire the laser from the Insight software capture menu, nothing happens***: Be sure the laser is in the "on" position on BOTH the laser power unit AND on the Insight software control panel. Also make sure the control mode is set to "external" on the laser power unit. **WHEN MAKING THESE ADJUSTMENTS, BE SURE YOU ARE WEARING THE LASER GOGGLES AND THE LENS CAP IS ON THE CCD CAMERA!**

6. ***Even after adjusting the Δt to ensure the proper amount of pixel displacement has occurred between the images in an image pair, there are still a high number of "false" (red) vectors when the images are processed:***

   a. Most likely, this is because the camera isn't quite focused on the illumination region. If the images look "foggy" (for instance, if discrete groupings of illuminated pixels cannot be discerned from the pattern), then the camera needs to be refocused and the calibration procedure needs to be repeated.

   b. If the camera has been refocused and there is still a problem, re-check the pixel displacement between images to ensure the proper setting (between 5 and 15 pixels). If still problems persist, be sure the aerosol seed density is appropriate. If the density is too high, the statistical analysis (peak-locking) cannot perform properly and loses statistical confidence in the results.

7. ***When I view a velocity flow field (or an averaged velocity flow field) in Tecplot, the color scale covers an irrational range of values and the vectors are shown as tiny dots:***

   One of the calculated vectors within the flow field (or one of the original flow fields if looking at an averaged flow field) is erroneously high. Occasionally, depending on the post-processer settings, a "false" vector makes it through to the end flow field. The image pair can either be re-processed with adjusted post-processor settings to eliminate the erroneous vector, or if viewing an averaged flow field, the average can be re-calculated in Tecplot without the including the individual flow field at fault.

8. ***I was getting "good" vectors at one interrogation region, but after moving the camera with the traverse system to the next region all the vectors are now "bad:"***

   The vibration from the traverse movement can change the focus. Be sure to re-focus the camera on the objective each time the camera is moved and check that the calibration factor has not changed.

9. ***Velocity values are nowhere near what was expected:***

   More times than not, there is a problem with the calibration factor. Be sure the correct calibration is selected in the processing menu and check that a mistake was not made when inputting the numbers.

F.2 VOAG

1. ***Aerosol jet won't start:***

   a. Make sure the orifice plate is clean. Even though light can be seen coming through the hole when it is held up to a light source, this does not mean it isn't partially plugged. First follow the orifice back-flushing procedure outlined in the

VOAG manual (TSI, 2012c). If that doesn't work, follow the orifice cleaning procedures outlined in the VOAG manual (TSI, 2012c), using filtered detergent and distilled water. A plugged orifice can usually be spotted by monitoring the inline pressure gauge. If it climbs quicker than usual and the orifice only oozes solution (or nothing comes out at all), the orifice is probably plugged.

b. Make sure the solution being fed to the VOAG has been properly filtered. Triple-filtering through a glass fiber filter was found to be effective. Small, un-dissolved solids can plug the orifice plate.

c. Check the Micropore filter inside the filter holder for the solution feed line. The effectiveness of the filter will degrade over time (high differential pressure across the filter will cause an insufficient flow rate to the orifice), and will do so more quickly if the solution was not properly filtered. Changing the filter every 12 hours of run time was found to be effective.

2. VOAG droplets are not monodisperse:

a. Most of the time this is due to an improper feed rate / function generator frequency setting. TSI (2012c) recommends that a deflection test be conducted for each orifice, and the frequency be adjusted from there to find an acceptable frequency range over a given flow rate. While this is true, it was found in this research that the ideal flow rate / frequency window also seemed to be aerosol size-specific. For example, the smaller aerosols held desirably small geometric standard deviations when operated at a higher flow rate and higher frequency. When generating droplets above 10 µm, however, the operational window used for the small aerosols was no longer appropriate as a desirable geometric standard deviation could not be achieved. When

the flow rate was lowered and a new frequency range was established using another deflection test, the geometric standard deviation improved.

b. Inspect the orifice for damage. Over the course of this research four 20 µm orifices began to show signs of damage after extended use.

c. If gauging the geometric standard deviations of aerosol diameters using the APS, be sure to check the population against the microscope, particularly if the geometric standard deviations of larger-sized liquid particles are being analyzed. The deformation of larger particles as they go through the acceleration chamber can skew this data.

3. The aerosol population contains an unacceptably high number of multiplets:

a. First go through the procedures listed above to ensure the flow rate / frequency operational window is appropriate.

b. If the operational window is appropriate and the population is monodisperse save the presence of multiplets, then be sure the Kr-85 tube is clean. Follow the cleaning procedures outlined in the VOAG user's manual (TSI, 2012c).

c. If measuring multiplets under the microscope, be sure the proper amount of droplets are sampled using the impactor. If the sampling time is too long, then droplets will impact upon one another giving a falsely high number of multiplets. Multiplets caused by coagulation in the ionizer tube or distribution hose generally provide an oblate spheroid upon impact; however, multiplets resulting from overlying impaction may result in asymmetrical droplets.

APPENDIX G

APPLICABLE REQUIREMENTS FROM 40 CFR 53 SUBPARTS D AND F

40 CFR 53 Subparts D and F served as the main guidance for experimental design, setup, and execution for this research as well as provided the target performance goals for the designed aerosol dispersion wind tunnel. These requirements are summarized in this appendix. Note that the following tables are not meant as an exhaustive review of the CFR; they are only to help summarize the rules and requirements applicable to this research.

Particle size (µm)	Wind speed (km/hr)		
	2	8	24
3±0.5	L	L	L
5±0.5	L	L	L
7±0.5	L	L	L
9±0.5	L	L	L
10±0.5	L	L	L
11±0.5	L	L	L
13±1.0	L	L	L
15±1.0	L	L	L
20±1.0	L	L	L
25±1.0	L	L/S	L/S

Table G-1: Aerosol Testing Requirements for PM_{10} Candidate Federal Reference Method Samplers
(From Table D-2, 40 CFR 53 Subpart D, USEPA, 1987)

Table G-1 is organized by generated particle size ± the accepted tolerance, in µm. Each size is to be tested at 2, 8, and 24 km/hr. The L *indicates liquid aerosols, while the* S *indicates solid aerosols.*

Primary Partical Mean Size (µm)	Full Wind Tunnel Test (Aerosols < 2.5 µm)	
	2 km/hr	24 km/hr
1.5±0.25	S	S
2.0±0.25	S	S
2.2±0.25	S	S
2.5±0.25	S	S
2.8±0.25	S	S
3.0±0.25	L	L
3.5±0.25	S	S
4.0±0.5	S	S

Table G-2: Aerosol Testing Requirements for $PM_{2.5}$ Candidate Federal Reference Method Samplers
(From Table F-2, 40 CFR 53 Subpart F, USEPA, 1997)

Table G-2 is organized by generated particle size ± the acceptable tolerance, in µm. Each size is to be tested at 2 km/hr and 8 km/hr. The S *indicates solid aerosols, and the* L *indicates liquid aerosols.*

53.42 (Subpart D)--Generation of test atmospheres for wind tunnels	53.62 (Subpart F)--Test Procedure: Full wind tunnel test
53.42(a)	**53.62 (c)**
VOAG used to produce monodisperse particles	Wind tunnel test velocites are 2 km/hr and 24 km/hr
Solution of oleic acid and uranine dye	VOAG used to produce monodisperse particles
Geometric standard deviation of each particle size and type cannot exceed 1.1 for primary particles (singlets)	Geometric standard deviation of each particle size and type cannot exceed 1.1 for primary particles
Wind tunnel blower system must be capable of achieving uniform wind speeds at speeds specified in table D-2	Multiplets must make up no more than 10% of the aerosol population
53.42(b)	Aerosol sizes measured by method with a sizing resolution of 0.1 µm or less
Aerosols are verified using microscopy	Accracy of particle size verification technique must be 0.15 µm or better
Glass slides pretreated with oleophobic surfactant	Wind speed measurement method must have precision of 2% or better and an accuracy of 5% or better
Appropriate flattening coefficient must be applied to spheroids	Must have at least 12 velocity test points across cross section
Test aerosol sizes must be within tolerances specificed in Table D-2	Mean wind speed of tunnel must be within 10% of specificed in Table F-2
Precision of particle sizing technique must be 0.5 µm or better	Variation of wind speed at any test point cannot exceed 10%
Particle sizes determined by the verification technique cannot differ by more than 0.5 µm or 10%, whichever is higher, from the calculated size using VOAG operational parameters	Aerosol rake must have no less than 5 evenly spaced samplers
53.42(c)	Calibrated fluorometer must be used to quantify mass of exctracted aersol mass deposits
Multiplet population delivered to test section cannot exceed 10%	**53.62(d)**
53.42(d)	Wind speed during testing must be within 10% of speed specified in Table F-2
An array of not less than 5 evenly-spaced samplers must be used to determine concentration uniformity in the sampling zone	Aerodynamic diameter must be within tolerances specified in Table F-2
Particle concentration at a single point cannot differ by more than 10% from mean concentration	Verify qualityof test aerosols; the determined geometric mean aerodynamic diameter of test aerosol must be within 0.15 µm of calculated value from operating parameters of the VOAG
53.42 (e)	Multiplets in sample must not exceed 10% of total population
Wind speed verification method must be capable of a precision of 5% or better	An aerosol sampler rake with no fewer than 5 sampling cones must be used to determine the aerosol uniformity and concentration measurement
Mean wind speed must be within 10% of value specified in Table D-2	Deterine quanity of material with each sampler using fluorometer, C(iso)
Wind speed measured at any point within test area cannot differ by more than 10% of the mean wind speed	Calculate Cv(%) from C(iso)

Table G-3: Applicable Rules and Standards Organized by CFR; Subpart D (Left Column) and Subpart F (Right Column)

REFERENCES

Auvermann, Brent W. 2012. "Improving Estimates of Fugitive PM_{10} Emission Flux from Open-Lot Livestock Facilities via Vertical Profiling of Wind Vector and Mass Concentration," *Proposal: Texas AgriLife Research Air Quality Research Program FY2012-2013*.

Baron, Paul A. 1986. "Calibration and Use of the Aerodynamic Particle Sizer (APS 3300)," *Aerosol Science and Technology* 5(1): 55-67.

Brixey, L.A., Paik, S.Y., Evans, D.E., and Vincent, J.H. 2002. "New Experimental Methods for the Development and Evaluation of Aerosol Samplers," *Journal of Environmental Monitoring* 4: 633-641.

Berglund, Richard N. and Benjamin Y.H. Liu. 1973. "Generation of Monodisperse Aerosol Standards," *Environmental Science and Technology* 7 (2):147-153.

Cermak, Jack E. 1995. "Progress in Physical Modeling for Wind Engineering," *Journal of Wind Engineering and Industrial Aerodynamics* 54 (55): 439-455

Cermak, Jack E. 2003. "Wind-Tunnel Development and Trends in Applications to Civil Engineering," *Journal of Wind Engineering and Industrial Aerodynamics* 91: 355-370.

Cengal, Y.A. and J.M. Cimbala. 2014. *Fluid Mechanics: Fundamentals and Applications.* 3rd ed. New York: McGraw Hill.

Cheng, Y.S., H. Irshad, A.R. McFarland, W.C. Su, U. Zhou, and D. Barringer. 2004. "An Aerosol Wind Tunnel for Evaluation of Massive-Flow Air Samplers and Calibration of Snow White Sampler," *Aerosol Science and Technology* 38: 1099-1107.

Fantech. 2012. "Fantech FSD Series Square Inline Mixed Flow Centrifugal Fans," *Publication Item #450397*.

Faulkner, William B. and John S. Haglund. 2012. "Flattening Coefficients for Oleic Acid Droplets on Treated Glass Slides," *Aerosol Science and Technology* 46 issue 7: 828-832.

Hinds, W.C., and Kuo, T.L. 1995. "A Low Velocity Wind Tunnel to Evaluate Inhalability and Sampler Performance for Large dust Particles," *Applied Occupational and Environmental Hygiene* 10: 549-556.

Holton, James R. 1979. *An Introduction to Dynamic Meteorology.* 2nd ed. New York: Academic Press.

Klar, Scott. "User's Manual for UMD's Portable Dust Sensor." University of Minnesota-Duluth

Lee, Sangil, Miae Yu, and Hun H. Kim. 2013. "Development of Aerosol Wind Tunnel and its Application for Evaluating the Performance of Ambient PM_{10} Inlets," *Atmospheric Pollution Research* 4 issue 3: 323-328.

Legrand, Mathieu, Jose Nogueira, Alberth A. Vargas, Ruben Ventas, and Maria del Carmen Rodriguez-Hidalgo. 2014. "CCD Image Sensor Induced Error in PIV Applications," *Measurement Science and Technology* 25: 1-13.

Liu, B.Y., D.Y.H Pui, and X.Q. Wang. 1982. "Drop Size Measurement of Liquid Aerosols," *Atmospheric Environment* 16 issue 13: 563-567.

McFarland, A.R., Gupta, R., and Ananda, N.K. 1999. "Suitability of Air Sampling Locations Downstream of Bends and Static Mixing Elements," *Health Physics* 77: 703-712.

Normayati, Nordin, Safiah Othman, Vijay R. Raghavan, and Zainal Ambri Abdul Karim. 20112. "Verification of 3-D Stereoscopic PIV Operation and Procedures," *International Journal of Engineering & Technology* 12(4): 19-26.

Olan-Figueroa, E., A.R. McFarland, and C.A. Ortiz. 1982. "Flattening Coefficients for DOP and Oleic Acid Droplets Deposited on Treated Glass Slides," *American Industrial Hygiene Association Journal* 43: 395-399.

Ranade, M.B., M.C. Woods, F-L. Chen, L.J Purdue and K.A. Rehme. 1990. "Wind Tunnel Evaluation of PM_{10} Samplers," *Aerosol Science and Technology* 13(1): 54-71.

Pankurtst, R.C. and D.W. Holder. 1952. *Wind Tunnel Technique.* London: Sir Isaac Pitman & Sons. Out of print.

TSI Incorporated. 1994. "Particle Image Velocimetry," *TSI Seminar on Fluid Flow Instrumentation*. Shoreview, MN.

TSI Incorporated. 2005. *Powerview Plus 4MP Camera Model 630059* Revision A. Shoreview, MN.

TSI Incorporated. 2007. "Particle Image Velocimetry (PIV): Quantitative Flow Visualization," *Poster 5001111 Revision A.* Shoreview, MN.

TSI Incorporated. 2009. *Model 3321 Aerodynamic Particle Sizer Spectrometer* Revision F. Shoreview, MN.

TSI Incorporated. 2012a. "Aerodynamic Particle Sizer Model 3321: Theory of Operation," *P/N 5001468 Revision A.* Shoreview, MN.

TSI Incorporated. 2012b. "Aerosol Neutralizers Models 3012, 3012A, 3054, 3054A, 3077, 3077A, 348002," *P/N 2980230 Revision C.* Shoreview, MN.

TSI Incorporated. 2012c. *Model 3450 Vibrating Orifice Aerosol Generator* Revision L. Shoreview, MN.

Turner Designs. 1997. "Appendix A: Key Operating Principles of the Model 10-AU," *Model 10-AU-005-CE Fluorometer User's Manual* 998-001. Sunnyvale, CA.

U.S. USEPA. 1987. "Procedures for Testing Performance Characteristics of Methods for PM_{10}", *40 CFR 53 Subpart D, Federal Code of Regulations.* Washington, D.C.: U.S. Government Printing Office.

U.S. USEPA. 1997. "Procedures for Testing Performance Characteristics of Class II Equivalent Methods for $PM_{2.5}$", *40 CFR 53 Subpart F, Federal Code of Regulations.* Washington, D.C.: U.S. Government Printing Office.

Westerweel, J. 1997. "Fundamentals of Digital Particle Image Velocimetry," *Measurement Science and Technology* 8: 1379-1392.

Wilson, Brandon M. and Barton L. Smith. 2013. "Taylor-series and Monte-Carlo-method Uncertainty Estimation of the Width of a Probability Distribution Based on Varying Bias and Random Error," *Measurement Science and Technology* 24: 035301.

Wilson, Brandon M. and Barton L. Smith. 2013. "Uncertainty on PIV Mean and Fluctuating Velocity due to Bias and Random Errors," *Measurement Science and Technology* 24: 035302.

Wilson, David A.L., and Barry Martin. 2006. "The Distribution of the Geometric Mean," *The Mathematical Gazette* 90(517): 40-49.